POLITECNICO DI MILANO

School of Industrial and Information Engineering

Department of Aerospace Science and Technology

Master of Science in Space Engineering

Z-70 Hall Thruster Performance Analysis

EXPERIMENTAL THRUST AND PLASMA MEASUREMENTS

SUPERVISOR: PROF. LUIGI T. DE LUCA

CO-SUPERVISOR: PROF. MARK A. CAPPELLI

MSC CANDIDATE:

ANDREA MARCOVATI 815809

Academic Year 2014/2015

In memory of Prof. Adriano Morando and Prof. Teodoro Merlini

Praise to the Engineer

[The Engineer] is a great profession. There is the fascination of watching a figment of the imagination emerge through the aid of science to a plan on paper. Then it moves to realization in stone or metal or energy. Then it brings jobs and homes to men. Then it elevates the standards of living and adds to the comforts of life. That is the engineer's high privilege.

The great liability of the engineer compared to men of other professions is that his works are out in the open where all can see them. His acts, step by step, are in hard substance. He cannot bury his mistakes in the grave like the doctors. He cannot argue them into thin air or blame the judge like the lawyers. He cannot, like the architects, cover his failures with trees and vines. He cannot, like the politicians, screen his shortcomings by blaming his opponents and hope that the people will forget. The engineer simply cannot deny that he did it. If his works do not work, he is damned. [...]

On the other hand, unlike the doctor, his is not a life among the weak. Unlike the soldier, destruction is not his purpose. Unlike the lawyer, quarrels are not his daily bread. To the engineer falls the job of clothing the bare bones of science with life, comfort, and hope. No doubt as years go by people forget which engineer did it, even if they ever knew. Or some politician puts his name on it. Or they credit it to some promoter who used other people's money with which to finance it. But the engineer himself looks back at the unending stream of goodness which flows from his successes with satisfactions that few professions may know. And the verdict of his fellow professionals is all the accolade he wants.

Herbert Hoover, Engineer and President of the United States of America [1928-1932].

Abstract

Even though Hall thrusters have been studied for many years by the Russians and Western countries, part of the physics governing the plasma behavior is still not perfectly understood. This drove the work of Chris Young and Andrea Lucca Fabris who studied in detailed the Z-70 with a technique called Laser Induced Fluorescence (LIF) and numerical simulations. The Z-70 is a laboratory model of the SPT-70 which is a space qualified Russian Hall thruster with a diameter of around 72 mm. The LIF allows to measure the ion velocity in many precise points close to the exit section of the annular chamber. This thesis integrates their work by measuring the thrust under the same conditions and comparing the results obtained. The thrust was measured using an sophisticated instrument called thrust stand which was modified in order to get rid of the non-linear behavior of the instrument. A closed-loop control system was developed in order to keep the moving part fixed at a precise location preventing any non-linearity. A current-driven actuator made of a solenoid and a permanent magnet is able to generate the force for the control system. The thrust was then measured by looking at how much current is required to flow in the solenoid.

To integrate and enrich the comparison the ion velocity and the composition of the plasma were measured using a ExB sensor. The ExB sensor exploits a magnetic and electric perpendicular fields to deviate and collect ions at different energy levels. This instrument was partially developed by the author using the ExB sensor of the Electric Propulsion Laboratory (PEPL) of the Michigan State University as a reference.

Keywords

Electric Propulsion, Hall Thruster, Thrust Stand, Control System, Wien Filter

Sommario

Nonostante i propulsori a effetto Hall siano stati studiati intensamente per molti anni dai russi e dalle nazioni occidentali, alcuni aspetti della fisica che governa il comportamento del plasma all'interno di tali propulsori non sono ancora perfettamente chiari. Questo spinse Chris Young e Andrea Lucca Fabris a studiare in dettaglio il propulsore Z-70 utilizzando la tecnica della fluorescenza indotta da laser (LIF) e simulazioni numeriche. Il Z-70 è una copia di laboratorio del SPT-70 che è un propulsore russo qualificato per lo spazio dal diametro di circa 72 mm. La LIF permette di misurare precisamente la velocità degli ioni in prossimità della sezione di uscita della camera anulare del propulsore a effetto Hall. Questa tesi integra il loro lavoro misurando la spinta del propulsore sotto le medesime condizioni operative per vedere se si ottengono risultati paragonabili. La spinta è stata misurata utilizzando uno strumento molto sofisticato chiamato bilancia di spinta, il quale è stato modificato per prevenire gli effetti non lineari dello strumento. Un sistema di controllo in anello chiuso è stato sviluppato per far sì che la parte mobile della bilancia rimanga ferma, facendo così in modo che gli effetti di non linearità non si manifestino. Un attuatore comandato in corrente, costituito da un solenoide e un magnete permanente, è in grado di generare la forza di controllo per l'anello chiuso. La spinta è stata misurata misurando quanta corrente è necessaria per compensare la spinta. Per integrare e arricchire il paragone la velocità degli ioni e la composizione del plasma sono stati misurati utilizzando un sensore E cross B. Questo tipo di sensore sfrutta un campo magnetico e uno elettrico perpendicolari tra loro per deviare e percepire gli ioni a diversi livelli energetici. Lo strumento è stato parzialmente sviluppato dall'autore come copia del sensore ExB del Electric Propulsion Laboratory (PEPL) della Michigan State University.

Parole Chiave

Propulsione Elettrica, Propulsore ad Effetto Hall , Bilancia di Spinta, Sistema di Controllo, Selettore di Velocità Ionica

Acknowledgments

The acknowledgments section is divided in two parts, the Stanford part (in English) and the Milan part (in Italian).

For the Stanford part I would like to thank all the people who helped me during these incredible six months, in particular all the guys from the SPPL team. Thank you Bob and David for all the lunches together, I know we have different views about the world, nevertheless it has been a pleasure to bump heads with you guys. Thank you Taemin for being so kind to me all the time. Thank you Andrea, you have been so helpful for the first part of the thesis and for all the nice and useful inputs. Thank you Fabio, you have been the closest friend during the six months, I always knew I could count on you. Nic and Chris, you guys helped me so much and I learned so much from you. Nic, every time you talked to me I felt like I had to take out my notebook and write down everything you said. I will hardly forget the afternoons spent together trying to find the right Swagelok fitting! Chris, without you I would have been lost, thank you for running the thruster all those times just for me. Do you remember when we hammered the cooling shroud? I think we should have hit it harder.... much harder! Thank you Ricky for the help with the E cross B sensor. Mark, thank you for inviting me to Stanford, it was the best experience ever. Thank you for having had faith in me, even if you didn't know me.

Per la parte milanese un grazie speciale a tutta la mia famiglia. Grazie mamma e papà per avermi supportato, non solo economicamente. Mi avete sempre dato una seconda chance (e una terza e una quarta) anche quando non me la meritavo. Grazie Luca per sopportarmi sempre. Giulia, tu sei la costante della mia vita. Grazie per essermi venuta a trovare a Natale, ci siamo divertiti un sacco a Las Vegas. Avevi ragione tu: il fatto che il nero sia uscito sei volte di fila non significhi che sia buona idea puntare tutto sul rosso. Grazie a tutti quelli che hanno creduto in me. Un grazie speciale al professor De Luca per aver avuto fiducia in me e per avermi insegnato praticamente tutto ciò che so sulla propulsione.

Estratto della Tesi

Capitolo 1

Introduzione

Il plasma è un costituente fondamentale dell'universo. Il 99% della materia dell'universo è in stato plasmatico. Il plasma è un fluido in cui cariche positive e cariche negative sono libere di muoversi e interagire con campi esternamente applicati o autogenerati, secondo le ben note equazioni di Maxwell. Le due condizioni essenziali per capire cosa succede ad una carica all'interno di un propulsore ad effetto Hall sono due: carica immersa in solo campo magnetico e carica immersa in campo magnetico ed elettrico perpendicolari. Quando una carica è immersa nel solo campo magnetico ruota attorno alle linee di campo magnetico in orbite circolari, il cui raggio viene chiamato raggio di Larmor, La carica, mentre ruota, si muove di moto a velocità costante in direzione parallela alle linee di campo magnetico. Una ulteriore campo elettrico tende ad attrarre gli ioni verso potenziali più bassi (nel caso di ioni positivi) e deformare così le orbite. Per un effetto chiamato ExB drift, dovuto all'agire di un campi elettrici e magnetici perpendicolari, le cariche si muovono di un moto netto in direzione perpendicolare ai campi sia megnetico che elettrico. Questo effetto porta, all'interno di un propulsore a effetto Hall, alla generazione di una corrente chiamata corrente di Hall, la quale è fondamentale per la generazione della spinta e da' il nome al propulsore. Un propulsore a effetto Hall è costituito da 4 elementi principali: un anodo, un catodo, dei circuiti magnetici e una camera anulare. Il catodo (caricato negativamente), esterno alla camera anulare, emette elettroni, i quali vengono naturalmente attratti verso l'anodo (caricato positivamente). Il catodo, alimentato a gas argon per lo Z-70, è di tipo cavo. L'anodo è posizionato in fondo alla camera anulare e da lì atomi di xeno vengono emessi. I circuiti magnetici generano un campo magnetico radiale all'interno della camera anulare. Quando gli elettroni emessi dal catodo entrano nella camera anulare si

trovano immersi in un campo magnetico e quindi iniziano a spiralare attorno alle linee di campo e si dicono magnetizzati. Mentre girano vengono anche attratti dal campo elettrico e iniziano a ruotare in direzione tangenziale. Gli elettroni risultano effettivamente intrappolati dal campo magnetico, il loro moto verso l'anodo è ostacolato e formano una nuvola elettornica proprio in prossimità dell'uscita della camera anulare. Gli atomi di xeno interagiscono con questi elettroni e si caricano positivamente quando vengono colpiti con abbastanza energia. Gli ioni positivi di xeno vengono così attratti dalla nuvola ed espulsi ad altissima velocità. Gli ioni, in quanto molto più pesanti degli elettroni, non vengono magnetizzati e possono così accelerare senza venire intrappolati dal campo magnetico. Alcuni elettroni riescono a raggiungere l'anodo e chiudono il circuito elettrico, alcuni formano la nuvola elettronica e altri ancora si mischiano con gli ioni in uscita per formare un getto neutro. I propulsori ad effetto Hall costituiscono uno dei più efficienti sistemi di propulsione ad uso spaziale, molto più efficienti dei motori termochimici, competono con i propulsori ionici, i quali, sebbene possano essere più efficienti, hanno un minore rapporto spinta-potenza.

Capitolo 2

Bilancia di Spinta

Uno strumento particolare, chiamato bilancia di spinta, è necessario per una misura accurata della relativamente bassa spinta di un propulsore a effetto Hall (grammi di spinta). La bilancia di spinta è formata da una parte mobile e una parte fissa. La parte mobile oscilla attorno ad una posizione di equilibrio grazie ad una molla e uno smorzatore magnetico. Sulla parte mobile viene montato il propulsore a effetto Hall. Quando il propulsore è acceso spinge la parte mobile, la quale trova una nuova posizione di equilibrio. Lo spostamento viene registrato da un LVDT. Grazie ad una calibrazione, che viene effettuata rilasciando dei pesi di massa nota sulla parte mobile, è possibile relazionare lo spostamento registrato dal LVDT alla spinta. Il

problema di questo stumento è che il coefficiente di rigidezza non è costante e tende a variare con lo spostamento a causa del fatto che il sistema non è per nulla lineare. L'autore della tesi propone ed effettua una modifica a questo strumento. Al posto di lasciare che la parte mobile trovi una nuova posizione di equilibrio, un attuatore fa in modo che la parte mobile torni alla posizione di equlibrio iniziale esercitando una forza che, una volta che la posizione di equilibrio iniziale è raggiunta, è uguale alla spinta del propulsore a effetto Hall. L'attuatore è formato da un magnete permanente, attaccato alla parte mobile, e un solenoide, attaccato alla parte fissa. Quando della corrente circola all'interno del solenoide genera un campo magnetico che interagisce con quello generato dal magnete permanente. L'interazione dei due campi magnetici risulta in una forza di attrazione o repulsione. Questa forza è la forza di controllo. Al posto dello spostamento, la nuova bilancia di spinta relaziona la spinta con la corrente che circola all'interno del solenoide. Il sistema di controllo è un sistema in anello chiuso dove la corrente viene fornita da un alimentatore che a sua volta viene comandato da un computer. Il computer riceve lo spostamento dal LVDT e un regolatore digitale PI, implementato in LabView, decide la corrente che l'alimentatore deve fornire al solenoide. La corrente viene misurata grazie ad una resistenza di shunt da 1 Ohm posta in parallelo alla linea che alimenta il solenoide, in modo che la caduta di potenziale sia uguale alla corrente che passa nella linea. Questa caduta di tensione viene registrata e salvata sul computer. Il magnete scelto è un magnete cilindrico al neodimio in quanto è il più forte dei magneti e anche il più diffficile da smagnetizzare. Il solenoide è formato da 20 avvolgimenti ed ha più o meno le stesse dimensioni del magnete permanente. La distanza tra loro è di circa un quinto di pollice.

Capitolo 3

Misure Sperimentali

I test sono stati effettuati nel laboratorio di fisica dei plasmi dell'università di Stanford. Il sistema è posto all'interno di una grossa camera a vuoto dal diametro di 1,5 metri e profonda più di 4 metri. La camera è collegata ad un sistema di pompe da vuoto che le permettono di simulare l'ambiente spaziale. Delle pompe chiamate "roughing pumps" costituiscono il primo stadio di vuoto e portano la pressione in camera a circa 30mTorr. Una turbopompa abbassa la pressione fino a pochi Torricelli, successivamente la camera viene isolata dalle pompe. Dei pannelli all'interno della camera vengono portati a temperature criogeniche da un unità PolyCold e due criopompe. Le molecole rimaste all'interno della camera congelano quando vengono a contatto con i pannelli e non danno più un contributo di pressione. Le criopompe rimangono accese durante i test per fare in modo che le molecole introdotte dal propulsore vengano congelate il più in fretta possibile, in modo tale che la pressione rimanga bassa durante l'esperimento. Con questa tecnica la pressione scende drasticamente (nell'ordine di $10^{-5} Pa$) simulando il vuoto dello spazio profondo. La bilancia di spinta, con il propulsore montato sopra, è posta all'interno della camera e collegamenti di gas ed elettrici collegano la bilancia di spinta con l'esterno. La corrente di controllo, durante i test, manifesta un sostanziale incremento anche in assenza di forza applicata (current drift). Ciò è dovuto all'aumento di temperatura del sistema. Infatti quando il propulsore si accende diventa molto caldo e ciò porta ad un allungamento della bilancia di spinta a causa della dilatazione termica. Il magnete e il solenoide si allontanano tra loro e quindi il sistema ha bisogno di usare più corrente per bilanciare il sistema e questo è il motivo dell'aumento di corrente. Per risolvere questo problema l'autore ha perfezionato un sistema di acquisizione di misura che permette di calcolare la spinta in modo preciso, tenendo conto dell'aumento di temperatura. Il propulsore viene acceso e tenuto acceso per almeno mezzora in modo che possa entrare pienamente a regime, poi il sistema di controllo viene acceso e inizia l'acquisizione. I pesetti di

calibraizone vengono rilasciati uno alla volta e poi sollevati uno alla volta in modo da relazionare la forza con la corrente, poi il propulsore viene spento e la corrente di controllo diminuisce bruscamente, in quanto non deve più bilanciare la spinta. Confrontando la calibrazione con il salto di corrente dovuto allo spegnimento del propulsore, la spinta viene calcolata. Il cambiamento di corrente dovuto alla temperatura viene sottratto facendo del post-processing al computer, ma è in ogni modo contenuto dato che l'acquisizione avviene in pochi minuti. La spinta calcolata nel punto di interesse è di circa 27 mN, impulso specifico di circa 1300s e efficienza dell'anodo di circa 40%. Questi valori sono in accordo con i valori stimati dalle simulazioni numeriche e misurati con le misurazioni laser (LIF).

Capitolo 4

Misurazioni di Velocità Ionica

Un sensore ExB non funzionante viene modificato e aggiustato. Il sensore consiste in una scatola metallica con dei magneti permanenti per generare un campo magnetico constante e un grosso condensatore, comandato da un alimentatore, per generare un campo elettrico costante. Il campo elettrico viene fatto variare e la forza che aglisce sugli ioni, che è dovuta ai due campi, varia a seconda del voltaggio dell'alimentatore. Un apertura consente ai soli ioni orizzontali di entrare la scatola. Gli ioni che entrano vengono deviati dai campi elettrico e magnetico. Quando la forza risultante è nulla gli ioni colpiscono un sensore e producono un segnale in corrente. La principale modifica consistette nella rimossione dei tubi di alluminio che schermavano gli ioni dal campo elettrico, ma non da quello magnetico, impedendo quindi al sensore di funzionare correttamente. Il segnale generato dal sensore ExB presenta due chiari picchi, uno relativo agli ioni singlorarmente ionizzati e uno, più piccolo, realtivo agli ioni doppiamente ionizzati. Dalla distribuzione di corrente la concentrazione delle due specie ioniche viene calcolata e risulta essere di circa 94.5% ioni singolarmente ionizzati e circa 5.5% di ioni

doppiamenti ionizzati. Il sensore permette anche la stima dell'energia delle singole specie ioniche. Dall'energia è possibile calcolare il potenziale di accelerazione che è un informazione importante perchè rende possibile stimare dove, all'interno del propulsore, le singole specie ioniche si formano. Gli ioni singolarmente ionizzati si formano vicino alla fine della camera anulare, cioè dove il campo magnetico è più forte, mentre gli ioni doppiamente ionizzati si formano piùa valle, dove il potenziale è minore.

Capitolo 5

Conclusioni

Le modifiche apportate alla bilancia di spinta sono state un successo. La bilancia di spinta non è più affetta da non linearità dovute allo spostamento grazie al fatto che ritorna sempre nella stessa posizione di equilibrio. La velocità degli ioni in uscita calcolata dalla bilancia di spinta, simulazioni numeriche, indagine laser (LIF) e ExB viene confrontata. Mentre bilancia di spinta, simulazioni numeriche e LIF portano a risultati molto simili, il sensore ExB porta a rislutati sovrastimati e ciò è probabilmente dovuto al fatto che la scatola metallica interagisce con il plasma e, a causa del fatto che è messa a terra, il suo potenziale è molto basso e quindi tende ad accelerare ulteriormente gli ioni. Ad ogni modo la scatola è molto utile per misurare le concentrazioni delle specie ioniche. Per futuri usi, la bilancia di spinta può essere utilizzata con un sistema di raffreddamento per diminuire l'aumento di corrente in assenza di spinta e il sensore ExB può essere usato in un modo innovativo per poter calcolare le concentrazioni delle specie in funzione del tempo.

Contents

List of Figures

List of Tables

Nomenclature

α	Plasma composition correction factor
α_T	Coefficient of thermal expansion
ΔV	Difference in potential between the ExB plates
Δv	Velocity increment
$\dot{m}_a$	Anode mass flow rate
$\dot{m}_c$	Cathode mass flow rate
$\dot{m}_p$	Mass flow rate of propellant
ε_0	Dielectric constant in vacuum
η_0	Electrical utilization efficiency
η_a	Anode efficiency
η_c	Cathode efficiency
η_m	Mass utilization efficiency
η_q	Charge utilization efficiency
η_t	Total efficiency
γ	Correction factor
$\mathbf{J_{Hall}}$	Hall current
μ_0	Magnetic permeability
ω_c	Cyclotron frequency
Ω_i	Current fraction of the species i

ρ	Density
ρ_c	Density of the chain
σ	Variance the Gaussian
θ_c	Angle of rotation spool
ΔL	Elongation
ξ_i	species fraction for species i
A	Amplitude of the Gaussian peak
A	Area
B	Magnetic field
d	Damping coefficient
d	Distance between the ExB plates
D_e	Outer diameter
D_i	Inner diameter
E	Electric field
E	Energy
e	Charge of electron
e	Error
F	Force
f	Control force
F_B	Magnetic force

f_b Frequency of breathing oscillation

F_{cal} Calibration force

F_{dd} Dipole-dipole force

F_E Electric force

F_{FEMM} FEMM force

F_{tot} Total force

F_t Divergence angle correction factor

G Transfer function

i Current

I^{++} Doubly-charged ions current

I^{+} Singly-charged ions current

i_{cal} Calibration current

I_d Discharge current

I_{sp} Specific impulse

k Stiffness coefficient

k_d Derivative constant

k_i Integral constant

k_p Proportional constant

L Channel length

L_c Length of the chain

m	Mass
m_1	Magnetic moment of solenoid
m_2	Magnetic moment of magnet
m_0	Initial mass
m_c	Mass of the chain
m_f	Final mass
m_I	Mass of ions
M_m	Molecular mass
m_p	Propellant mass
m_{tot}	Total mass released
m_w	Mass of the weights
N	Number of turns
n	number density
n_e	Number of electrons
n_i	Density species i
n_i	Number of ions
p	Chamber pressure
p_c	Minimum chamber pressure
P_d	Discharge power
P_{jet}	Jet power

P_k Cathode keeper power

P_{mag} Magnetic circuits power

P_{tot} Total power

q Charge

r Distance between solenoid and magnet

r_0 Distance between solenoid and magnet at rest

r_L Larmor radius

R_s Radius of the spool

sccm Standard cubic centimeter per minute

T Thrust

T_{left} Temperature of left panels

T_{right} Temperature of right panels

u_e Velocity of expulsion

u_i Velocity species i

v LVDT output

v Voltage relative to the Gaussian peak

V^+ Positive plate potential

V^- Negative plate potential

V^G Ground potential

v_0 Setpoint voltage

V_{acc}	Acceleration potential
V_b	Beam potential
V_c	Coupling voltage
V_d	Discharge potential
V_g	Ground potential
x	Position of thrust stand
Xe^0	Neutral xenon atom
Xe^1	Positive xenon atom
Z_i	Charge state

1 Introduction

1.1 Motivations

Since the beginning of space exploration, chemical rockets had been the main choice of propulsion technology for spacecrafts, while electric propulsion for in-space applications was considered not much more than an elegant alternative.

Even though electric propulsion technology was proven to be much more efficient [9], government-owned agencies preferred to stick to the well-known and well-tested chemical rockets in the attempt to reduce the risk of failure.

In particular Hall thrusters, which have been intensively tested by both Russians and Americans, promise high efficiency and high thrust-to-power ratio [7], but at the cost of big powers which are not needed for chemical rockets.

In the last decade space companies all around the world, both private and public, are building satellites which rely on bigger and bigger power production and conditioning systems. The power produced and processed by these big satellites is now used for powering electric thrusters, mostly Ion and Hall thrusters, for any kind of purpose like station keeping, maneuvering and deorbiting.

The space company SpaceX has now opened a new satellite development facility in Washington State, with the goal of developing electrically powered satellites for a new and innovative space-based internet communication system and is now hiring electrical propulsion experts for the development and testing of Hall thrusters. SpaceX has also recently launched the world's first two all-electric satellites: the Asian ABS-3A and the American Eutelsat 115 West B, which are both communication satellites in geostationary orbit.

What was once considered a thing of the future represents now a reality for space engineering and the academic community has now a renewed interest in doing research on this kind of engine.

1.2 Basic Plasma Physics

This introduction provides the basic plasma physics necessary to understand what happens inside an Hall thruster and so better understand the purpose of the thesis.

Plasma is one of the fundamental states of the matter. Even though it is not common in daily life, plasma amounts for 99% of the known matter in the universe, meaning that 99% of the known matter (which is just 5% of the total) is in plasma state. The reason for that is because plasma is the main constituent of the stars and interstellar clouds.

Plasma is a collection of charged particles that are free to move when immersed in an electric field E or magnetic field B applied or self-generated according to the Maxwell equations:

$$\nabla \cdot E = \frac{\rho}{\varepsilon_0} \tag{1.1}$$

$$\nabla \times E = -\frac{\partial B}{\partial t} \tag{1.2}$$

$$\nabla \cdot B = 0 \tag{1.3}$$

$$\nabla \times B = \mu_0 \left(J + \varepsilon_0 \frac{\partial E}{\partial t} \right) \tag{1.4}$$

whereis the charge density of plasma, ε_0 is the dielectric constant in vacuum and μ_0 is the magnetic permeability.

In a neutral plasma the number of positively charged particles (xenon ions in the Z-70 Hall thruster) is almost equal to the number of negatively charged particles (mostly electrons) $n_i \approx n_e$ [7].

In order to understand what happens inside an Hall thruster one must understand the behavior of a particle inside a magnetic and an electric field.

For a charged particle the Lorentz equation holds:

$$F = m\frac{dv}{dt} = q\left(E + v \times B\right) \tag{1.5}$$

For a charge particle, for which the electric field is negligible and the magnetic field is only along the $\hat{z}$ direction , equation 1.5 in each direction becomes:

$$\begin{aligned} m\tfrac{\partial v_x}{\partial t} &= qBv_y \\ m\tfrac{\partial v_y}{\partial t} &= -qBv_x \\ m\tfrac{\partial v_z}{\partial t} &= 0 \end{aligned} \tag{1.6}$$

The third equation states that the velocity of the particle in the direction of the magnetic field remains constant.

Taking the time derivatives of the other two equations and dividing by the mass of the charged particles leads to:

$$\begin{aligned} \tfrac{\partial^2 v_x}{\partial t^2} &= \tfrac{qB}{m}\tfrac{\partial v_y}{\partial t} = -\left(\tfrac{qB}{m}\right)^2 v_x \\ \tfrac{\partial^2 v_y}{\partial t^2} &= -\tfrac{qB}{m}\tfrac{\partial v_x}{\partial t} = -\left(\tfrac{qB}{m}\right)^2 v_y \end{aligned} \tag{1.7}$$

The solution, in the x-y plane, is the simple harmonic oscillator.

$$v_{x,y} = v_\perp e^{i\omega_c t} \tag{1.8}$$

Where $v_\perp$ is the velocity component perpendicular to the magnetic field and ω_c is the cyclotron frequency defined as:

$$\omega_c = \frac{|q|B}{m} \tag{1.9}$$

A charged particles, inside a magnetic field and negligible electric field, starts to rotate around the magnetic field direction.

Plugging the definition of cyclotron frequency 1.9 in equation 1.7 leads to:

$$\begin{aligned} v_x &= -\tfrac{1}{\omega_c}\tfrac{\partial v_y}{\partial t} \\ v_y &= \tfrac{1}{\omega_c}\tfrac{\partial v_x}{\partial t} \end{aligned} \tag{1.10}$$

The trajectory of the charged particles in the y direction can be found by plugging equation 1.10 into equation 1.8 and then integrating:

$$y - y_0 = \frac{v_\perp}{\omega_c} cos(\omega_c t) = r_L cos(\omega_c t) \tag{1.11}$$

Where r_L is the Larmor radius (or gyroradius) defined as the ratio between the velocity perpendicular to the magnetic field and the cyclotron frequency.

Another way of seeing this effect is to think of the effect of the centrifugal force which is generated while the particle, subjected to the Lorentz force, rotates around the magnetic field direction as shown in figure 1.1 .

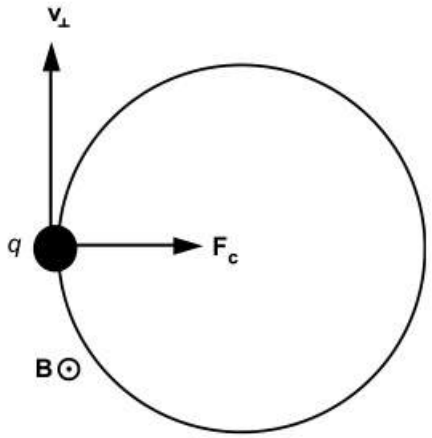

Figure 1.1: Centrifugal force [7]

The particle is subjected to the well known Lorentz force:

$$\mathbf{F} = q(\mathbf{v} \times \mathbf{B}) \tag{1.12}$$

The force generates in the direction perpendicular to both the velocity of the particle and the magnetic field causing the particle to move in circle (or gyrate).

The Lorentz force equals the centrifugal force:

$$\frac{mv_{\perp}^2}{r_g} = |q|\, v_{\perp} B \tag{1.13}$$

Which leads to the definition of Larmor radius:

$$r_g = \frac{mv_{\perp}}{|q|B} \tag{1.14}$$

The particles, while rotating, form a current loop which generates an induced magnetic field which is always opposite the one that originated the gyration in the first place, this effect is called diamagnetism [7].

The next condition of interest is when there is also an electric field perpendicular to the magnetic field. Equation 1.5, in steady state conditions, becomes:

$$\mathbf{E} = -\mathbf{v} \times \mathbf{B} \tag{1.15}$$

Taking the cross product of both sides of the equation leads to:

$$\mathbf{E} \times \mathbf{B} = (-\mathbf{v} \times \mathbf{B}) \times \mathbf{B} = \mathbf{v}B^2 - B\,(\mathbf{B} \cdot \mathbf{v}) \tag{1.16}$$

In the planar case in figure 1.1 the dot product between the magnetic field and the velocity of the particle is equal to zero. So the velocity of the particle is:

$$\mathbf{v} = \frac{\mathbf{E} \times \mathbf{B}}{B^2} \tag{1.17}$$

This is called “E cross B” drift velocity [7]. The drift is in the direction perpendicular to both E and B.

An electron immersed in an electric and magnetic field moves towards the higher potential and tends to gyrate around the direction of the magnetic field, and while it does that it also drifts in the ExB direction. This generates elongated orbits and causes a net motion of particles in the ExB direction [7].

The temperature cannot be considered to be the same for both electrons and ions. In particular the electron temperature is higher than the ion temperature [7]. In fact

electrons are more mobile, due to their lower mass, and they tend to make a larger number of coulomb collisions because, on average, they spend more time inside the thruster [7]. Moreover, as it will be explained later, electrons are injected from the cathode after being heated up. The ions, on the other hand, tend to be colder because they are extracted from the plasma to form the thrust beam, so they leave the plasma after perhaps only one pass [7].

1.3 Hall Thrusters

1.3.1 History and Use

Hall thrusters were first studied in the Soviet Union and in the USA. While American scientists preferred to concentrate on the development of gridded ion thrusters, the Russians developed the first space-qualified thruster in 1971 [7] and they have been studying and improving this technology ever since. Recently the implementation and use of Hall thrusters have been the interests of western countries, for example the European Space Agency (ESA) used Hall thrusters to propel the SMART-1 probe.

Hall thrusters rely on very complex physics, more complex than ion thrusters, but they are relatively simple devices [7]. They are made of an annular channel, an anode, an external cathode and a magnetic circuit which generates a radial magnetic field inside the annular channel.

The performance of this kind of engine is much higher than chemical rockets in terms of mass consumption [9, 18], but gridded ion thrusters can achieve an even higher mass efficiency, as shown in table 1.1 summarizing the performances of thruster technologies [7, 18, **?**, **?**, **?**, 9].

Engine	Thrust [mN]	I_{sp} [s]	η_t %	Common propellant	Power [kW]
chem solid	up to 10^{10}	210-320	~50	$NH_4ClO_4 + Al$	-
chem liquid	up to 10^{10}	290-450	~50	$N_2H_4, H_2 + O_2.$	-
chem mono	30-100,000	200-250	~50	N_2H_4	-
resistojet	100-500	200-350	65-90	H_2, CH_4, NH_3, N_2H_4	0.5-1.5
arcjet	200-2,000	400-2000	30-50	H_2, N_2, NH_3, N_2H_4	0.3-100
Ion	0.01-200	2500-3600	60-80	$Xe, ArKr$	0.5-2.5
Hall	0.01-200	1500-2000	35-60	Xe, Ar	1.5-5
MPD	0.01-200	2000-5000	25-50	Xe, ArH_2Li	1-4000
PPT	0.01-20,000	600-2000	5-10	$Teflon$	0.001-0.2

Table 1.1: Comparison of different thrusters

The specific impulse I_{sp} is the most important parameter in space propulsion. The total efficiency η_t takes into account the amount of theoretically available energy effectively converted into kinetic energy. For electric thrusters the available energy is the total electrical energy [7], while for chemical thruster is the chemical energy stored in chemical bonds in the propellant [18]. Both I_{sp} and η_t will be discussed later on in the thesis.

Even though they are less efficient than ion thrusters, Hall thrusters have an higher thrust over power ratio and they have comparable total impulse values even if the operational time of Hall thrusters is shorter, due to the inevitable consumption of the annular ceramic channel [7].

Russian, American and European space companies are now also engaged in the development of high power Hall effect thrusters (with power up to 50 kW), which will increase the specific impulse up to 7000 s (TM-50 by TsNIIMaSh).

Concerning electric propulsion, sometimes the word expellant is used instead of propellant, since the word propellant, for some experts and authors, implies the release of energy through chemical reactions [18] while in electrostatic propulsion the expellant has the only goal of being accelerated and the energy is provided by an electrical external source. In this paper there is no distinction and the author prefers the use of the word propellant also for electric thrusters.

Xenon is most common propellant for electric propulsion because of its ability to

be ionized at relatively low voltages and because of its high molecular mass [10]. Compared with the alternatives like Krypton Argon and Nitrogen it has a higher ionization rate at lower electron energies which increases the mass utilization efficiency and so the specific impulse [10]. The thrust of an Hall thruster running in Xenon is higher for the same applied voltage [16] due to the shorter acceleration zone [13]. Cesium vapor and mercury vapor were considered as alternatives since they have a very low ionization potential (they require less energy to be ionized), but they are not inert gasses. Xenon, moreover, has the highest boiling point and at the highest density making it more convenient to be stored in spacecrafts [10]. Xenon is an inert gas and it is not radioactive like Radon, which has an even lower ionization potential.

1.3.2 Geometry

Figure 1.2 shows the principal components of an Hall thruster [7].

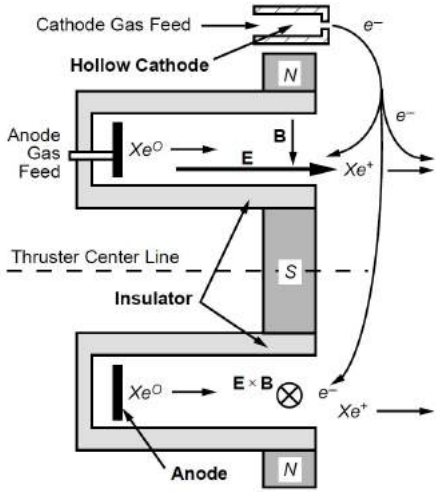

Figure 1.2: Illustration of a generic annular Hall thruster, similar to the Z-70

The principal components are the hollow cathode, the anode and the magnetic coils. Most of the action happens in the annular region near the exit where both the ionization and acceleration take place.

The anode is a ring at the base of the annular section. It is connected with the cathode to the power supply and represents the positive electrode. From there neutral xenon is injected.

The cathode is external to the annular region and represents the negative electrode. From there electrons are expelled. These electrons naturally try to reach the anode, since they are attracted to high potential regions.

The electric field formed between anode and cathode tends accelerate the electrons towards the anode. Plasma is generated from the collision between electrons and neutral xenon particles, in fact when an electron collides with enough energy with a neutral particle the neutral particle loses an electron and becomes a positive ion:

$$Xe^0 + e \rightarrow Xe^{+1} + 2e$$

With the magnetic coils switched off the process generates a low efficiency plasma and little thrust. The engine doesn't work as an Hall thruster without the magnetic field.

The magnetic field generated by the coils is radial near the exit of the annular section as shown in figure 1.2. The magnetic field traps the electrons and doesn't make it easy for them to reach the anode. The electrons are forced into orbit near the exit of the annular region, where they generate an electron grid. The perpendicular magnetic and electric fields are responsible for electrons spiraling in the $E \times B$ direction, according to equation 1.17, and represents the Hall current, which gives the name to the engine.

The vast majority of the xenon particles collides with the electrons and gets ionized and is then accelerated by the electric field to high velocity (in the order of 15,000 m/s for the z-70, but can be much higher) near the end of the annular region. After the annular region, the positive ions join with some of the electrons emitted by the cathode, so the global charge of the engine doesn't change.

This happens also in the gridded thrusters, but they require a cathode just for the neutralization called neutralizer. In Hall thrusters there is just one cathode.

The emitted electrons have three main functions: some of the electrons menage to

reach the anode and close the circuit, some are trapped by the magnetic field and generate the electron cloud responsible for the ionization and acceleration of xenon particles and some don't make it to the annular chamber and form the neutral plasma beam.

The hollow cathode is made of a cylindrical electron emitting material wrapped by a heater. This assembly is covered by a tube made of a refectory material with a orifice in the downstream end. When the heater power supply is turned on and set in current mode, current flows in the heater. The temperature increases and electrons are released by the electron emitting material. These electrons interact with a small amount of gas (argon for the Z-70) which is injected in the cathode tube and generate plasma [7]. The plasma physics inside and outside the cathode is very complex and it is not necessary to get into details in this thesis. The hollow cathode is enclosed in a cylindrical electrode called keeper. The keeper protects the cathode and has the main function of extracting electrons out of the discharge zone. In space qualified thrusters both keeper and heater are used for turning on the thruster and then are turned off. The z-70 needs to have both the keeper and heater on all time.

Figure 1.3: z-70 Hallow cathode

Figure 1.4 shows the electrical connections for an Hall thruster.

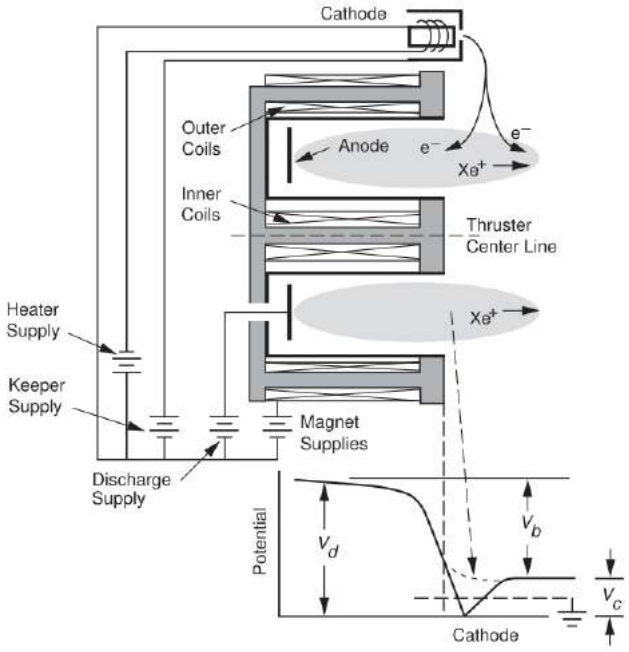

Figure 1.4: Hall thruster circuits [7]

The beam potential V_b is the difference between the discharge potential V_d (provided by the power supply) and the coupling voltage V_c, which is the one required to extract the beam current from the hollow cathode and can be approximated to be equal to the ground potential V_g [7].

$$V_b \approx V_d - V_g \tag{1.18}$$

The anode current is mostly electron current at the anode, since the ion current is negligible due to the higher mass of xenon [7]. Since the cathode current is also negligible the discharge current I_d can be approximated to be equal to the anode current, whose value depends on the operating conditions.

The annular walls of an Hall thrusters must be made of dielectric material with low sputtering yield and low secondary emission [7]. The walls of the Z-70 are made with boron nitride (BN).

1.4 Objectives of the Project

The goal of this thesis project is to measure the thrust of the Z-70 Hall thruster and compare the results to plasma measurements obtained through laser induced fluorescence (LIF) and numerical simulations for the same working point.

In order to precisely measure the thrust of the Z-70 the author proposes and develops some improvements to an instrument called thrust stand, which is able to measure the thrust of an electric engine working in vacuum.

The secondary goal of the thesis is to measure the ion velocity and plasma composition using a Wien filter, or ExB sensor.

A non working Wien filter is taken apart and studied in detail. In order to fix it the author made few modifications which turned out to be successful. The measurements of velocity obtained using this sensor will integrate and enrich the comparison between the results of this thesis, LIF measurements and numerical simulations.

2 Thrust Stand

2.1 Working Principle

A sophisticated sensor called thrust stand is needed to measure the thrust of an Hall thrusters. The thrust stand is able to precisely measure the low thrust generated by an Hall thruster. There are few thrust stands in the world due to their very peculiar application. It is also a very delicate and fragile piece of equipment. The one that is propriety of Stanford University is an inverted pendulum type thrust stand developed by the United States Air Force (USAF) for Stanford University.

The thrust stand is divided in two parts: a moving part, where the thruster is mounted, and a still part. The two parts are connected by two inverted pendulum-like structures made of four thin flexures each. The two structures bend when the moving part is subjected to a force, a magnetic damper allows the structure to converge to a new equilibrium position and to reduce transient oscillations induced by the environment. A linear voltage differential transformer sensor (LVDT, Macro Sensors, model PR 812) is able to sense the displacement of the moving part. An LVDT indicator translates the LVDT signal into a voltage. The change in voltage is, ideally, proportional to the applied thrust, so it is possible to relate the thrust to the voltage readout.

Some of the electrical and propellant lines are connected to the thrust stand and from the thrust stand other lines connect the stand to the thruster, in this way the disturbance on the measurement is reduced. In fact the metallic pipes, carrying gas flow to the anode and the cathode, make large circle around the structure, so the stiffness to the system is reduced to the minimum.

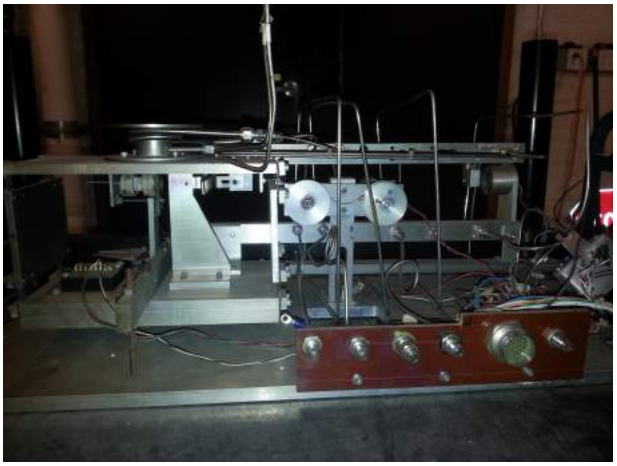

Figure 2.1: Thrust stand

2.2 Old Procedure

2.2.1 Calibration Method

Since the thrust produced by the Hall thruster is very low the calibration process is critical and it could lead to a big error in the measurement if not properly executed.

The moving part of the thrust stand is connected to a calibration mechanism made of a pulley, a spool and three weights and can be seen in figure 2.2.

The small weights, of known mass, are attached to a chain which can wind around the spool and is released by a stepper motor, controlled manually with a switch. The chain hangs on the pulley and is attached to the moving part of the thrust stand.

When the spool rotates the weights are slowly released one by one on the pulley so that the chain can translate the vertical weight in horizontal push to the thrust stand. By adding a known force to the thrust stand and by measuring the displacement it is possible to relate the LVDT voltage to the applied force, this is the working principle of the calibration process. When the calibration process has ended the weights are slowly removed by the stepper motor and winded back around the stool.

In figure 2.2, on the far left, the screw is part of the moving part and it is attached to

the chain, the pulley is the one on the left and the spool is the one on the right. On the lowest part of the chain a red marker helps the operator see when the weights are released.

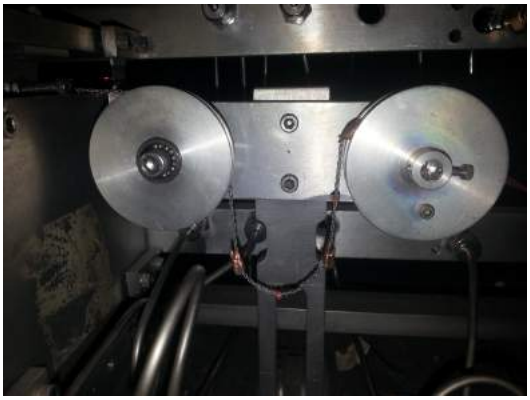

Figure 2.2: Calibration mechanism

It is important to stress that the tests are performed in the vacuum camber facility so all the calibration procedure, including the control of the stepper motor, is performed from the outside of the camber and the monitoring of the weights is performed by looking through one of the portholes.

This calibration system is not precise and errors in the measurement are added due to many sources. The weight of the chain is not taken into account in the old calibration [23] and its value increases as the weights are added to the pulley.

The calibration has two purposes: relating the LVDT voltage to the thrust and determining the drift in the measurement. In fact, after one weight is added and then taken away, the moving part will not return to the same point (the LVDT will read a different equilibrium voltage). The drift is computed numerically for each calibration.

The calibration procedure is properly explained by Young [23], who used this thrust stand last.

Firstly the weights are added one at the time and then taken away one at the time, so the LVDT records a pyramid-like shape, like the one shown in figure 2.3. The base corresponds to the unloaded state and the upper plateau corresponds to all

three weights applied. Fit lines are then computed to represent same loading states (red lines). These lines are then averaged (green line) to approximate the average drift. The drift is subsequently subtracted out of the data to reduce its effect on the measurement.

Next, changes in voltages between different loading states are calculated by averaging the sections of constant loading, in this way the the voltage differences are related to the force applied by the weights.

Then the voltages are plotted against the force applied and finally the linear regression rate is computed in order to have the linear behavior of the thrust stand, since it is expected to be linear.

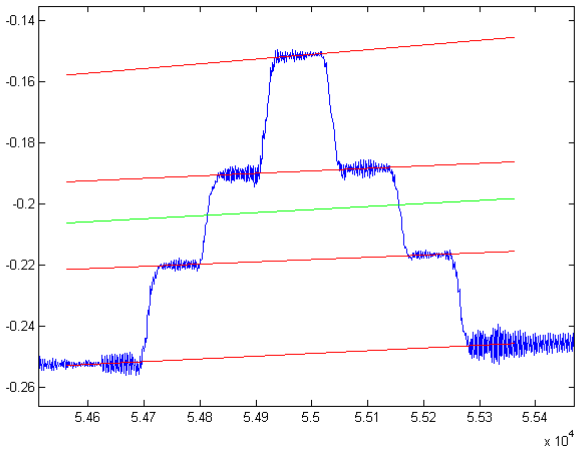

Figure 2.3: Calibration pyramid

2.2.2 Data Acquisition

When the Hall thruster is in the vacuum facility, the data from the LVDT is recorded.

Two pyramids, like the one of the calibration, are obtained by adding and then removing the three weights twice, firstly with the thruster on and then with the thruster off. The value of the thrust is computed by looking at the difference between the two pyramids and comparing the difference with the calibration [23].

Best fit lines are calculated across each plateau of the single pyramids. Then, instead of computing the average voltages with respect to the unloaded state, the average voltages are computed comparing the "thruster on" pyramid with the "thruster off" one [23]. Four voltages are obtained: the first is the difference between the unloaded state "thruster on" and "thruster off", and the other three are the difference between the loaded states with the three different weights. These four voltages are averaged and the average value obtained is approximately due to the thrust only. This value of voltage is compared with the calibration line, that relates the voltage to the thrust, so the thrust is computed.

As Young points out [23], during the "thruster off" acquisition, the gas is still flowing from the thruster and the cathode and this inevitably affects the measure even though this effect amounts for less then 3% of the thrust.

2.3 Proposed Development

2.3.1 New Geometry

The presence of uncertainties in the computed value of thrust, using this instrument, is highlighted by the fact that the thrust stand does not spring back to the old equilibrium position after a force is applied and then removed. This denotes a non linear dissipative behavior, which introduces uncertainties in the computed value of thrust.

The idea is to exploit a current-controlled magnetic force to restore the moving part to the equilibrium condition every time. The moving part just oscillates around the equilibrium position until it reaches convergence, and then it remains still. In this way the dissipative non linear behavior of the thrust stand does not play any role since the thrust stand remains always very close to equilibrium. The value of the force is then computed by looking at how much current is needed to make the moving part remain still in equilibrium condition.

A nice propriety of well-designed sensors is linearity, in this case the relationship between the current and the force would be nice if linear. Since the calibration is done just by adding three weights, it would be impossible to see non linear behavior

of order higher than 3 (considering no weight as a calibration point).

The proposed solution is to attach a small permanent magnet to the moving part and to control the current of a solenoid, aligned and relatively close to the magnet, on the fixed part. Both the permanent magnet and the solenoid produce a magnetic field, the interaction between the magnetic fields produces a resulting force. This force is controlled by controlling the current flowing in the solenoid and must be equal the thrust to have equilibrium.

2.3.2 Mathematical Model

Figure 2.4 shows the mathematical model of the system: the moving part of the thrust stand is modeled as a cart of mass m, k is the equivalent stiffness of the system, d is the damping coefficient of the system (mostly due to the magnetic damper), T is the thrust, f is the control magnetic force and x is the position of the center of mass of the moving part (it is 0 at equilibrium for any value of T).

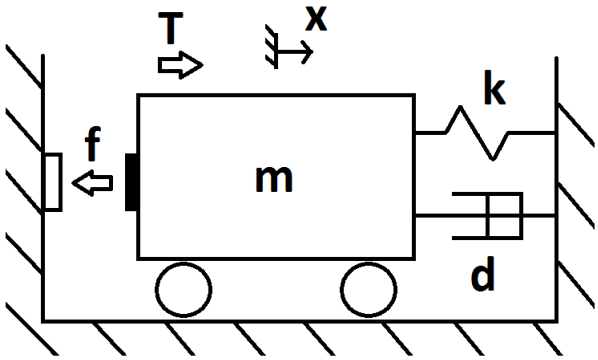

Figure 2.4: Thrust stand model

The force f is represented by an arrow pointing towards the solenoid (white rectangle), while the permanent magnet is attached on the moving part (black rectangle).

The equation governing the system is

$$m\ddot{x} + d\dot{x} + kx = F_{tot} = f + T \tag{2.1}$$

The characterization of f is needed. The interaction between the permanent magnet and the solenoid is modeled as magnetic dipole-dipole interaction. This interaction, as it will be shown, leads to a linear relationship between force and current.

The magnetic dipole is an ideal point magnet, or equivalently it is an ideal infinitesimal current loop with constant magnetic moment [8]. The solenoid and the permanent magnet are not points, but if they are small enough and the distance between the two is sufficiently larger than their characteristic sizes, they can be modeled as such [8].

Figure 2.5 shows the magnetic field generated by the magnetic dipoles.

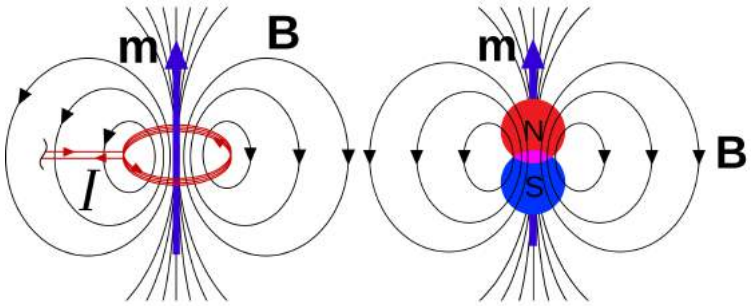

Figure 2.5: Magnetic fields of a dipole for a magnet and for a current loop

The force between two dipoles is

$$\mathbf{F} = \frac{3\mu_0}{4\pi|\mathbf{r}|^4}\left((\hat{\mathbf{r}}\times\mathbf{m_1})\times\mathbf{m_2} + (\hat{\mathbf{r}}\times\mathbf{m_2})\times\mathbf{m_1} - 2\hat{\mathbf{r}}(\mathbf{m_1}\cdot\mathbf{m_2}) + 5\hat{\mathbf{r}}((\hat{\mathbf{r}}\times\mathbf{m_1}))\cdot(\hat{\mathbf{r}}\times\mathbf{m_2})\right) \tag{2.2}$$

Where μ_0 is the permeability constant in vacuum, $\mathbf{r}$ is the distance vector from the solenoid to the permanent magnet and $\mathbf{m_1}$ and $\mathbf{m_2}$ are respectively the magnetic moment of the solenoid and of the permanent magnet.

The magnetic moment is a vector from the south pole to the north pole and it is the most important characteristic of a magnetic dipole. For convenience the force f in figure 2.4 points in the direction of the arrow when the current is positive. The magnetic dipoles have the same directions: the north pole of the magnet is on the

side attached to the cart (moving part). The vector **r** has the same direction of the magnetic dipoles. Figure 2.6 shows the direction of the vectors.

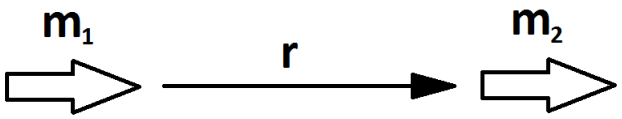

Figure 2.6: Vector positive direction

Moreover $\mathbf{m_1}$, $\mathbf{m_2}$ and **r** are parallel, so the cross products are null and equation 2.2 simplifies:

$$\mathbf{F} = -\frac{3}{2}\frac{\mu_0 m_1 m_2}{\pi r^4}\hat{\mathbf{r}} \tag{2.3}$$

Where m_1, m_2 and r are the norms of the respective vectors. The force **F** has opposite direction due to the minus, and it makes sense since the magnetic moment points always in the north direction (if the situation is the one in figure 2.6 the force is attractive).

The magnetic moment of the solenoid depends on the current i, the number of turns N and the section area A:

$$m_1 = iAN \tag{2.4}$$

Equation 2.3 becomes:

$$\mathbf{f} = -\frac{3}{2}\frac{\mu_0 iAN_1 m_2}{\pi r^4}\hat{\mathbf{r}} \tag{2.5}$$

As it is possible to see from equation 2.5 the relationship between force and current is linear, as pointed out before this is a much desirable quality for sensors. Equation 2.5 is linear with respect to the current, but not with respect to the distance between the solenoid and the permanent magnet.

The distance between solenoid and magnet r is the distance at rest r_0 minus the displacement from equilibrium x:

$$r = r_0 - x \tag{2.6}$$

The minus is due to the fact that, as it can be seen from figure 2.7 and unlike the sketch in figure 2.4, if x is positive the solenoid and magnet get closer (r decreases). Equation 2.5 becomes:

$$\mathbf{f} = -\frac{3}{2}\frac{\mu_0 i A N_1 m_2}{\pi (r_0 - x)^4}\hat{\mathbf{r}} \tag{2.7}$$

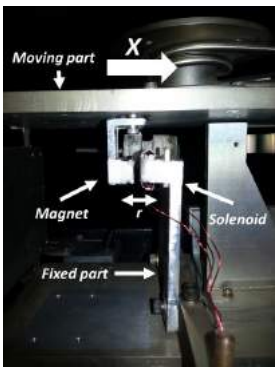

Figure 2.7: Solenoid and magnet

2.3.3 Control System

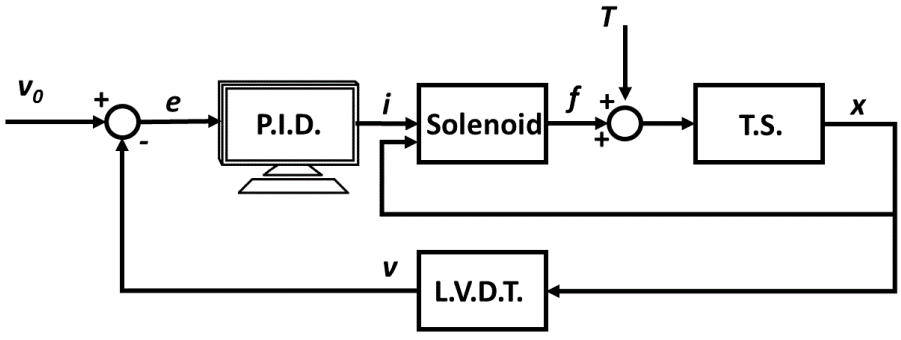

Figure 2.8: Closed-loop system

Figure 2.8 shows the closed-loop control system. T.S. is the thrust stand, modeled as in figure 2.4 (mass, spring, damper system).

v_0 is the setpoint of the control loop. When the control system is turned on a value for the output of the LVDT is chosen and it becomes the setpoint value for the control loop.

At any time v_0 is compared with the output of the LVDT v, the difference between the two values is the error e, if it is null the system is at equilibrium, if it is different from zero the system is not at equilibrium.

The P.I.D. controller reads the value of the error e and produces an output which is proportional to the value of the error (proportionality constant k_p), its derivative (proportionality constant k_d) and its integral value (with zero as initial value, proportionality constant k_i).

$$i = k_p e + k_d \dot{e} + k_i \int e \tag{2.8}$$

In the real case the output of the PID control system is a voltage. This control voltage is the input to a power supply which is able to generate a current proportional to the voltage, so effectively the system can be seen as producing a current proportional to the error e, its derivative and its integral.

The values of the proportionality constants determine the performance of the system. The output of the P.I.D. is the current flowing in the solenoid, provided by the power supplier.

The current flows inside the solenoid and produces a magnetic field, which interacts with the permanent magnet and produces a force f. The force f depends nonlinearly with the value of the displacement x.

The force on the thrust stand is the sum of the magnetic force f and the thrust T. The total force acts on the thrust stand which, as a response, moves by a value of displacement x. The displacement x is measured by the LVDT and translated into a voltage v. The value of v is then compared with the value of voltage at equilibrium v_0 and the loop is closed.

2.3.4 Stability Analysis

Firstly a linear analysis is performed to understand the behavior of the system around equilibrium with and without the closed-loop.

The non linearity comes from the equation 2.7: the magnetic force depends to the fourth power of the displacement x. This equation can be linearized around the equilibrium condition using the first order Taylor expansion. In particular, for a two-variable equation $f(i,x)$ (equation 2.7), the first order Taylor expansion is:

$$f(i,x) \cong f(i_0,x_0) + f_{/i}(i_0,x_0)\cdot(i-i_0) + f_{/x}(i_0,x_0)\cdot(x-x_0) \tag{2.9}$$

For the thrust stand the equilibrium condition is when $x = 0$ and i_0 is the value of the current needed to compensate the thrust. For simplicity $(i-i_0)$ will be called just i and it is the oscillation of current near equilibrium.

The values of the derivatives are:

$$f_{/x} = -\frac{6\mu_0 i A N m_2}{\pi(r_0-x)^5} \tag{2.10}$$

$$f_{/i} = -\frac{3}{2}\frac{\mu_0 A N m_2}{\pi(r_0-x)^4} \tag{2.11}$$

The linearized force becomes

$$f(i,x) \simeq -\frac{3}{2}\frac{\mu_0 i_0 A N_1 m_2}{\pi r_0^4} - \frac{3}{2}\frac{\mu_0 A N m_2}{\pi r_0^4} i - \frac{6\mu_0 i_0 A N m_2}{\pi r_0^5} x \tag{2.12}$$

At equilibrium, in steady-state condition ($i = 0$ and $x = 0$), this force must be equal to minus the thrust (because it has to counteract it), so:

$$-\frac{3}{2}\frac{\mu_0 i_0 A N_1 m_2}{\pi r_0^4} = -T_0 \tag{2.13}$$

Where T_0 is the thrust that for simplicity, at this stage, it is approximated to be linear.

Equation 2.12 becomes:

$$f(i,x) = -T_0 - \frac{3}{2}\frac{\mu_0 A N m_2}{\pi r_0^4} i - \frac{6\mu_0 i_0 A N m_2}{\pi r_0^5} x \tag{2.14}$$

To lighten the notation, the value of a is introduced:

$$a \triangleq \frac{\mu_0 A N m_2}{\pi r_0^5} \tag{2.15}$$

a is positive since it is defined as products and divisions of positive terms.

The force $f(i,x)$ becomes:

$$f(i,x) = -T_0 - \frac{3}{2} a r_0 i - 6 a i_0 x \tag{2.16}$$

Approximating $T = T_0$ (constant thrust), the total force F_{tot} (sum of the force f and the thrust T) is obtained:

$$F_{tot} = -6 a i_0 x - \frac{3}{2} a r_0 i \tag{2.17}$$

The equation of motion becomes:

$$m\ddot{x} + d\dot{x} + kx = -6 a i_0 x - \frac{3}{2} a r_0 i \tag{2.18}$$

Which is a linear relation. Moving the linear term in x on the left side:

$$m\ddot{x} + d\dot{x} + (k + 6 a i_0) x = -\frac{3}{2} a r_0 i \tag{2.19}$$

Since a is positive the solenoid adds a positive contribution linear to x. This is equivalent to increasing the stiffness of the system, so enhancing the stability (the poles are moved further away from the unstable region).

The stability of equation 2.19 depends on the shape of the current i, which is controlled by the P.I.D. controller.

The output of the LVDT is a voltage that is ideally proportional to the displacement x by a value of k_{LVDT}:

$$v = k_{LVDT} x \tag{2.20}$$

For simplicity, and without loss of generality, the value of v_0, which is the output of the LVDT in equilibrium condition, is set to 0. The value of the error e is equivalent to the value of the output voltage v.

$$e = v$$

Substituting equation 2.20 into the P.I.D. equation 2.8

$$i = k_p v + k_d \dot{v} + k_i \int v = k_p k_{LVDT} x + k_d k_{LVDT} \dot{x} + k_i k_{LVDT} \int x \tag{2.21}$$

To simplify the stability analysis the value of k_i is set to zero, so it is possible to go further with the stability analysis remaining in the time domain, the effect of the integral constant will be discussed later on.

$$i = k_p k_{LVDT} x + k_d k_{LVDT} \dot{x} \tag{2.22}$$

Substituting the value of the closed-loop current (equation 2.22) in equation 2.19:

$$m\ddot{x} + d\dot{x} + (k + 6ai_0)\, x = -\frac{3}{2} a r_0 k_p k_{LVDT} x - \frac{3}{2} a r_0 k_d k_{LVDT} \dot{x} \tag{2.23}$$

Moving the terms on the right hand side:

$$m\ddot{x} + \left(d + \frac{3}{2} a r_0 k_d k_{LVDT}\right) \dot{x} + \left(k + 6ai_0 + \frac{3}{2} a r_0 k_p k_{LVDT}\right) x = 0 \tag{2.24}$$

Positive terms are added to both the damping coefficient and the stiffness coefficient, so the system is made even more stable by the control loop, since the stability of the system increases if the positive coefficients of the characteristic polynomial increase. The derivative constant k_d adds to the damping of the systems.

To compute the closed-loop transfer functions it is necessary to compute all the transfer functions in the closed-loop in figure 2.8.

For the P.I.D. block the transfer function is computed from equation 2.8, which, in the Laplace domain is:

$$I(s) = \left(k_p + sk_d + \frac{1}{s}k_i\right) E(s) \tag{2.25}$$

The transfer function, which is the input-output relation between current and the error, is:

$$G_{PID}(s) = \frac{I(s)}{E(s)} = \frac{sk_p + s^2k_d + k_i}{s} \tag{2.26}$$

The input-output relation for the actuator (solenoid and magnet interaction) is more complex because it relates two values (the current i from the P.I.D. control and the displacement x): it is a vector of transfer functions. The input of the thrust stand block is the total force F_{tot}, which is the sum of the thrust T and the control force F. In the most general case the thrust is not constant and can be modeled as a constant part T_0 plus a variable part T_r.

$$T = T_0 + T_r \tag{2.27}$$

The total force F_{tot} becomes:

$$F_{tot}(s) = F(s) + T_0 + T_r(s) \tag{2.28}$$

The control force $F(s)$ in the Laplace domain can be computed from equation 2.16:

$$F(s) = -T_0 - 6ai_0X(s) - \frac{3}{2}ar_0I(s) \tag{2.29}$$

The total force becomes:

$$F_{tot}(s) = -6ai_0X(s) - \frac{3}{2}ar_0I(s) + T_r(s) \tag{2.30}$$

The total force can be represented in matrix notation:

$$F_{tot}(s) = \begin{bmatrix} -6ai_0 & -\frac{3}{2}ar_0 \end{bmatrix} \begin{Bmatrix} X(s) \\ I(s) \end{Bmatrix} + T_r(s) = \mathbf{G_{sol}} \begin{Bmatrix} X(s) \\ I(s) \end{Bmatrix} + T_r(s) \quad (2.31)$$

Where $\mathbf{G_{sol}}$ is the vector transfer function representing the solenoid-magnet interaction.

$$\mathbf{G_{sol}} = \begin{bmatrix} G_{sol,1} & G_{sol,2} \end{bmatrix} \begin{Bmatrix} X(s) \\ I(s) \end{Bmatrix} \quad (2.32)$$

The transfer function of the LVDT is ideally trivial and is:

$$V(s) = G_{LVDT} X(s) \quad (2.33)$$

$$G_{LVDT} = k_{LVDT} \quad (2.34)$$

Now it is possible to put the transfer functions together. The relationship between them is the one represented in figure 2.8 and is better visualized in the Laplace domain in figure 2.9.

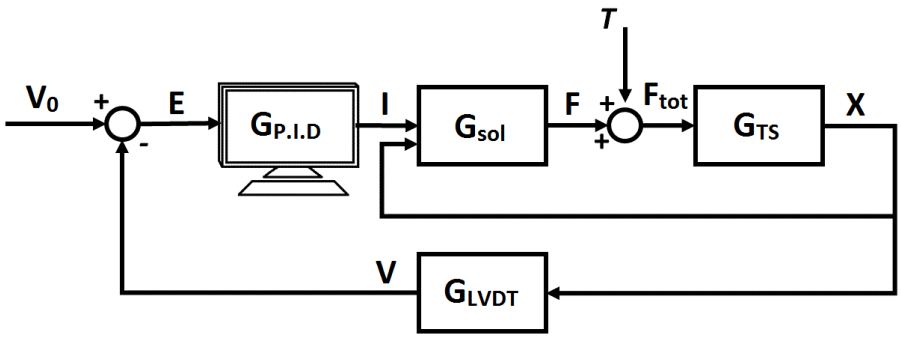

Figure 2.9: Closed-loop in Laplace domain

Now, thanks to the proprieties of the Laplace domain, the input-output relation between the current I and the displacement X can be computed using just sums and

multiplications.

Starting from the relationship between the displacement X and the total force:

$$X(s) = G_{TS}F_{tot(s)} = G_{TS}\begin{bmatrix} G_{sol,1} & G_{sol,2} \end{bmatrix}\begin{Bmatrix} X(s) \\ I(s) \end{Bmatrix} + G_{TS}T_r(s) \tag{2.35}$$

In scalar form (implying from now on the dependence on the Laplace variable s):

$$X = G_{TS}G_{sol,1}X + G_{TS}G_{sol,2}I + G_{TS}T_r \tag{2.36}$$

Making some simple algebraic manipulations:

$$X = \frac{G_{TS}G_{sol,2}}{1 - G_{TS}G_{sol,1}}I + \frac{G_{TS}}{1 - G_{TS}G_{sol,1}}T_r \tag{2.37}$$

The current I is related to the error E through G_{PID}, moreover the error E can be approximated to be equal the the output voltage of the LVDT V (as it was done for the time domain stability analysis). The value of v_0 adds nothing to the theoretical framework, it is just a constant value and will come into play during the actual implementation of the control system.

The voltage V is proportional to the displacement X (equation 2.33).

$$I = G_{PID}G_{LVDT}X \tag{2.38}$$

Equation 2.37 becomes:

$$X = \frac{G_{TS}G_{sol,2}G_{PID}G_{LVDT}}{1 - G_{TS}G_{sol,1}}X + \frac{G_{TS}}{1 - G_{TS}G_{sol,1}}T_r \tag{2.39}$$

Which leads to:

$$X = \frac{1 - G_{TS}^2G_{sol,1}}{1 - 2G_{TS}G_{sol,1} - G_{TS}G_{sol,2}G_{PID}G_{LVDT} - G_{TS}^2G_{sol,1}G_{sol,2}G_{PID}G_{LVDT}}T_r = G_{XT}T_r \tag{2.40}$$

Where G_{CL} is the close-loop transfer function that relates the thrust.

Starting from equation 2.36 and 2.38 it is also possible to compute the close-loop transfer function that relates the current and the external thrust, which is:

$$I = \frac{G_{PID}G_{LVDT}G_{TS}}{1 - G_{TS}G_{sol,1} - G_{TS}G_{sol,2}G_{PID}G_{LVDT}}T_r = G_{IX}T_r \tag{2.41}$$

It is worth noting that the transfer functions can only be computed for small oscillation around the equilibrium, because the equations are linearized. The non-linear model cannot be studied with this simple mathematical modeling.

2.3.5 Simulink Model

The non-linear behavior of the system can be modeled with Simulink. The Simulink model (figure 2.10) simulates the thrust stand in terms of dynamics of the closed-loop system. The coil box simulates the interaction between magnet and solenoid with the dipole-dipole approximation.

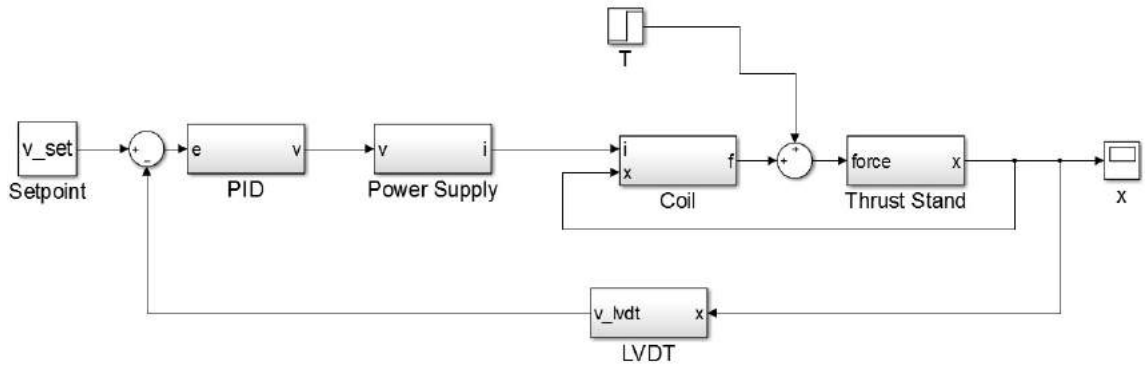

Figure 2.10: Simulink model

Figure 2.11 shows the response of the system in terms of solenoid current and position of the moving part when the system is subjected to a step force of 30mN.

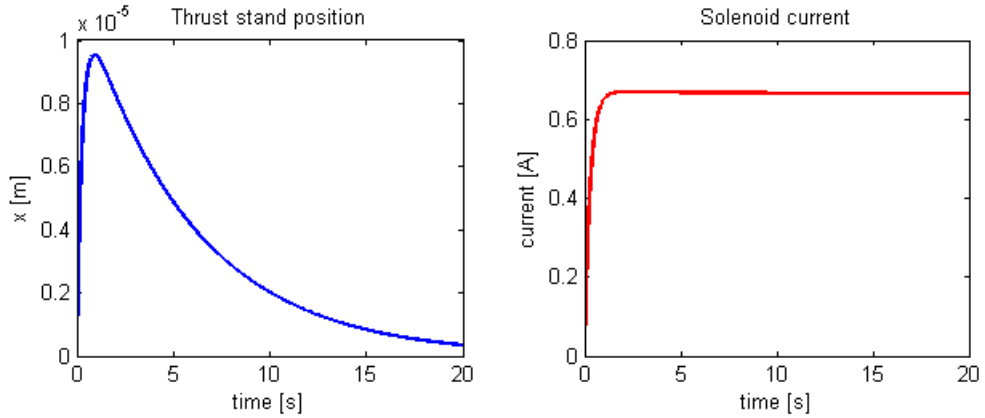

Figure 2.11: Simulink thrust stand simulation

The displacement x increases as soon as the thuster turns on, consequently the current increases as well. The force generated by the interaction between the solenoid and the magnet restores the thrust stand to its original position. The final value of the current is proportional to the thrust.

Figure 2.12 compares the real position (LVDT output) with the simulation. The real value was computed in vacuum with all the lines and cables plugged in.

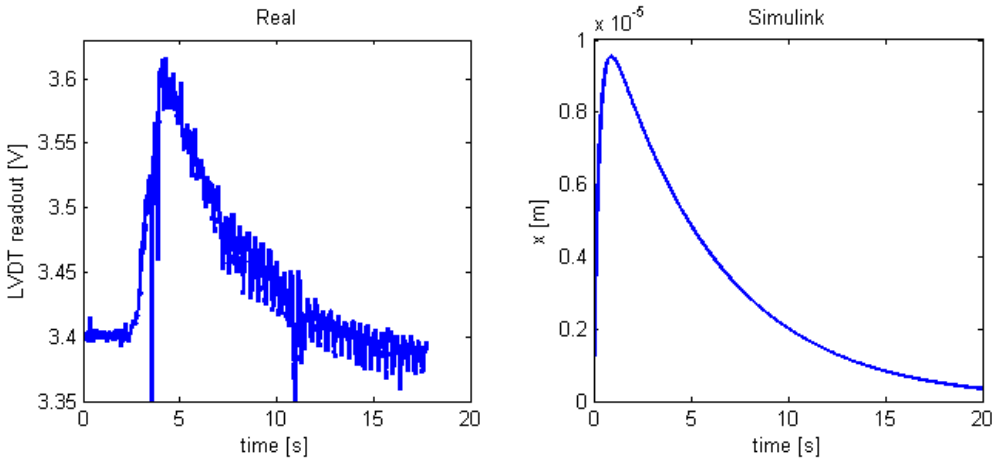

Figure 2.12: Real position vs Simulink model

As it can be seen the lines and cables introduce additional vibrational modes which are not included in the model.

The mass, stiffness and damping coefficient used in the simulation are not precise since it was not possible to actually measure them. They were estimated by looking at the response of the system to external outputs.

2.4 Simulation Modeling

2.4.1 Geometry

The figure 2.13 shows the modeled geometry of the problem.

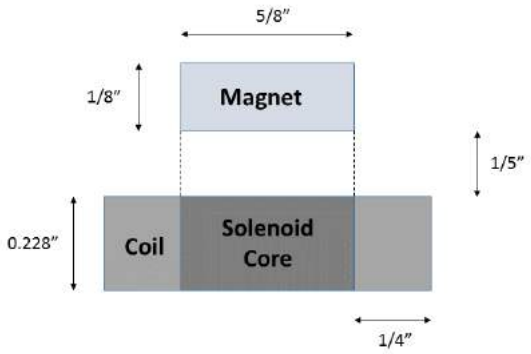

Figure 2.13: Solenoid magnet geometry (not in scale)

How the solenoid was done and the characteristics of the magnet will be explained later.

2.4.2 Real Physics Prediction using FEMM

FEMM (Finite Element Method Magnetics) is a free software and a very powerful tool for simulating symmetric magnetic problems. In this particular case the symmetry is axisymmetric, since both the solenoid and the magnet are cylindrical.

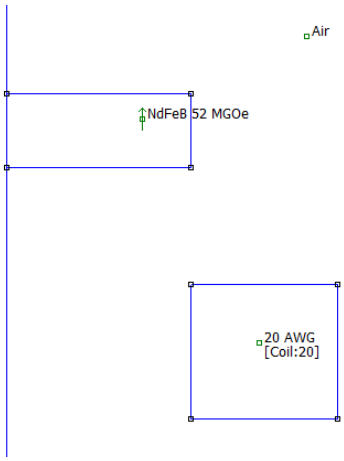

Figure 2.14: FEMM model axial symmetric

The software asks for the 2D geometry in the axial and radial direction and computes the axisymmetric solution. The geometry of the solenoid is the geometry of the coil, since the core is passive (air-core solenoid).

The magnet material is set to be NdFeB 52 MGOe which is the strongest kind of neodymium magnet on the market. Since the real value in MegaGauss-Oersted will be lower than 52, the real magnet will be somewhat weaker than the model magnet (not much).

The solenoid material is set to be copper wire 20 gauge. The real wire is 21 gauge but the software has only even gauges in the material library. The number of coils is 20 as in the real case.

Air is the passive medium in the software, so it is equivalent to vacuum.

The solution was obtained in 154559 nodes, by solving the finite element problem over 307653 elements. The quality of the mesh was increased until the force on the magnet due to the solenoid is close to the force on the solenoid due to the magnet. The two theoretically have to be equal thanks to Newton's third principle, but the finite element method introduces errors in the solution so for a coarse mesh the two forces are sensibly different.

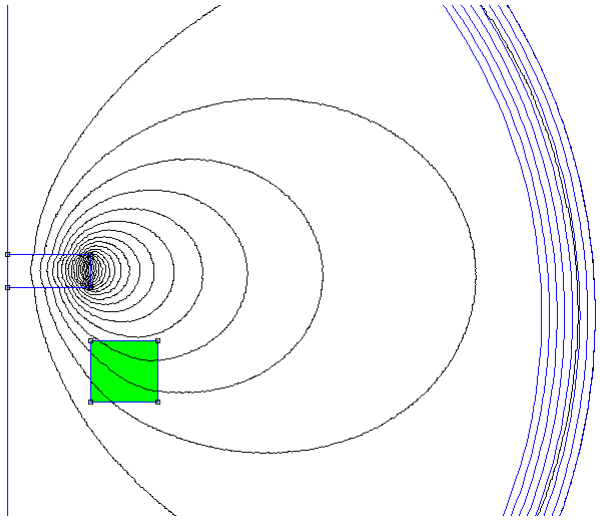

Figure 2.15: FEMM solution

Figure 2.15 shows the solution in terms of magnetic field isolines in Tesla.

The main source of magnetic field is the permanent neodymium magnet. The magnetic field generated by the solenoid (highlighted in the figure) is not visible since it it very weak also for the maximum current it can sustain.

The solution in terms of force generated, which is the solution of interest, was computed for several values of current. Table 2.1 shows the results obtained.

i [A]	F [mN]
0	0.980981
1	43.1639
2	85.3611
3	127.572
4	169.798
5	212.037

Table 2.1: FEMM current vs force

The software computes a very small value of force for no current, due to the interaction between copper wire and the magnet.

An increase of 1 Ampere in current leads to an increase of approximately 42 mN of force.

The values are graphically presented in figure 2.16.

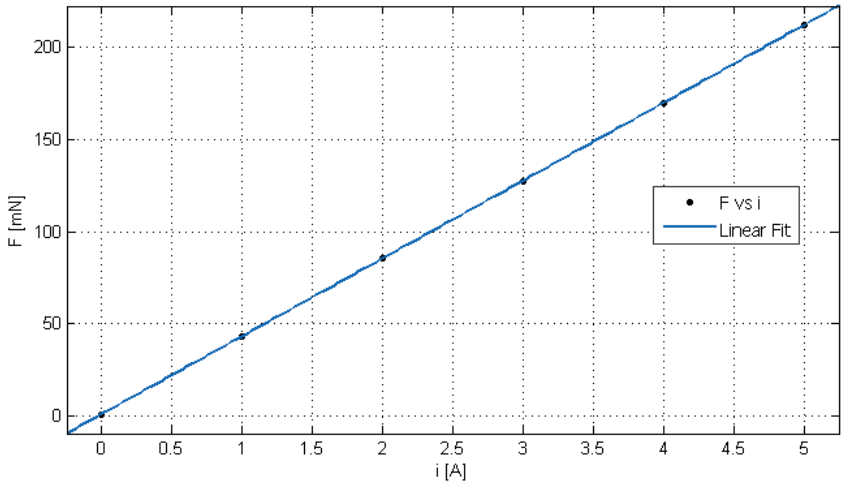

Figure 2.16: Force vs current FEMM

The force varies linearly with the current and this is a very nice propriety as explained earlier, since it means that only few points are enough to calibrate the instrument (theoretically just two) .

The goodness of the fit is summarized in table 2.2.

SSE	0.001863
RMSE	0.021583

Table 2.2: Goodness of linear fit

SSE is the residual sum of squared errors of prediction and RMSE is the root-mean-square error. Both values are very small, so the linear approximation is a good approximation.

2.4.3 Comparison Between FEMM Results and Dipole-Dipole Interaction

The FEMM model and the dipole-dipole model can be compared in order to see the difference between the two models. The FEMM model is more accurate since it takes into account the geometry and solves directly the Maxwell equations to obtain the result.

In order to make the comparison the distance between the two dipoles, for the dipole-dipole interaction, is set to be the maximum axial distance between the magnet and the solenoid (figure 2.17), since that distance gives comparable results.

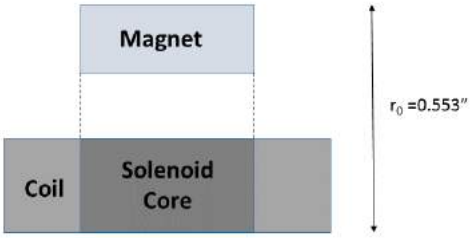

Figure 2.17: Distance between solenoid and magnet in the dipole-dipole model

The dipole-dipole interaction would give much higher results if the distance r_0 (distance at equilibrium) was set to be the distance between the middle points of the solenoid and the magnet. The reason for that is because the magnetic field lines, in the dipole-dipole interaction, are much denser and for this reason a greater number of lines, generated by the point dipoles, interacts with one another. Defining the distance as in figure 2.17 leads to better results.

Table 2.3 summarizes the comparison between the two models.

i [A]	F_{FEMM} [mN]	F_{dd} [mN]
0	0.980981	0
1	43.1639	45.1538
2	85.3611	90.3077
3	127.572	135.462
4	169.798	180.615
5	212.037	225.769

Table 2.3: FEMM vs dipole-dipole model varying current

The results of the two models are comparable. The dipole-dipole interaction model gives approximately 7% higher results.

Another comparison can be done for different values of distance and same value of current. The results, computed for 3 Ampere of current and getting magnet and solenoid closer and further away by 1 mm, are shown in table 2.4.

Δr [mm]	F_{FEEM} [mN]	F_{dd} [mN]
-1	151.730	182.020
0	127.572	135.462
+1	107.992	102.883

Table 2.4: FEMM vs dipole-dipole model varying distance

The result of the dipole-dipole model remains within 20%. The force becomes higher and higher as the magnet and the solenoid get closer and consequently the model becomes less and less precise.

In conclusion the dipole-dipole model is pretty accurate with respect to the FEMM analysis if we define r_0 as the maximum axial distance.

The FEMM analysis was exploited for the sizing of the system in terms of magnet material and size, solenoid diameter and number of coils, distance between solenoid and magnet.

2.5 Improvements Implementation

2.5.1 Solenoid

The solenoid was made by winding a 21 gauge wire around an acrylic support. The acrylic support was done using the laser cutter to cut the core and the external washers.

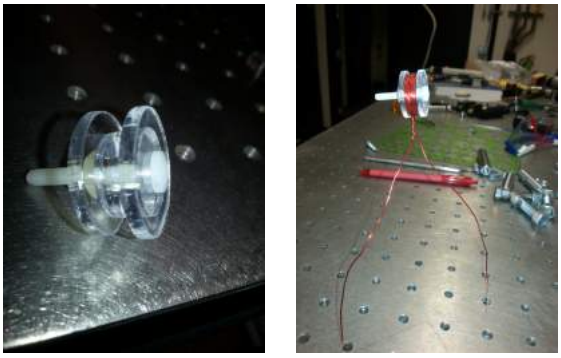

Figure 2.18: Solenoid

The washers and the screw were used for the making and testing of the solenoid but are not part of the final configuration.

The solenoid was then tested at different values of currents. At 5 A and approximately 1.78 W the solenoid got moderately hot (the temperature was not measured), but seemed to be able to dissipate the power. At 6 A and a power of 2.90 W the solenoid got very hot and the plastic core started to melt and to produce the characteristic smell of burning plastic.

It is important to note that the solenoid was tested in air and a temperature of approximately 70 řF (lab conditions). In vacuum the conditions for heat dissipation are much worst because there is not the possibility to exchange heat by convection, but only conduction and radiation.

2.5.2 Permanent Magnet

The magnet used for this implementation is a neodymium magnet. Neodymium magnets are the most powerful magnets and they are almost impossible to demagnetize. Since they are very powerful, a small cylindrical magnet is enough for the thrust stand control system.

A neodymium magnet is an alloy made of neodymium, iron and boron forming a tetragonal crystalline structure $Nd_2Fe_{14}B$. It is a relative new technology since it was invented in 1982. Neodymium magnets are characterized by the grade and it is indicated as a two-digit number following the letter N. The grade indicates how concentrate the magnet is, the higher the grade the stronger the magnet, comparing two magnets of the same size and geometry (and temperature). The grade number is the maximum energy product in MGOe (MegaGauss-Oersted), that is the maximum of the product BxH in the second quadrant of the hysteresis loop (demagnetization curve) expressed in MegaGauss-Oersted. In real life it is impossible to produce two equal magnets, so the industry has accepted a range of acceptable value for each grade (for example N52 magnets can have a real grade between 50 and 52 MGOe). Some sellers (like the one the magnet was bought from) don't explicitly tell the grade of the magnets they sell, but just the pull. The pull is a characteristic of a magnet of any kind and, unlike the grade, it depends on the shape and the size of the magnet. It is defined as the maximum mass (usually expressed in lb) of an unpainted iron plate that can be lifted if attached to the surface of the magnet.

The magnet chosen is a neodymium nickel-plated disc magnet 5/8" in diameter and 1/8" in thickness with a declared pull force of 10 lb maximum. A simulation, done using an online free software, estimates the grade of the magnet to 52, which is the most powerful grade. It is worth noting that all neodymium magnets are very powerful and the estimation of the grade of the neodymium magnet is not so important. In fact a change of 1 grade corresponds, roughly, to a change of 1% of strength. The difference between a N47 and N52 magnet is only approximately 5%.

Coating is necessary for neodymium magnet since the $Nd_2Fe_{14}B$ oxidizes in air. For the Neodymium magnet chosen the coating is nickel (also the most common).

Figure 2.19: Neodymium magnet

2.5.3 Shunt Resistor

Figure 2.20: 1 Ω Shunt resistor

A 1 Ω shunt resistor was used to measure the current flowing in the solenoid. Since it was installed in series with the solenoid the voltage drop across the resistor is equal to the current flowing in the line. This voltage drop is then measured by the A/D converter and read and saved by the computer as shown in figure 2.23.

The precision of the resistor is $\pm 1\%$, but its value is not important for the measurement of thrust, the only important feature is that the value of the electric resistance must remain constant in order to show a value that is proportional to the current flowing. The resistor must also be able to dissipate a lot of power, the model chosen is able to dissipate up to 25W, which corresponds to 5 A. The current flowing in the solenoid must not exceed 5 A in order to not burn the resistor.

2.5.4 Power Supply

The power supply used is Sorensen dlm 40-15. It can produce a maximum output voltage of 40 V and maximum output current of 15 A. This particular model was chosen because its output can be analogically controlled by a input voltage, so it can easily be used inside a control loop.

Figure 2.21: Sorensen dlm 40-15

2.5.5 Analog to Digital Conversion

The A/D converter used is the National Instrument USB-6009 shown in figure 2.22.

Figure 2.22: NI USB-6009 A/D converter

The A/D allows the computer to send voltage signals to the power supply and receive voltage signals from the LVDT meter, the shunt resistor and the stepper motor.

2.5.6 Stepper Motor Control

The stepper motor is used to release the chain with the weights so they can be used for the calibration of the thrust stand. The motor rotates according to a input voltage which is controlled by a remote switch. The switch controls a AC/DC converter with a constant output of 5 V. The switch changes the voltage to ± 5 V or 0 V, according to the position of the switch. When the voltage is 0 V the motor remains still, ± 5 V make the motor rotate in the two opposite directions.

The input of the stepper motor is connected to the A/D converter and read by the computer, which computes the position of the motor by knowing its input voltage.

2.5.7 Circuits

Figure 2.23 shows the electrical connections.

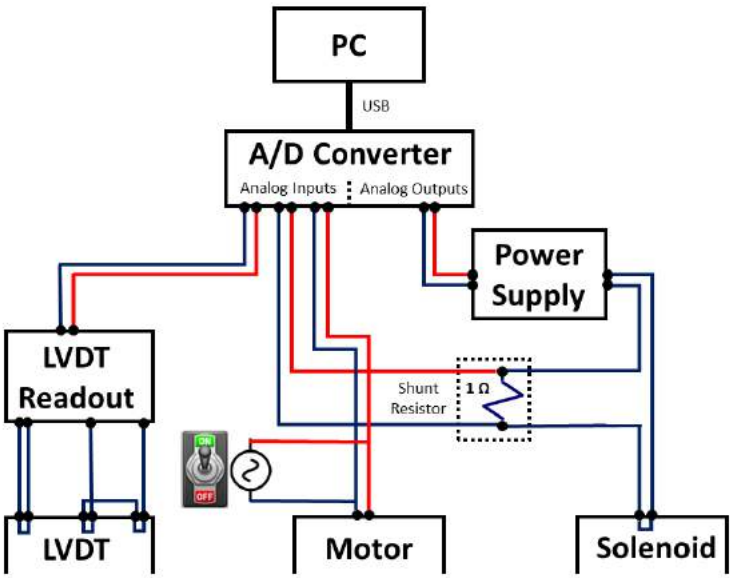

Figure 2.23: Circuit connections

The LVDT (LVDT) has six outputs of which two must be shortened for it to work,

figure shows the scheme of an LVDT. The details on hot it works are not covered by the thesis.

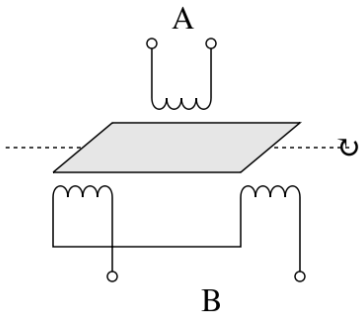

Figure 2.24: LVDT

The output of the LVDT must be read by another instrument. The LVDT meter (PML 1000 LVDT Readout) translates the output of the LVDT into a voltage that is proportional to the displacement (it also shows the value on a screen). This voltage is read by the A/D converter.

The stepper motor is connected to the board too as shown in figure 2.23. The motor is controlled by a toggle switch, and the voltage is read and analyzed by the computer.

The A/D converter generates, as output, the input to the power supply which translates it to a proportional current. The 1 Ω shunt resistor, in series, generates a voltage drop at its ends that is approximately equal to the current. The ends of the shunt resistor are connected to the A/D converter.

The A/D converter is connected to the computer by a USB cable.

2.5.8 Supports and Thruster Mount

Supports were needed to attach the solenoid to the fixed part, the magnet to the moving part and also the thruster to the thrust stand.

Since it is important that the force produced by the interaction between the solenoid and the magnet is totally transferred to the moving part the supports for the solenoid

and the magnet were done in aluminum. Aluminum is sufficiently stiff and it is non-magnetic.

Aluminum was cut using a vertical sew and a vertical drill into the desired shape and then kept in position by screws and bolts.

The support for the Hall thruster cannot be done in aluminum, since the Hall thruster needs to be electronically floating in order to work properly. The support was laser cut in acrylic using a laser cutter. An optical post was used to raise the thruster as it can be seen in figure 2.25 (right). The thruster was raised so the plume of plasma did not hit the thrust stand itself. The post was chosen to be quite tall to allow the possible future use of the cooling system, which was not used for this thesis.

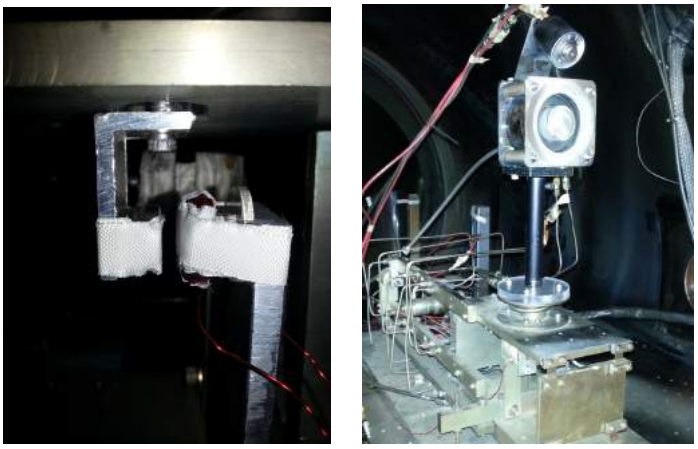

Figure 2.25: Magnet and solenoid supports (left) and Z-70 support (right)

2.6 Testing of the Improvements

2.6.1 Implementation of the Closed-Loop using LabVIEW

The control logic behind the control system was developed in LabVIEW and can be found in the appendix.

The first input is the LVDT readout output. This voltage is read by the computer, then the signal is filtered and averaged to reduce the noise. In particular the cutoff frequency of the second order low-pass filter is 0.5 HZ and the system waits for

50 measurements to make the average of the value. The filtered value becomes the process variable of the PID control system. The output of the PID control system is then limited so the current is never negative (not admissible for the power supply) and not higher then 5 A (limit current for both the solenoid and the shunt resistor).

The second input is the voltage drop across the shunt resistor. This value is the measure of current flowing through the solenoid, the value is printed on screen.

The third input is the input of the stepper motor. Since the stepper motor has a minimum input voltage below which it doesn't rotate ($\pm$ 0.9 V), the control system waits for the voltage to be higher than that value before computing the rotation (this is implemented in LabView using a case structure). The value is then integrated. Since the rotational speed of the motor is proportional to the input voltage, the angle of rotation is proportional to the integral of the input voltage. The value of the integral is shown on screen while the system operates and it is used to control the position of the weights of the calibration system when the thrust stand is not visible from the outside. This will be very useful in the future when the thrust stand will be covered by the cooling system and a visual inspection will be impossible.

2.6.2 PID Tuning

The tuning of the PID has been done heuristically because the real condition is much different from the ideal condition. The 1D mass-spring-damper model is a very good model for the thrust stand, but the power lines and the gas lines, that are connected to the thruster when it is inside the chamber, make it non linear since they tend to vibrate on their own modes. The speed of the control and other performance parameters are not very important for this application because the dynamic characterization of the thrust is not needed, just the static value is of interest. For this reason the most important performance parameter is the robustness of the control: the control system must be able to work even if the system is non linear and there are additional vibrational inputs. In particular the vibrational inputs come from the induced vibration of the lines, the low frequency vibration introduced by the thruster and also from the vacuum chamber. In fact the vacuum chamber introduces some low frequency vibrations while the cryopumps are working. The sum of all these vibrations must be compensated and kept under control by the PID control system.

Table 2.5 summarizes the best vales for the PID control.

k_p	k_i	k_d
0.400	0.007	0

Table 2.5: PID tuning

The derivative constant must be zero for the system to be stable. This is because of the high frequency noise that, even with the filters, makes the derivative of the signal very high and not indicative of the behavior of the system.

The proportional constant is a relative low number because it makes the system more robust even if slower. The integral constant is a relative low value for the same reason, an higher vale would make the system overshoot and under-damped. That would make the system faster, but more sensible to low frequency higher-order vibrations.

2.6.3 Calibration

The calibration of the thrust stand has been done in two ways.

An initial calibration was performed with the help of a cup attached to the chain as shown in figure 2.26.

The weights, which are just cut up pieces of wire, were firstly precisely measured and then added in the cup using tweezers as shown in figure 2.26.

Figure 2.26: Calibration cup (left) and scale with the weights (Right)

The pulley transfers the load to the thrust stand. The control system adjusts the value of the current until the system is again in equilibrium. Figure 2.27 shows the calibration points.

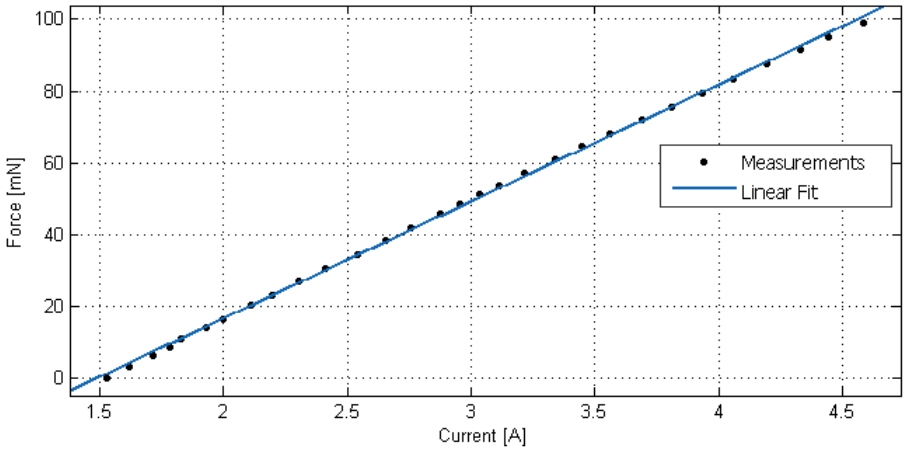

Figure 2.27: Calibration using the cup

A change in 1 A of current corresponds to a force generated of 32.59 mN

The goodness of the fit is summarized in table 2.6.

SSE	18.59
RMSE	0.8148

Table 2.6: Goodness of linear fit

SSE is the residual sum of squared errors of prediction and RMSE is the root-mean-square error.

The problem with this calibration system is that it can be used just to characterize the instrument but not for actually calibrating it because it needs someone who inserts and takes out the weights in and from the cup and that is not possible inside the vacuum chamber.

The second calibration method is the one that is actually used for calibrating the instrument because it can be used also when the thrust stand is inside the chamber.

The stool (on the right of every picture in figure 2.28) is controlled by the stepper motor and, while rotating, it releases the chain with the weights. The weights have been changed with respect to the old weights in figure 2.2. The new weights are just

nuts tied to the chain by a wire of negligible mass. The nuts have an higher mass with respect to the old weights and are more fit for the level of thrust generated by the z-70.

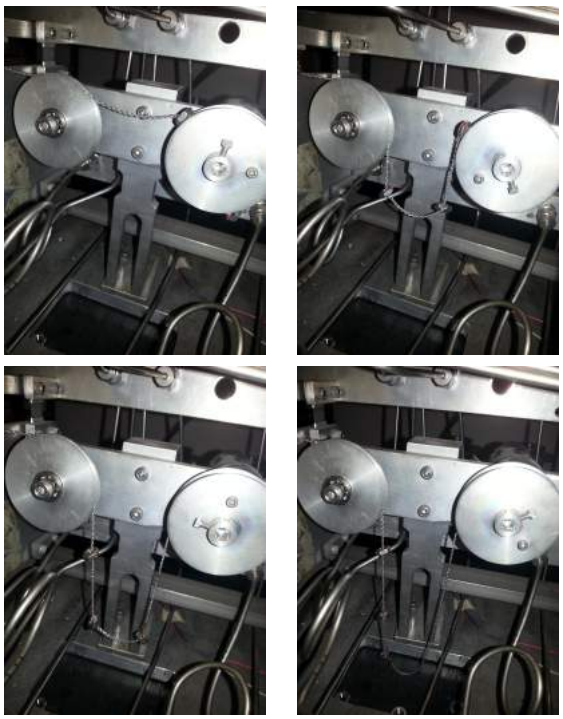

Figure 2.28: Calibration system

This calibration procedure leads to four calibration points, more than enough since the behavior of the thrust stand is linear, but still much less than the cup method.

The force transferred to the thrust stand is due to the mass of the chain and the mass of the weights.

The mass m_c of the chain was precisely measured, so the linear density ρ_c could be computed just by dividing the mass of the chain by its length L_c. The mass of the weights m_w is the same for each and every weight.

The mass of the chain released by the spool is computed by computing the length of chain released in the four cases and then multiplying the length by the linear density of the chain ρ_c.

The length of the chain released is computed by looking at the angle of rotation of the spool and then multiplying the angle (in radians) by the radius of the spool R_s.

$m_c[g]$	L_c $[in]$	$\rho_c[g/in]$	m_w $[g]$	R_s $[in]$
1.85	18.70	0.0989	1.20	0.885

Table 2.7: Calibration masses proprieties

To compute the angles of rotations in the three cases figure 2.29 was used. A picture of the spool was taken for each of the four points and then superimposed on a goniometer.

With these four angles it is possible to compute the mass of the chain.

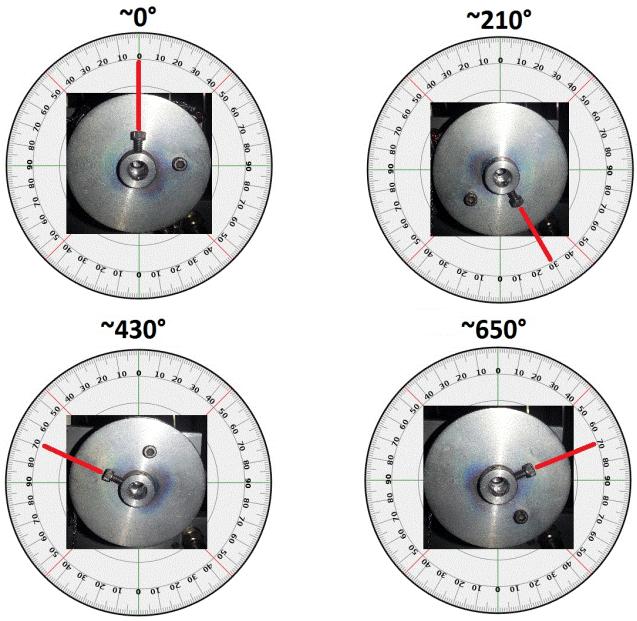

Figure 2.29: Angles of spool rotation

The mass of the chain that is effectively released on the thrust stand is half of the

mass of the chain released by the spool, since 50% of the mass is sustained by the spool itself, as it can be understood from figure 2.28.

The weights naturally weigh on the thrust stand (through the pulley) when they are on the left branch of the chain as seen in figure 2.28. In the first configuration no weight adds mass to the thrust stand, one weight in the second, two weights in the third, and all three weights in the fourth.

The total released mass m_{tot} for the four configurations is computed and shown in table 2.8. The calibration force F_{cal} is computed by simply multiplying the mass by 9.81 m/s^2.

#	m_w [g]	θ_c [ř]	m_c [g]	m_{tot} [g]	F_{cal} **[mN]**
0	0	0	0	0	**0**
1	1.2	210	0.1604	1.3604	**13.3455**
2	2.4	430	0.3284	2.7284	**26.7660**
3	3.6	650	0.4965	4.0965	**40.1865**

Table 2.8: Calibration force computation

The following calibration points in table 2.9 were taken outside the chamber at room temperature (70 degrees) and without the thruster mount. For each calibration force F_{cal} the current of calibration i_{cal} needed to stabilize the thrust stand was recorded. The value of i_{cal} was averaged over 2000 measurements.

F_{cal} [mN]	i_{cal} [A]
0	0.706
13.3455	1.124
26.7660	1.554
40.1865	1.990

Table 2.9: Calibration points

The linear fit is shown in figure 2.30, with the calibration points.

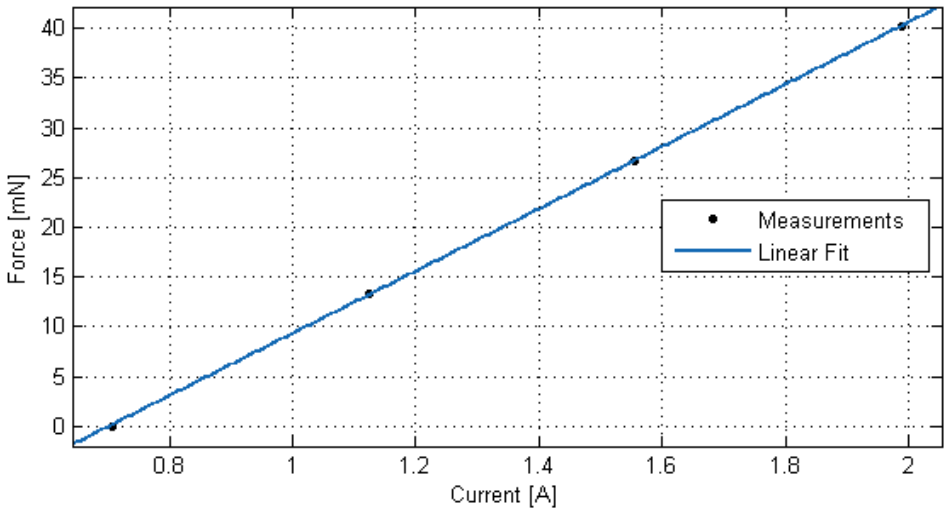

Figure 2.30: Calibration fit

As it can be seen the behavior is almost perfectly linear. For this calibration a change in 1 A of current corresponds to a force generated of 31.29 mN. This value is different with respect to the one computed with the cup method because it strongly depends on the equilibrium distance between the solenoid and the magnet and this distance changes at every testing. The difference between the two values is not related to the different ways the two calibrations are performed: every calibration leads to a slightly different gain of the instrument every time.

The goodness of the fit is summarized in table 2.10.

SSE	0.05816
RMSE	0.1705

Table 2.10: Goodness of linear fit

SSE is the residual sum of squared errors of prediction and RMSE is the root-mean-square error. Both values are very small, so the linear approximation is a good approximation.

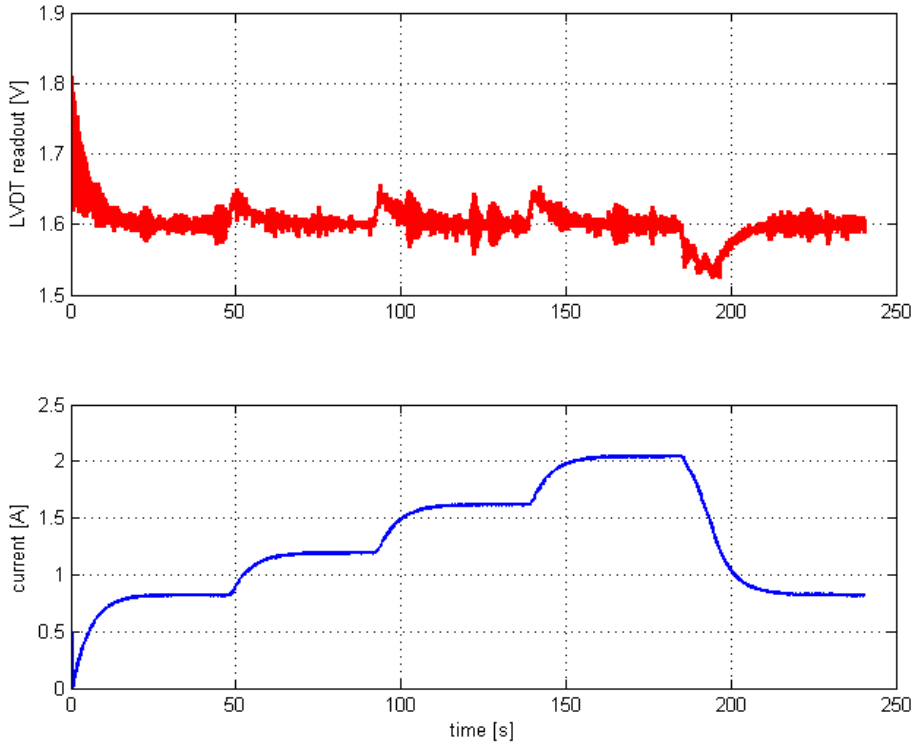

Figure 2.31: Calibration current and LVDT readout

Figure 2.31 shows the LVDT readout and the current against time during a calibration. In the first 20 seconds the thrust stand reaches the setpoint equilibrium condition. When each weight is released the current increases and the thrust stand takes few seconds to reach again the same equilibrium position. When all the weights are removed the thrust stand returns back to the original position and it is ready to precisely measure the thrust. The position of the thrust stand, after the first 20 seconds, remains more or less the same as it can be seen from the top in figure 2.31. When each weight is released there is a perturbation which is promptly compensated by the control system.

2.6.4 Comparison Between Real and FEMM Results

FEMM has been a very useful and important tool for this project because it drove the choice of the magnet material, its sizes, the number of coils of the solenoid, its diameter and the distance between the two.

From the previous sections it is possible to compare the predicted to the delivered results.

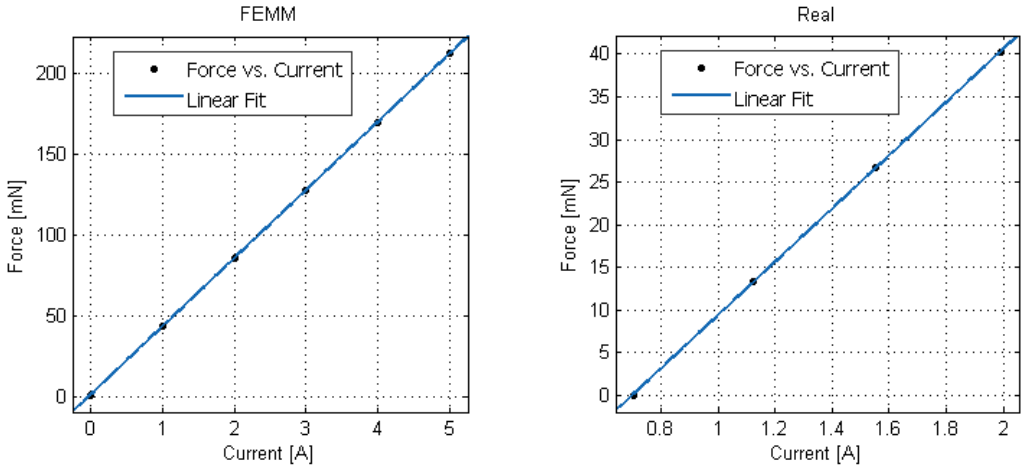

Figure 2.32: Comparison between real (right) and FEMM (left) results

The real calibration coefficient is compared with the simulated one using FEMM and dipole-dipole interaction.

Model	Calibration coefficient [mN/A]
Dipole-dipole	45.15
FEMM	42.21
Real	31.29

Table 2.11: Comparison between FEMM and real calibration

As expected the real system is less efficient than the simulations.

3 Testing

3.1 Large Vacuum Facility

3.1.1 Large Vacuum Chamber

The large vacuum chamber at Stanford University consists of a non-magnetic stainless steel tank approximately 1.5 m in diameter and 3.3 m in length. The tank is connected to a T section, where there are the cryogenic panels. A large 1.5 m gate valve can insulate the main tank from T section, so it is possible to make adjustments to the setup, without exposing the panels.

Figure 3.1: Large vacuum chamber

3.1.2 Roughing Pumps

The first stages of vacuum are represented by two mechanical pumps, informally called black pump and blower. The black pump is the roughest pump in the line and is the first one to be turned on after closing the vacuum chamber. It brings down the pressure in the chamber down to less than 10 Torr.

Below 10 Torr the blower, which is in series with the black pump, is turned on. The blower brings the pressure down to less than 50 mTorr.

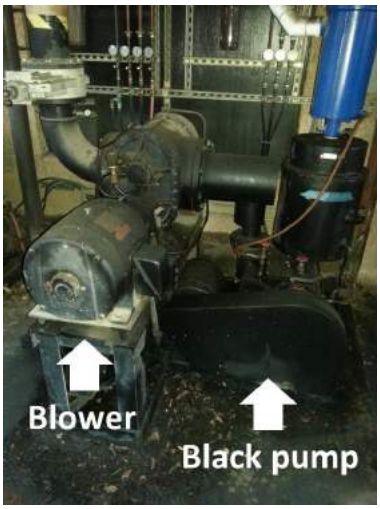

Figure 3.2: Roughing pumps

3.1.3 Turbomolecular Pump

The turbomolecular pump is a mechanical additional optional stage, which is not always used. When used, it speeds up the pumping process and it also can be used along with the cryopumps to help them dealing with xenon and argon when the thruster is running. This pump has to be backed by the blower and the black pump when it is working.

Figure 3.3: Turbomolecular pump

3.1.4 PolyCold and Cryopumps

After the rough vacuum is achieved using the roughing pumps and sometimes also the turbomolecular pump all the vacuum lines to the chamber are closed and the vacuum chamber is sealed.

The cryopumps are the main responsible for the extremely low pressure in the chamber. They are not real pumps, but rather very powerful chillers able to bring down the temperature of panels inside the chamber (figure 3.4 on the right) to 12K or lower. The molecules in the chamber get frozen as soon as they get in contact to the panels and become solid, thus giving no more contribution to the pressure. This is the working principle that allows the pressure inside the chamber to go down. The two cryopumps in the large vacuum facility in Stanford could not go down to lower than 17K at the time of the development of this thesis. In order for them to work they have to be backed by a commercial chiller called Polycold. The Polycold chiller brings down the temperature of the panels below the freezing point of water before the cryos are turned on, so decreasing the load of the cryopumps, which don't have to take care of the water vapor in the air. The Polycold unit is a less expensive alternative of using liquid nitrogen, which is much more effective and fast. During the experiments the temperature of the panels is monitored. The temperature tends to increase when the panels are close to saturation since too many frozen molecules on the panels reduce the efficiency of the system.

Figure 3.4: PolyCold (left) cryopump (center) panels (right)

3.1.5 Vacuum Performances

The pressure is monitored using a thermocouple gauge sensor and a hot-cathode ionization gauge. The thermocouple gauge sensor can measure pressures down to 30 mTorr. When the crypumps are on and the temperature drops down the pressure can be monitored using a hot-cathode ionization gauge.

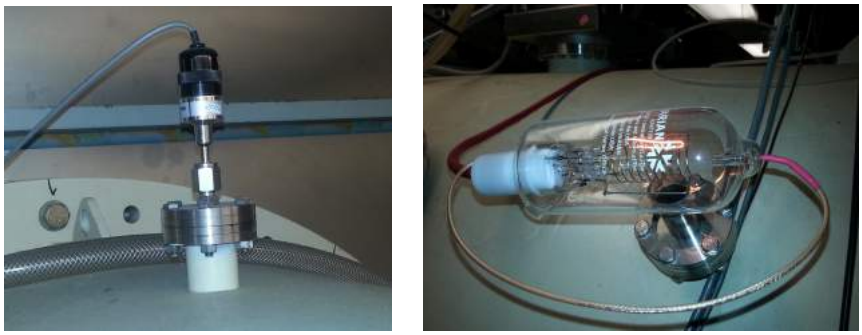

Figure 3.5: Thermocouple gauge sensor and hot-cathode ionization gauge

Table 3.1 shows the typical values in terms of pressure inside the chamber and temperature of the panels (left panels T_{left} and right panels T_{right}) during a test session. p_c is the minimum pressure (reached when the thruster is not working), while p is the pressure during typical thrust measurements. While the thruster is working the pressure increases due to the flows of argon and xenon, the temperature of the panels increases a little during the operation of the thruster.

p_c[torr]	p_c[Pa]	p[Pa]	T_{left} [K]	T_{right} [K]
$4{\cdot}3 \cdot 10^{-7}$	$5{\cdot}73 \cdot 10^{-5}$	$3 \cdot 10^{-4}$	19.1	23.9

Table 3.1: Vacuum performances

3.2 Laboratory Setup

3.2.1 Vacuum Connections

Figure 3.6 shows the anode connections to the thruster, inside the vacuum chamber. The outer and inner magnets are connected from the outside, because this particular

engine can also be operated connecting the two magnetic circuits to two different power supplies.

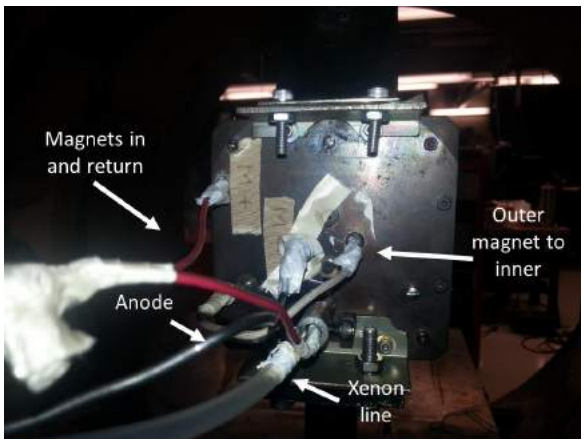

Figure 3.6: Z-70 Connection anode

The cathode connections consist of one electrical line for the heater, one for the keeper and one for connecting the cathode to the Hall thruster circuit as shown in figure 1.4 and also a gas connection. The cathode was operated on argon.

Figure 3.7: Cathode connections

3.2.2 Xenon and Argon Lines

The xenon and argon lines are shown in figure 3.8 (left). The xenon tank (blue one) and the argon tank (not shown in the picture) are connected to two of the three lines

in figure. The third line is used to bypass the argon control valve. The bypass is used to start the cathode. In Figure 3.8 (right) it is possible to see the mass flow controller, which enables the operator to choose the mass flow rate of argon and xenon.

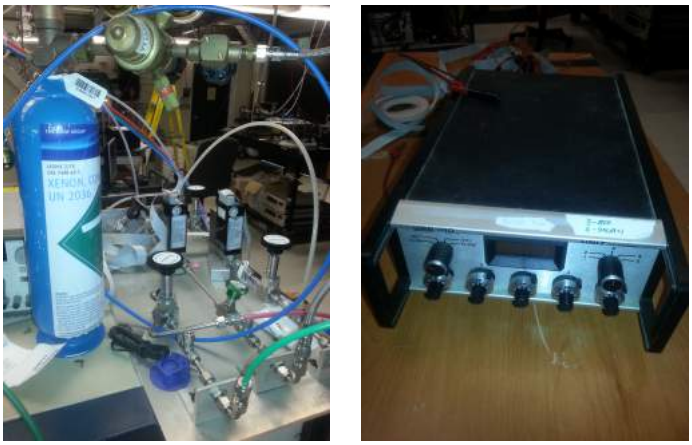

Figure 3.8: Xenon and argon assembly (left), mass flow controller (right)

The mass flow is set in sccm (standard cubic centimeter per minute).

3.3 Thrust Stand Operation

3.3.1 Raw Data

Figure 3.9 shows the data obtained during the first test.

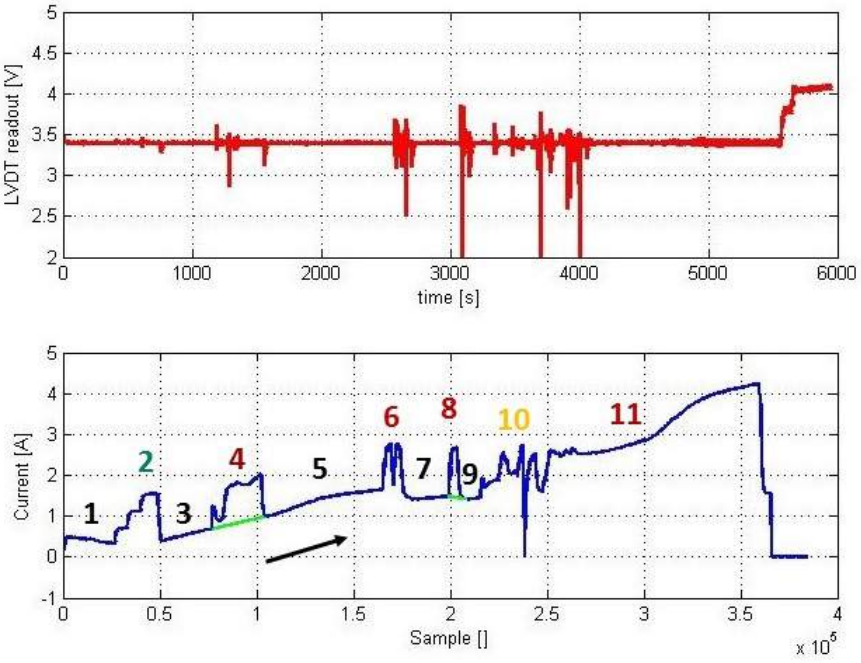

Figure 3.9: Raw data

The plot on the top in figure 3.9 shows the LVDT readout voltage, which is proportional to the displacement of the thrust stand. The plot on the bottom shows the current in the solenoid needed to control the position of the thrust stand. The x axes in the two plots are time and samples (constant sampling).

As it can be seen the thrust stand remains at a constant position throughout the experiment (LVDT readout 3.4 V), a part for oscillations due to noise and perturbations due to the thruster especially when the thruster is on and during calibration.

At the end of the experiment the current was so high due to drifts that the position was lowered to decrease the current needed and consequently the testing ended.

Numbers and colors in figure 3.9 help understanding what is going on. In points 1, 3, 5, 7 and 9 (color black) the thruster is off; in point 4,6,8 and 11 the thruster is on; point 2 is the calibration and finally in point 10 there were a lot of spankings going on in the engine (unstable behavior of the Hall thruster).

Figure 3.10 shows a typical current profile during thruster operation. The first hump is the glow mode, explained in the introduction of this thesis. During glow mode the magnets are off and the plasma is generated by the inefficient interaction between non magnetized electrons and neutrals. The engine is not working as an Hall thruster. After the magnets are turned on and the thruster goes into nominal mode the thrust increases significantly.

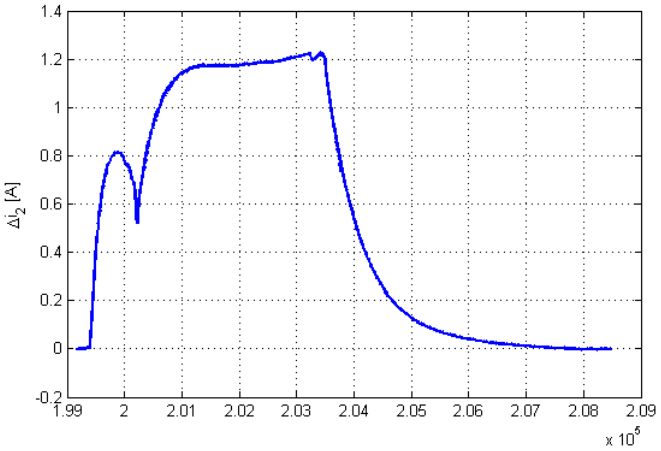

Figure 3.10: Thrust profile

A big positive drift makes it impossible to precisely compute the thrust from the raw data in figure 3.9.

3.3.2 Drifts

The drifts are due to two main reasons: stress relaxation and heating. Stress relaxation is an effect due to the fact that the stiffness of any elastic material tends to diminish if the material is subjected to a constant strain. Practically if one stretches

a spring, forcing it to remain in a certain position, the stiffness will be lower and lower in time. Since it is a relaxation it leads to a negative drift.

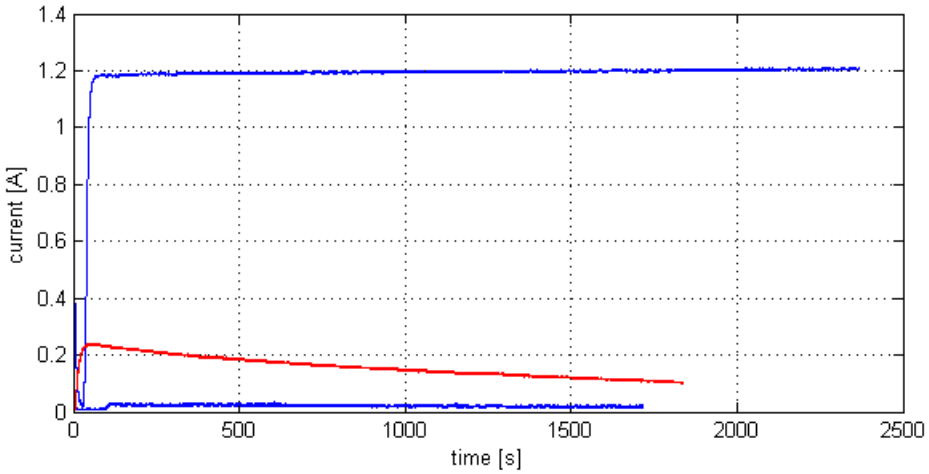

Figure 3.11: Stress relaxation drifts

Figure 3.11 shows a test that has been done in vacuum with the thruster off to measure the drifts due to stress relaxation. For the two blue curves (top and bottom) the initial current i_0 (control current for no thrust) is near zero. The curve in the bottom has no force applied, while a constant force of 40.19 mN is applied for the one on the top, this force is compensated by a current of around 1.2 A. For the red curve (middle) the initial current is around 0.25 A and no force is applied. As is can be seen, comparing the blue curves with the red one in the middle, if i_0 is near zero the drift is very little, while if it is not near zero there is a substantial negative drift. Table 3.2 summarizes the results of the drift experiment.

#	i_0 [A]	F [nN]	$Drift$ [A/hr]	$Drift$ [nN/hr]
1	0.03	0	-0.018	-0.58
2	0.25	0	-0.28	-9
3	1.19	40	+0.028	+0.9

Table 3.2: Stress relaxation drifts

In case number 3 in table 3.2, which corresponds to the curve on the top in figure 3.11, the drift is slightly positive due to the thermal effect which becomes dominant. In this case the heating more than compensates for the small relaxation.

Heating is due to two causes: heating due to the dissipation in the solenoid and due to the heat coming from the hot plasma and the thruster in general. Heating, in both cases, makes the solenoid less and less effective, meaning that an higher current is needed to generate the same force. This results in a positive current drift. One reason for the big heating drift in figure 3.9 can be understood by knowing the geometry the thrust stand. The LVDT, which measures the displacement, is on the other side with respect to the solenoid/magnet system. When the thrust stand heats up the whole structure expands due to thermal expansion.

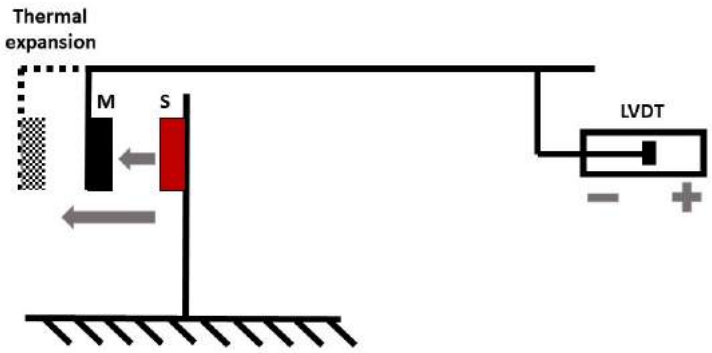

Figure 3.12: Thermal expansion effect

Figure 3.12 schematically shows the effect of thermal expansion. As the structure expands the LVDT readout voltage increases and the control system compensates by pushing the magnet in order to maintain the same LVDT readout output. Other than the current drift, this phenomenon is negative for another reason: since the magnet and the solenoid are now further apart the calibration is no longer valid because the interaction between the solenoid and the magnet is a function of the distance between the two. This distance, due to thermal expansion, is not only related to the output of the LVDT, but also to the temperature.

The drift due to heating is much harder to control and predict. A possible improvement would be to use a thermocouple to measure the temperature throughout the experiment. Once two or more calibrations are done for different values of temperature, it is possible to relate the calibration coefficient to the temperature. However, it is not trivial to put a thermocouple inside a vacuum chamber, and it was not possible to use one for this thesis.

Equation 2.16, which relates the displacement of the thrust stand to the current, leads to a linear relationship between temperature of the thrust stand and current only if the expansion is very small. Since the expansion coefficient α_T is very small, this approximation holds also for relative big changes in temperature. The static equation describing the behavior of the thrust stand is:

$$k\Delta L/2 = f(i,x) = \frac{3}{2}ar_0 i - 6ai_0\Delta L \tag{3.1}$$

i_0 is the equilibrium current (needed to keep the thrust stand in equilibrium before the thermal expansion), while i is the current needed to compensate for the thermal expansion.

It is important to note that the force generated by the solenoid, needed to compensate for the increase in temperature, is just half the force needed to move the thrust stand of the expansion length ΔL. The reason for that can be understood by looking at figure 3.12. The thrust stand expands evenly when heated, half on the left side (where there is the solenoid) and half on the right side (where there is the LVDT). Since the control system measures the displacement on the LVDT side, the solenoid has to push the magnet of only half the thermal expansion length in order to maintain the same LVDT readout voltage.

In order to relate the expansion x to the temperature, the linear expansion model can be assumed:

$$\Delta L = L_0\alpha_T\Delta T \tag{3.2}$$

Where L_0 is the initial length of the thrust stand, α_T is the coefficient of thermal

expansion and ΔT is the increase in temperature.

From equation 3.1:

$$\frac{3}{2}ar_0 i = \left(\frac{k}{2} + 6ai_0\right)\Delta L = \left(\frac{k}{2} + 6ai_0\right)L_0\alpha_T\Delta T \tag{3.3}$$

Which leads to a linear relation between current and increase in temperature .

$$i = \frac{\frac{k}{2} + 6ai_0}{\frac{3}{2}ar_0}L_0\alpha_T\Delta T \tag{3.4}$$

To prove this theory, which relates the current drift with thermal expansion, numbers were plugged in equation 3.4.

N []	$m_2[a \cdot m^2]$	$A_s[mm^2]$	$r_0[mm]$	k$[N/m]$	$L_0[m]$	ΔT [K]	i_{drift}[**A**]
20	0.740	198	14	100	0.80	100	**1.06**

Table 3.3: Current drift order of magnitude

An increase of 100K (order of magnitude of the increase in temperature) leads to a current of about 1 Amp, which is the order of magnitude of the current drift.

In theory it would be possible to use this model to compute the thrust under conditions different from the calibration condition by simply removing the excess force needed to compensate for the thermal expansion, but it wouldn't be a very precise measurement. A more precise data acquisition method, which relies on simple post processing, is required.

3.3.3 Data Acquisition and Reduction

The acquisition method used to obtain precise thrust measurements is similar to the one previously used in the old calibration method, but this time measuring the current instead of the LVDT output.

After the thruster is turned on and the mode of interest is reached, the thruster is left on for at least 20 minutes in order to let it reach the working temperature. Then

the control system is turned on. The moving part of the thrust stand is pushed to the equilibrium position (in terms of LVDT output voltage) according to the value selected by the operator. A pyramid is created by simply releasing and taking off the calibration weights. As soon as the calibration is done the thruster is immediately turned off. The current decreases and reaches the thruster-off condition. Then another calibration, with the thruster off, is performed. The calibration with the thruster on is the most important and determine the relationship between the current and the force and also the calibration drift. Plateaus of similarly loaded states, during the pyramid, are averaged and four values of current are obtained i_0, i_1, i_2, i_3. This four currents are compared in order to obtain the three values of current jumps (Δi_1, Δi_2, Δi_3) (double arrows in figure 3.13) needed to compensate for the calibration weights. Then the calibration drift is computed by making the weighted average of the three drifts of similarly loaded states, during the calibration. The average was weighted by the length of the plateaus, meaning that short plateaus (especially the single plateau relative to the third weight) influence less the drift. This drift, even if it is very small, has to be characterized in order to compute a precise value of the thrust. The current suddenly decreases as soon as the thruster is turned off. The whole system starts to cool down and the current starts to be affected by a big drift. The second pyramid, with the thruster off, is done to characterize this drift and compensate for the few seconds necessary for the system to go back to equilibrium position. The value of current at the instant the thruster is turned off (green dot on the right of figure 3.13) is computed by removing this drift. Then the calibration drift is removed and the final value of current (green dot on the left) is now placed in the middle of the pyramid. In this way the final value of current accounts for the two drifts: during the calibration and after the thruster is turned off. The pyramid after the thruster is turned off is not always done since the drift can be estimated even without the second pyramid.

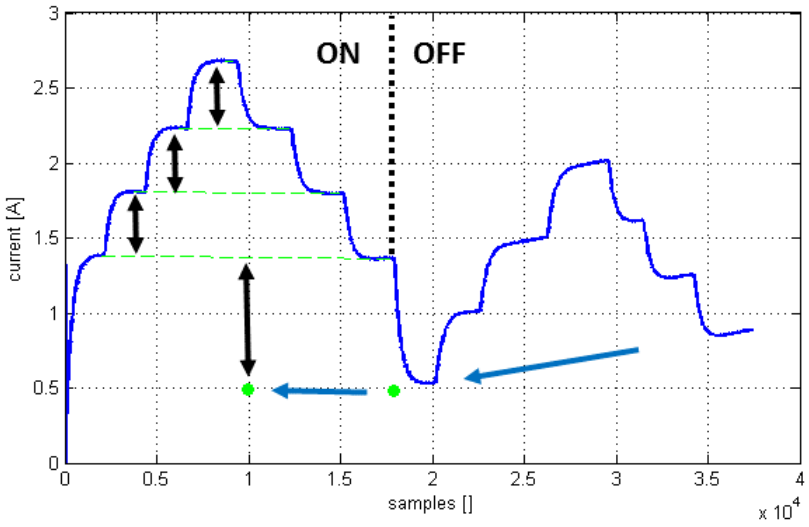

Figure 3.13: Data acquisition

This final value of current i_{off} is then compared with i_0 in order to have a precise estimation of the current jump due to the thrust. The difference of the two value Δi_{thrust} is multiplied by the calibration coefficient and the thrust T is obtained.

3.4 Performance Parameters

3.4.1 Thrust

In an Hall thruster the thrust is obtained through the acceleration and expulsion of stored propellant. For any kind of engine the thrust can be computed using the thrust equation:

$$T = \dot{m}_p u_e + (p_e - p_0)A_e \tag{3.5}$$

$\dot{m}_p$ is the mass flow rate of propellant, u_e is the average exit velocity of propellant (velocity of expulsion), p_e is the external pressure, p_0 is the internal pressure and A_e is the exit area of the thruster. In Hall thrusters (and ion thrusters as well) the

pressure inside the engine is approximately null since vacuum is necessary for the production of plasma inside the thruster chamber. The external pressure is approximately null too since Hall thrusters are made to work only in space. A finite little back pressure increases the performances of an Hall thruster [7], but it is just an artificial expedient, since it is not a realistic scenario in space. This explains why it is so crucial that the engine is tested in a high quality vacuum environment. For an Hall thruster the external area plays no role in the generation of thrust and the equation simplifies:

$$T = \dot{m}_p u_e \tag{3.6}$$

The thrust T is the one that will be measured with the thrust stand, $\dot{m}_p$ is the total mass flow as sum of the mass flows of xenon (anode) and argon (cathode) and u_e is the average exit velocity of the flow (not only ions).

The thrust equation holds for any kind of engine, however the physical mechanism for which momentum is exchanged changes completely between engines. For both ion and Hall thrusters the acceleration is obtained thanks to a static electric field, but the momentum exchange mechanism is different between the two [7]. In ion thrusters the momentum transfer is due to charged ions moving inside an electric field [7]. The ions modify the electric field they move in so that the net force on the grid, which is the thrust, is equal and opposite to the force the grid exerts on the ions [7]. In Hall thrusters the situation is more complicated since there is also a magnetic field which is responsible for the ExB current $\mathbf{J_{Hall}}$ (or Hall current). As explained before, while the ions are essentially unmagnetized, the electrons are subjected to the magnetic force $\mathbf{B}$. In fact the coupling between electric and magnetic field prevents electrons from going towards the anode. This effect is called Hall force and is responsible for the Hall current. This Hall force, according to Newton's third law, must be equal and opposite for electrons and magnets, meaning that the electrons trapped in this Hall current must exert on the magnets a force which is equal and opposite.

$$\mathbf{T} = \mathbf{J_{Hall}} \times \mathbf{B} = -\mathbf{F_i} \tag{3.7}$$

This is the mechanism for which momentum is transferred between plasma and the thruster body [7]. For this reason the Hall thruster is sometimes called an electromagnetic thruster [7] since both electric and magnetic field play a role in the generation of thrust, but it generates confusion since there are no electromagnetic waves involved. In an electrostatic thruster the ions are accelerated thanks to a potential difference V_b (beam voltage). In Hall thrusters this potential difference has to be smaller than the anode potential V_d (discharge voltage) set by the power supply, because of the voltage needed for ionization and losses. Figure 3.14 and 3.15 show the plasma potential and velocity profile inside the Z-70 as predicted by the simulation. The majority of the ions are accelerated near the end of the annular chamber.

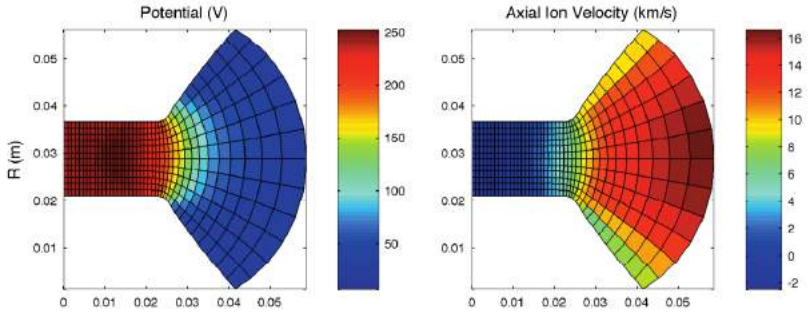

Figure 3.14: Plasma potential and ion velocity [5]

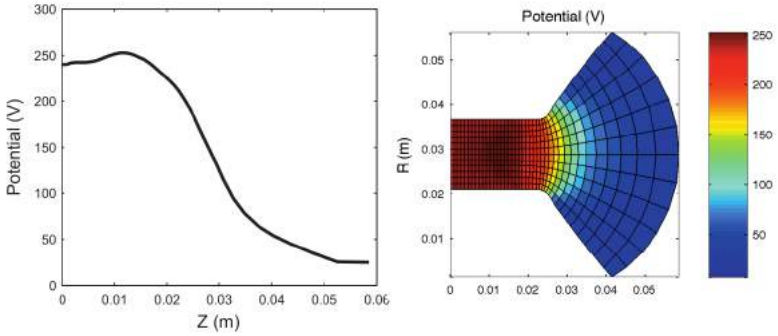

Figure 3.15: Plasma potential and ion velocity profile [5]

The theoretical framework in this chapter assumes that all the ions are singly-ionized, unless otherwise stated. The effect of doubly-ionized ions will be explained in chapter 4 where the species fraction of doubly-ionized ions will be measured using an ExB probe.

For the conservation of energy the kinetic energy of the ions must be equal to the energy provided by the electric field during the acceleration:

$$\frac{1}{2} m_I u_e^2 = q V_b \tag{3.8}$$

Which means that the velocity of the ions can be written as:

$$u_e = \sqrt{\frac{2qV_b}{m_I}} \tag{3.9}$$

The mass flow rate can be simply expressed as:

$$\dot{m}_p = \frac{I_b m_i}{q} \tag{3.10}$$

Substituting equation 3.10 and equation 3.9 in equation 3.6 :

$$T = \sqrt{\frac{2m_I}{q}} I_b \sqrt{V_b} \tag{3.11}$$

Where q, is equal to the charge of the electron $e = 1.60217662 \cdot 10^{-19} C$, and m_I is equal to the mass of the xenon atom which is $m_I = 2.18017 \cdot 10^{-25} kg$. The ratio $\sqrt{\frac{2m_I}{q}}$ is a constant, so the thrust can be computed by knowing the beam current I_b and voltage V_b.

This equation must take into account a correction factor γ .

$$T = \gamma \sqrt{\frac{2m_I}{q}} I_b \sqrt{V_b} \tag{3.12}$$

This correction factor γ can be written as the product between a correction factor α which takes into account the plasma composition and a correction factor F_t that takes into account the divergence angle of the beam [7].

$$\gamma = \alpha F_t \tag{3.13}$$

In the simple approximation of constant ion current density profile $J(r)$ and uniform electric field, the correction coefficient can be simple expressed as $F_t = \cos\theta$ [7], where θ is the average half-divergence angle (around 20 degrees), otherwise:

$$F_t = \frac{\int_0^r 2\pi J(r)\cos\theta(r)\,dr}{I_b} \tag{3.14}$$

The correction coefficient α, which takes into account the contribution of singly and doubly-ionized ions will be discussed in detail in chapter 4, along with the other effects of the multiply-charged ions.

3.4.2 Specific Impulse

By precisely knowing the thrust and the mass flow rate it is possible to compute the average exit velocity, which is related to the specific impulse, in fact:

$$I_{sp} = \frac{T}{\dot{m}_p g_0} = \frac{u_e}{g_0} \tag{3.15}$$

where g_0 (approximated as 9.81 m/s/s in this thesis) is a constant that simply scales the efficiency and it is not related to the real local value of the gravitational acceleration.

The change in mass of the spacecraft translates into a change in velocity the direction of which is opposite to the direction of propellant expulsion [18]. This change of velocity is called deltav and can be computed using the well-known Tsiolkovsky equation:

$$\Delta v = I_{sp} g_0 \log\left(\frac{m_0}{m_f}\right) = u_e \log\left(\frac{m_0}{m_0 - m_p}\right) \tag{3.16}$$

Where m_0 is the initial mass and m_f is the final mass which is equal to the initial mass minus the mass of propellant m_p . While this equation is not important in the

developing of the project it shows the importance of having high specific impulse, in fact it allows to have less propellant to obtain the same change in velocity deltav. The average exit velocity u_e equals the average ion velocity only if all the xenon molecules are ionized. In reality it is possible to define a mass utilization efficiency which takes into account the non-ionized xenon particles. The mass utilization efficiency η_m is defined as the ratio between the mass flow of charged ions and unionized propellant, which is:

$$\eta_m = \frac{\dot{m}_I}{\dot{m}_p} = \frac{I_b}{e}\frac{m_I}{\dot{m}} \tag{3.17}$$

3.4.3 Mass Flow Rates

The mass of the propellant for an Hall thruster is the sum of the mass flow of the cathode and the anode. The Z-70 is operated on xenon (anode) and argon (cathode).

$$\dot{m}_p = \dot{m}_a + \dot{m}_c \tag{3.18}$$

The mass flow controllers are able to control the flow of xenon and argon through the anode and cathode respectively. The value is set in sccm (standard cubic centimeters per minute), which is the flow of gas in cubic centimeters at standard pressure (1 atm) and temperature (273.15 K) per minute. In order to convert from sccm to mg/s, one must use the following equation [7]:

$$1\,sccm = 7.43583 \times 10^4 M_m [mg/s] \tag{3.19}$$

Where M_m is the molecular mass of either xenon or argon. In the two cases the equation becomes:

$$1\,sccm_{Xe} = 0.0983009 [mg/s] \tag{3.20}$$

$$1\,sccm_{Ar} = 0.0297046 [mg/s] \tag{3.21}$$

3.4.4 Total Efficiency

The total efficiency η_t is defined as the ratio between the jet power P_{jet} and the total power P_{tot}.

$$\eta_t = \frac{P_{jet}}{P_{tot}} \tag{3.22}$$

The kinetic power of the jet (or jet power) is defined as:

$$P_{jet} = \frac{1}{2}\dot{m}_p u_e^2 \tag{3.23}$$

Using equation 3.6 to compute the exit velocity as a function of thrust and substituting it into the definition of jet power:

$$P_{jet} = \frac{T^2}{2\dot{m}_p} \tag{3.24}$$

The total power is The sum of all the input powers:

$$P_{tot} = P_d + P_k + P_{mag} \tag{3.25}$$

Where P_d is the discharge power, P_k is the cathode keeper power (zero for space qualified thrusters, negligible for the Z-70) and P_{mag} is the power to generate the magnetic field. In theory, to compute the efficiency of the Z-70, one should also consider the heater power, since the cathode of the Z-70 is not able to work in self-heating mode. This power, however non-negligible, will not be taken into account for this study because it depends only on the cathode and not the engine itself and would be an unfair source of inefficiency since space qualified cathodes work in self heating mode.

The total efficiency becomes:

$$\eta_t = \frac{T^2}{2\left(\dot{m}_a + \dot{m}_c\right) P_{tot}} \tag{3.26}$$

This equation shows that whenever the thrust increases, thanks to any expedients

other than increasing the mass flow rate, the total efficiency increases [7]. For space qualified Hall thrusters this value can be as high as 60% as shown in table 1.1.

3.4.5 Anode Efficiency

The anode efficiency η_a describes the efficiency of the thruster considering only the effect of the anode. It can be computed by using the following equation:

$$\eta_a = \frac{T^2}{2\dot{m}_a V_d I_d} \tag{3.27}$$

The anode efficiency and the total efficiency can be related by defining the cathode efficiency and the electrical utilization efficiency[7].

The cathode efficiency is defined as:

$$\eta_c = \frac{\dot{m}_a}{\dot{m}_a + \dot{m}_c} \tag{3.28}$$

The electrical utilization efficiency is defined as:

$$\eta_o = \frac{P_d}{\dot{m}_a + \dot{m}_c} \tag{3.29}$$

The relation between anode and total efficiency is:

$$\eta_a = \frac{\eta_t}{\eta_o \eta_c} > \eta_t \tag{3.30}$$

Moreover the anode efficiency η_a can be decomposed as the product of multiple efficiencies:

$$\eta_a = \frac{T^2}{2\dot{m}_p P_d} = \eta_v \eta_b \eta_m \tag{3.31}$$

Where η_v is the voltage utilization efficiency, η_b is beam utilization efficiency and η_m is the mass utilization efficiency. The effect of multiply-charged ions on the anode efficiency will be discussed in chapter 4.

3.5 Z-70 Delivered Performances

3.5.1 Data

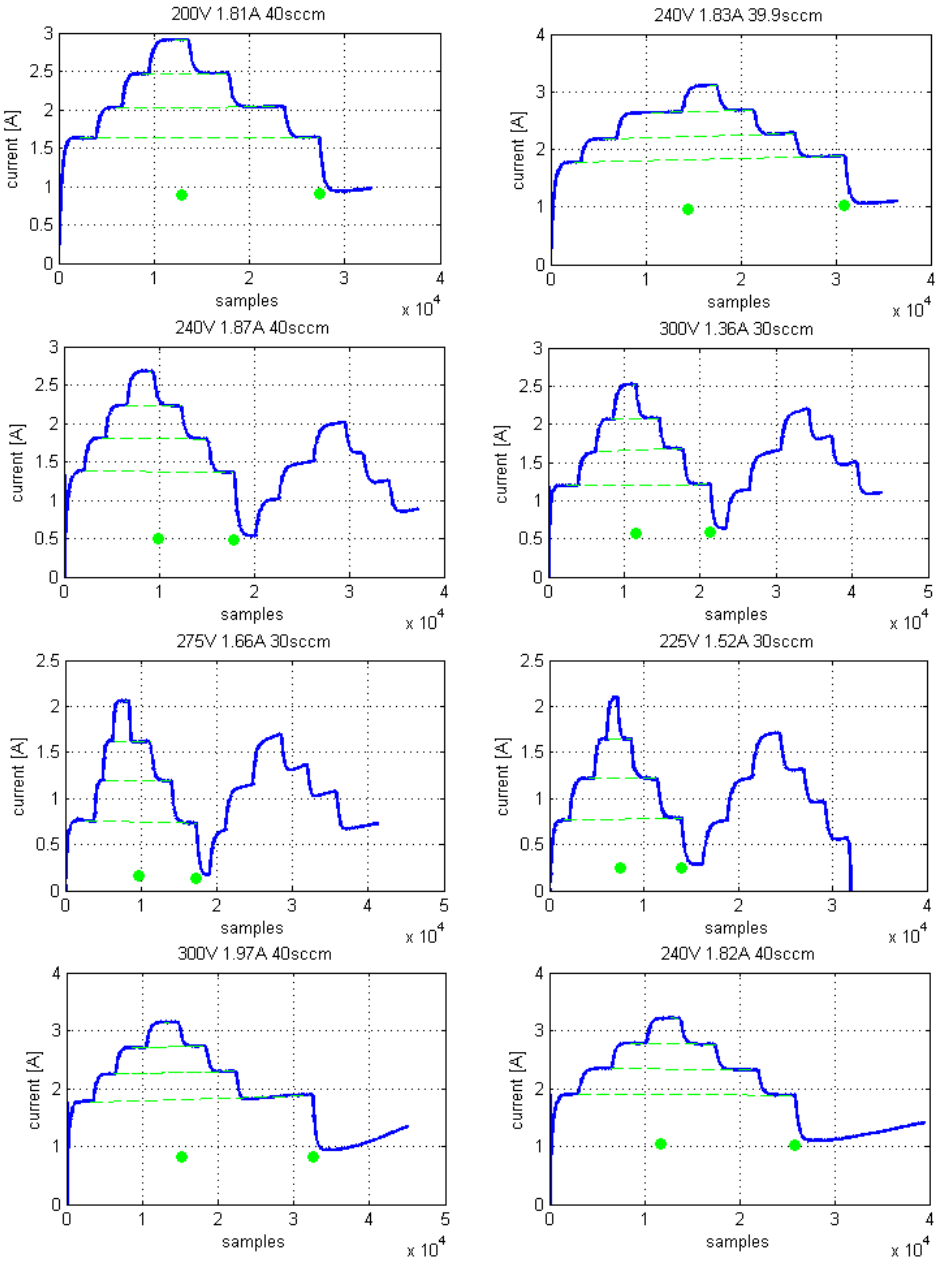

Figure 3.16: Data six working points

Figure 3.16 shows the data acquisition procedure for eight different working points.

3.5.2 Results

Table 3.4 shows the results computed for eight working points.

$V_D[V]$	$I_D[A]$	$P_D[W]$	$I_m[A]$	$\dot{m}_{Xe}[sccm]$	**T[mN]**	$u[m/s]$	$I_{sp}[s]$	$\eta_a[\%]$
200	1.81	362.0	1.620	20	**23.414**	11,073	1,129	38.52
225	1.52	342.0	0.790	15	**17.185**	10,588	1,079	29.28
240	1.82	436.8	1.700	20	**27.643**	13,073	1,333	44.49
240	1.83	439.2	1.899	20	**27.926**	13,238	1,349	45.27
240	1.87	448.8	1.901	20	**28.485**	13,471	1,373	45.98
275	1.66	456.5	0.790	15	**19.301**	11,892	1,212	27.67
300	1.36	408.0	1.310	15	**20.669**	12,735	1,298	35.51
300	1.97	591	1.700	20	**32.795**	15,509	1,581	46.28

Table 3.4: Results

The average velocity of ions, the specific impulse and the anode efficiency are computed using the experimentally measured values.

The main input parameters are the discharge voltage, the mass flow rate and the magnetic current. These values are set by the operator. The main outputs are the discharge current (which sets the power) and, of course, the performance values. The operator has to change one of the three parameters in order to change the discharge current, and so the power.

The most important point, which is the one that will be compared with LIF measurements and the simulations, is the point at 240V discharge voltage and 1.82A discharge current. This point is the closest one to where LIF measurements were done.

3.5.3 Comparison between Different Working Conditions

The equations presented before for computing the performance parameters are relatively simple, but all the parameters are strongly intertwined. A part from few

general considerations, the change of one parameter can have an effect which could be different from what would be expected. For example an increase in mass flow rate, according to equation 3.27, seems to lead to a decrease in anode efficiency, but in reality it leads to an increase in thrust, which makes the anode efficiency rise. In general the situation is even more complex.

The average ion velocity tends to increase for increasing discharge voltages. In fact the discharge voltage increases the beam voltage, so the ions have an higher potential difference to exploit to accelerate. The higher ion velocity leads to an higher specific impulse. The increase in discharge voltage does not necessarily mean an increased anode efficiency.

The magnetic current increases the magnetic field. The stronger magnetic field traps an higher number of electrons, thus increasing the ionization efficiency[7]. This results in an increased in anode efficiency and specific impulse. An high magnetic field tends to decrease the discharge current since less electrons manage to reach the anode. If the magnetic field increases to much the engine shuts off. Sometimes even a small increase in magnetic current is enough to shut the engine off.

An increase in mass flow of xenon tends to have a positive effect on the performances. An higher flow naturally increases the thrust. As explained before, since the efficiency equation varies with the square of the thrust, this leads to an increased anode efficiency. Moreover the increase in the mass flow rate leads to an higher number of charges in the annular chamber which increases the discharge current.

Table 3.5 is just a guideline which is in agreement with the experimental results and can be justified by the theoretical framework. These considerations do not hold in the general case, since, as explained before, all the parameters are linked together and are strongly dependent on the physics of the engine which is very complex and nonlinear.

Input parameter	Direct effect	Secondary effect
Discharge voltage	Increases ion velocity	Increases specific impulse
Mass flow rate	Increases discharge current and thrust	increases anode efficiency
Magnetic current	Increases ionization efficiency	Increases average velocity and anode efficiency; decreases discharge current and power

Table 3.5: Inputs influence

3.5.4 Delivered Total Efficiency

The total efficiency can be computed by computing the cathode efficiency and the electrical utilization efficiency. Table 3.6 shows the magnets power P_m and the electrical utilization efficiency for the eight working points.

$V_D[V]$	$I_D[A]$	$P_D[W]$	$I_m[A]$	$P_m[W]$	$\eta_o[\%]$
200	1.81	362.0	1.620	7.87	**97.87**
225	1.52	342.0	0.790	1.87	**99.46**
240	1.82	436.8	1.700	8.67	**98.05**
240	1.83	439.2	1.899	10.8	**97.60**
240	1.87	448.8	1.901	10.8	**97.64**
275	1.66	456.5	0.790	1.87	**99.59**
300	1.36	408.0	1.310	5.15	**98.75**
300	1.97	591	1.700	8.67	**98.55**

Table 3.6: Electrical utilization efficiency

The electrical utilization efficiency is very high for the working points with low magnetic current. For these points the anode efficiency is low, but the anode efficiency doesn't take into account the power needed to generate the magnetic field.

Table 3.7 shows the cathode efficiency η_c for the two different mass flows of xenon: 20 sccm and 15 sccm. The mass flow of argon is the same for every point equal to

5 sccm.

$\dot{m}_{Xe}[sccm]$	$\dot{m}_{Ar}[sccm]$	$\dot{m}_{Xe}[mg/s]$	$\dot{m}_{Ar}[mg/s]$	$\dot{m}_{tot}[sccm]$	$\eta_c[\%]$
15	5	1.4745	0.14852	20	**90.85**
20	5	1.9660	0.14852	15	**92.98**

Table 3.7: Cathode efficiency

Table 3.8 shows the total efficiency along with the cathode and the electrical utilization efficiencies for the working points.

$V_D[V]$	$I_D[A]$	$I_m[A]$	$\dot{m}_p[mg/s]$	T[mN]	$\eta_o[\%]$	$\eta_c[\%]$	$\eta_a[\%]$	$\eta_t[\%]$
200	1.81	1.620	2.114	23.414	97.87	92.98	38.52	**35.05**
225	1.52	0.790	1.623	17.185	99.46	90.85	29.28	**26.46**
240	1.82	1.700	2.114	27.643	98.05	92.98	44.49	**40.56**
240	1.83	1.899	2.114	27.926	97.60	92.98	45.27	**41.07**
240	1.87	1.901	2.114	28.485	97.64	92.98	45.98	**41.74**
275	1.66	0.790	1.623	19.301	99.59	90.85	27.67	**25.04**
300	1.36	1.310	1.623	20.669	98.75	90.85	35.51	**31.85**
300	1.97	1.700	2.114	32.795	98.55	92.98	46.28	**42.41**

Table 3.8: Total efficiency

3.5.5 Comparison between SPT Family

The results obtained in terms of specific impulse, total efficiency power and thrust for the Z-70 are compared with the SPT family in figure 3.17 [7, 14, 20, 16]. The performance parameters are reported as a function of the external diameter of the annular chamber. In particular the four SPT thrusters are: SPT 50, SPT 70, SPT 100 and SPT 140, with a diameter of 50, 70, 100 and 140 millimeters respectively. The Z-70 has a diameter of 72 mm, so it compares with the SPT-70. It's important to note that the results reported for the SPT family are the average performances in nominal conditions, while for the Z-70 the reported results are the ones achieved at the maximum power and maximum efficiency (table 3.4).

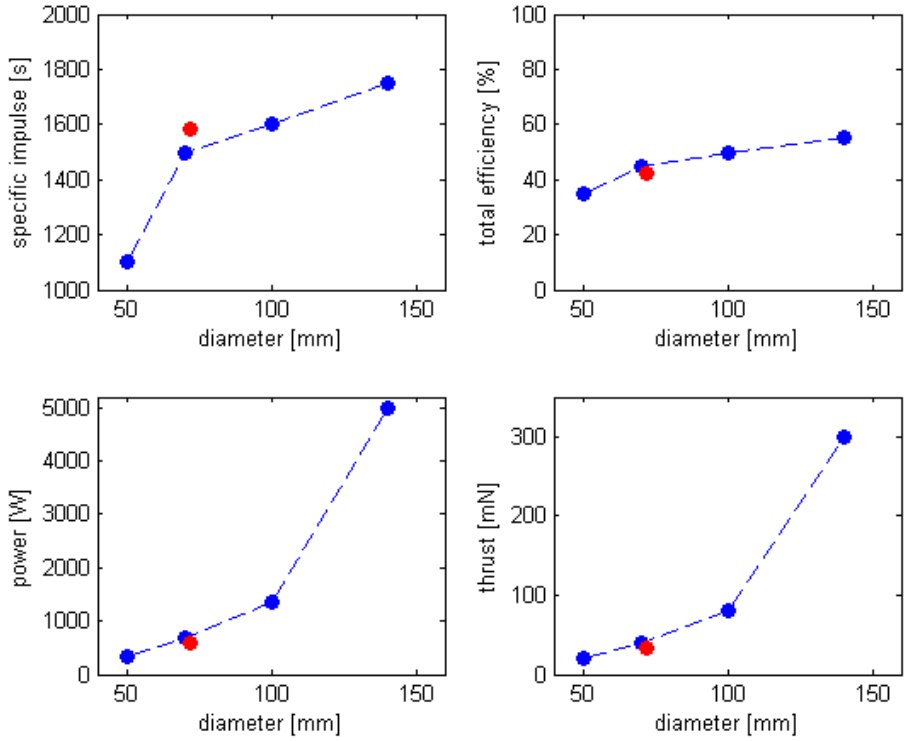

Figure 3.17: Z-70 vs SPT family

The blue dots are the SPT thrusters, while the red dot is the Z-70. The specific impulse and the total efficiency measured are comparable to the space qualified thrusters.

3.5.6 Numerical Simulations

The numerical simulations are useful to understand the physics governing the cross-field region, the plasma fluctuations and to predict the overall performances. The simulation is a 2-D hybrid simulation, where the solution is computed in the radial-axial plane. It is called hybrid because it treats electrons as a fluid while neutrals and ions are treated as discrete particles [3]. The main challenge of any Hall thruster simulation is to try to simulate the electron mobility along the electric field. The

model for the Z-70, developed at Stanford university, takes into account the turbulent nature of electrons in an Hall thruster by exploiting a zero-equation model [19]. This model describes the electron viscosity and dissipation using simple algebraic equations without solving any differential equation.

The geometry of the Z-70, used in the simulation, along with the peak magnetic field B near the channel exit and the other input values are reported in table 3.9.

D_e [cm]	D_i [cm]	L [cm]	B [G]	V_d [V]	$\dot{m}_p$ [kg/s]
7.2	4.2	2.3	160	240	2

Table 3.9: Z-70 simulation parameter

Where D_e and D_i are the outer and inner diameter, L is the channel length, V_d is the discharge voltage and $\dot{m}_p$ is the mass flow of propellant.

The results of the simulations in terms of average discharge current I_d and frequency of breathing oscillation f_b are reported in table 3.10.

I_d [A]	f_b [kHz]
1.7	~23

Table 3.10: Simulated ion current and breathing frequency

The discharge current as a function of time and its FFT are shown in figure 3.18.

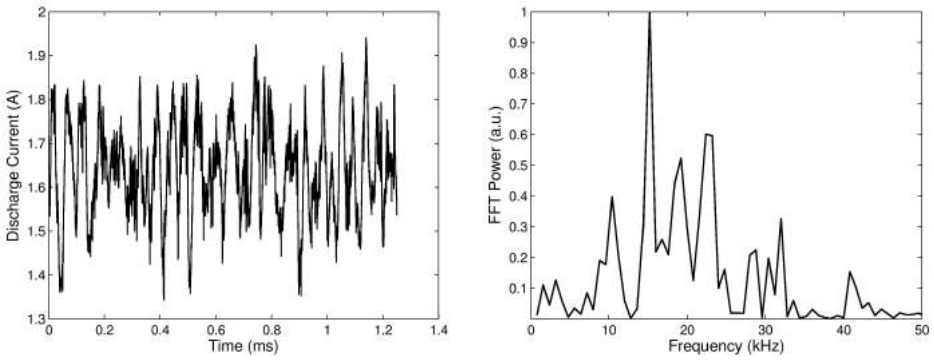

Figure 3.18: Discharge current vs time (left) FFT (right)

The current as a function of time was computed for just 1.3 milliseconds, because the simulation is very slow, this results in a non very reliable FFT of the signal. Nevertheless the FFT shows a peak at 23 kHz which is in agreement with the measurements, while the peak at 16 kHz has no real physical meaning.

Figure 3.19 shows the real measurements of discharge current. The breathing mode is clearly evident at the breathing frequency of around 23 kHz.

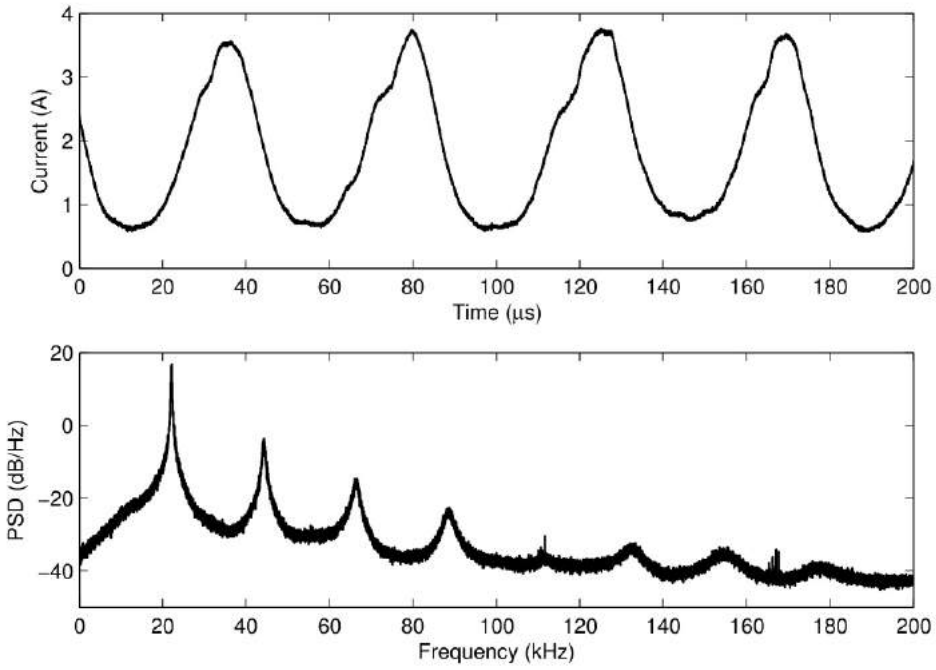

Figure 3.19: Discharge current measurements

The real measurement is much smoother than the simulated one and shows multiple peaks.

Figure 3.20 and 3.21 show the full results of the simulations in terms of plasma potential, axial ion velocity, plasma density, electron temperature, axial neutral velocity and neutral density.

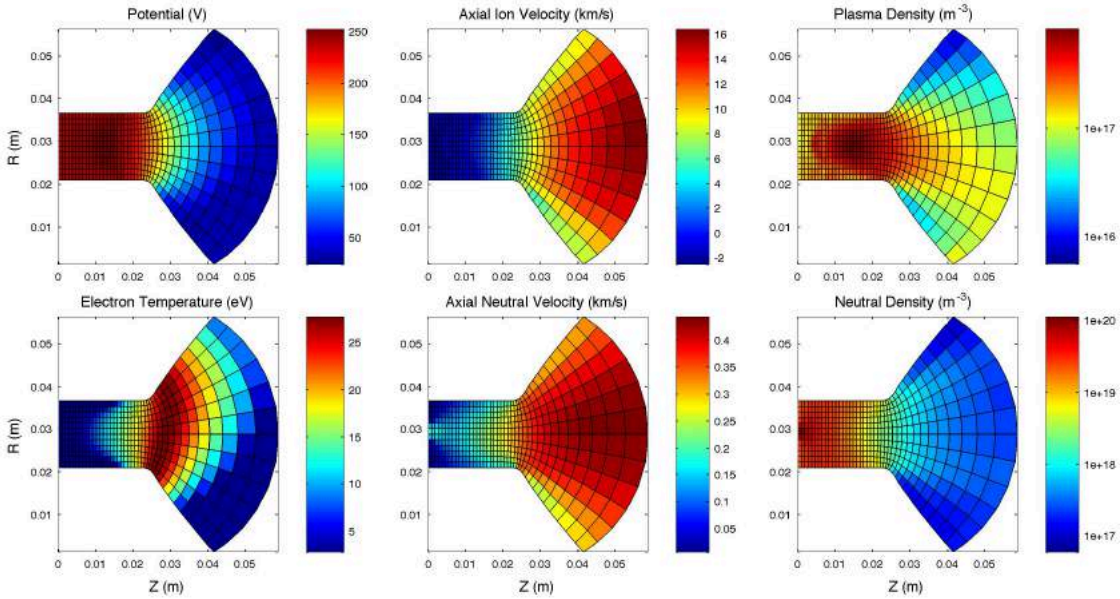

Figure 3.20: Simulation results, 2D map

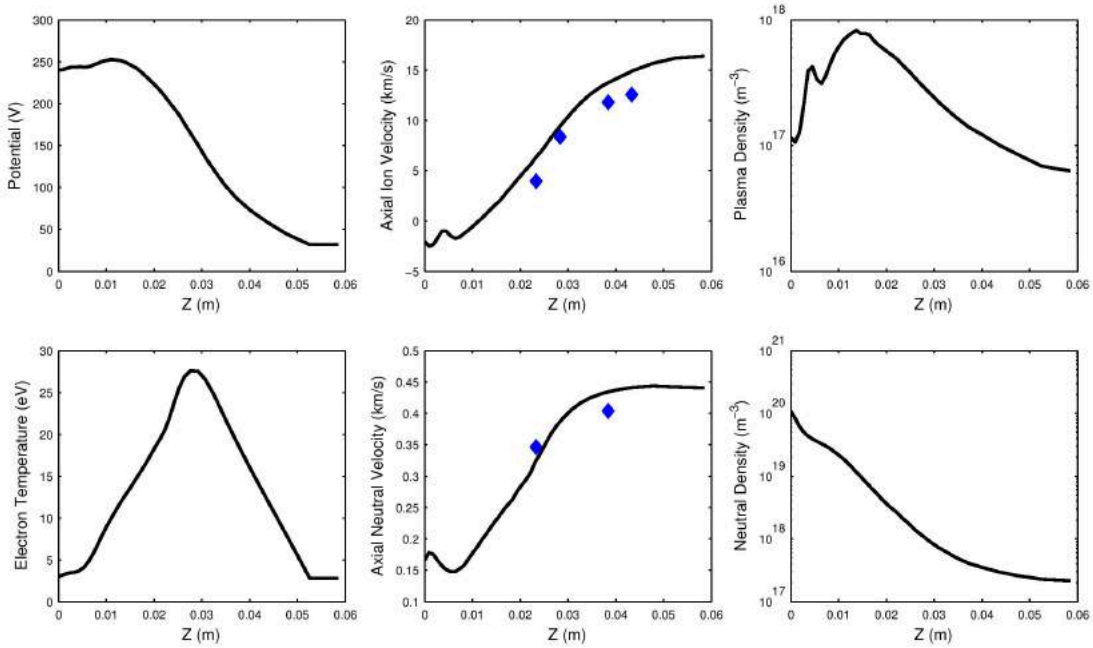

Figure 3.21: Simulation results, 1D average values

The blue dots in figure 3.21 are the values measured with LIF. The model matches reasonably well the measurements.

The integrated results in terms of specific impulse, thrust and anode efficiency, computed from the simulations are reported in table 3.11.

$I_{sp}[s]$	$T[mN]$	$\eta_a[\%]$
1369	26.8	45.6

Table 3.11: Z-70 simulated performances

The average velocity from the simulation is 13.430 km/s.

3.5.7 Comparison between Measurements and Simulation

The performance parameters are compared in table 3.22.

	$V_D[V]$	$I_D[A]$	$P[W]$	$I_{sp}[s]$	$T[mN]$	$\eta_a[\%]$
Simulation	240	1.7	408	1,333	26.8	44.49
Measurements	240	1.82	437	1,369	27.6	45.6

Figure 3.22: Comparison between measurements and simulation

The results of the simulations are very close to the measured values.

3.5.8 Laser Induced Fluorescence

The main reference for the LIF measurements is the paper published in 2015 by Chris Young and Andrea Lucca Fabris [1]. The details of the setup can be found in Chris Young's PhD thesis that will be published later this year. LIF is non-intrusive spectroscopic technique with which it is possible to measure the velocity of the ions in the plasma using laser technology. The velocity of the ions can be determined from the Doppler shift of the excitation fluorescence spectrum when compared with a stationary spectrum. In particular, thanks to the continuous wave laser-induced fluorescence sample-hold technique analysis done by Chris Young

and Andrea Lucca Fabris on the Z-70 it is possible to measure the velocity of the ions in a time-resolved and space-resolve fashion. Time-resolved analysis allows to know the ion velocity in a particular point of the breathing mode period, while space-resolved analysis allows the characterization of the ionization front inside the annular chamber. Figure 3.23 shows the ion velocity during the breathing period.

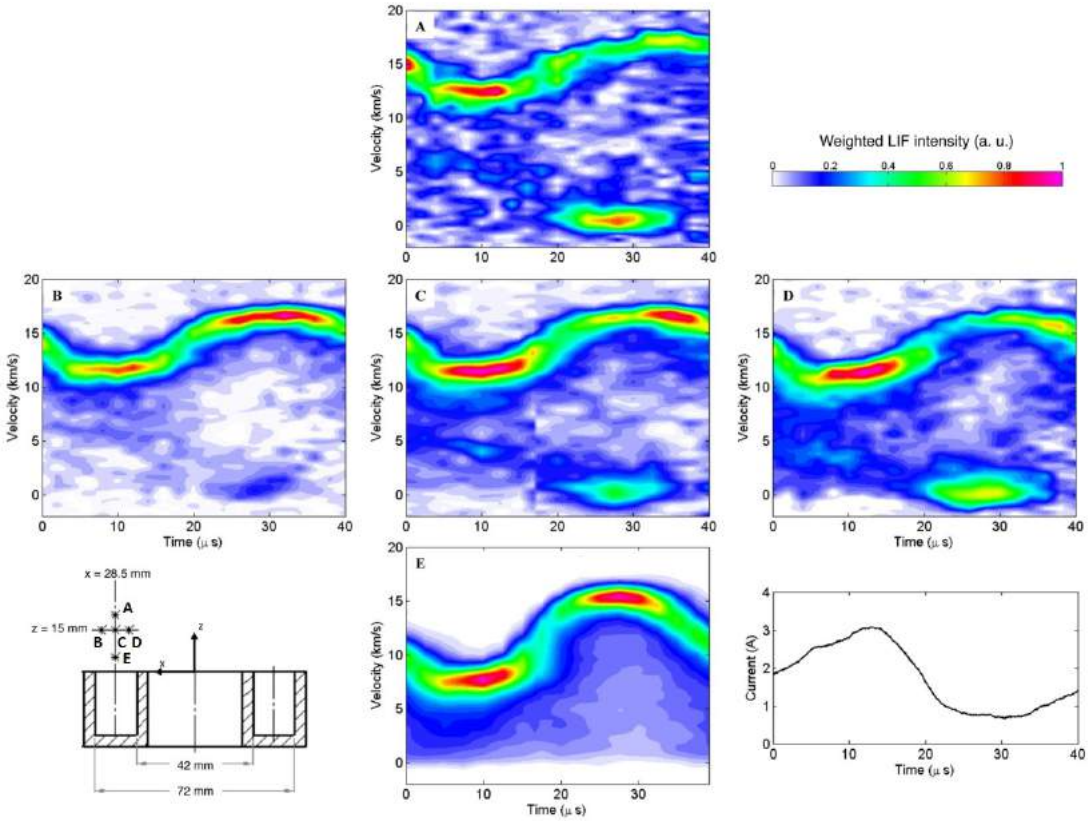

Figure 3.23: LIF time-resolved measurements

The four velocity maps are relative to the four points, right outside the annular chamber, A, B, C, D that can be seen in the scheme in the bottom left. The breathing mode period can be seen in the plot in the bottom right. Point A (map on the top) is the one more downstream where most of the acceleration has already taken place. In that regard it is interesting to see the difference in the velocity map between point E (closest to the exit section) and the others, most of the acceleration happens between

point E and C (B and D are aligned with point C). The highest ion velocity is when the current is the lowest in the breathing periods. When the discharge current is high the ionization is better and the population of low velocity ions (clearly evident in points A, C and D) almost disappears.

The average velocity measured by LIF is approximately 13.3 km/s

4 Ion Velocity Measurement

4.1 ExB Probe

4.1.1 Working Principle

The ExB probe (usually called Wien filter or velocity selector) is a sensor that can be used as a velocity filter for charged particles[6]. It consists of a box where inside there is a magnetic and electric field perpendicular one another. The ions enter a small aperture in the box and find themselves immersed in both fields. The electric force F_E is opposite to the magnetic force F_B. When $F_E = F_B$ the ions go straight and hit a sensor, which is made of a material able to emit electrons when hit by ions. This signal is measured and recorded. The magnetic field is constant and generated by permanent magnets, while the electric field is controlled and generated by a capacitor, connected to a power supply.

Figure 4.1 shows the working principle.

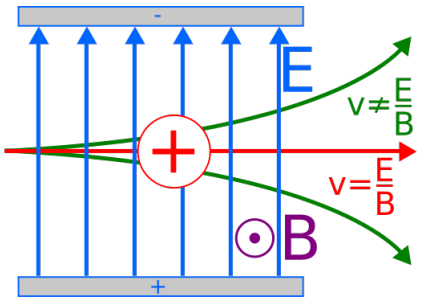

Figure 4.1: ExB sensor working principle

The ExB sensor used in this thesis project was developed in Stanford University as a copy of the ExB sensor of Michigan State University, the copy was made by past students, but the device had never worked properly.

When electric and magnetic field are balanced, the Lorentz force equals the electrostatic force:

$$q\,v \times B = q\,E \tag{4.1}$$

Since the electric and magnetic field are perpendicular, the scalar version of equation becomes:

$$vB = E \tag{4.2}$$

The velocity is simply:

$$v = \frac{E}{B} \tag{4.3}$$

Using the rough approximation that the electric field is linear, the following equation holds:

$$E = \frac{\Delta V}{d} \tag{4.4}$$

Where ΔV is the difference in potential between the two plates and d is the distance between the two plates. With this approximation the velocity is:

$$v = \frac{\Delta V}{Ed} \tag{4.5}$$

This is a rough approximation since it doesn't take into account the real geometry of the capacitor and fringe effects.

The ExB sensor used in this thesis is made of an iron box, with two big ferromagnetic magnets and two aluminum plates for the capacitor inside. The ions have to pass through a small aperture in order to enter a metallic tube which leads to the inside of the box where they find themselves immersed in the magnetic and electric field. The ions that go straight enter another small aperture and hit a piece of tungsten, which act as a Faraday cup (figure 4.2).

Figure 4.2: Tungsten sensor

The Faraday cup touches an aluminum screw which is connected to a BNC cable. The signal is read by a picoammeter, which is an instrument able to measure very small current signals. The picoammeter is connected to a computer which shows and records the signal.

4.1.2 Modifications

The sensor had major flaws and some modifications were made.

First, one of the two magnets was not in the right position since the iron box is a bit bigger than it should be. Aluminum sheets were added to "push" the magnet in position. It is worth noting that, since the magnets are very big and strong, separating them from the iron walls and adding aluminum sheets in between was not an easy task.

Figure 4.3 shows the inside of the ExB sensor. Over the magnet on the top, aluminum sheets keep the magnet in the metallic guides at a fixed distance between the lateral iron walls (removed in the picture).

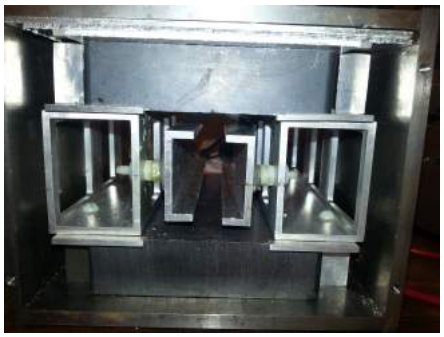

Figure 4.3: ExB sensor inside

Secondly, the people who made the instrument, in order to avoid fringe effects, made aluminum tubes that penetrated inside the magnetic and electric field. The big problem with this design choice is the fact that the aluminum tubes shield the electric field but not the magnetic field, so the ions were deflected inside the tube and were becoming neutrals after hitting the tube's walls. This is a critical design flaw and the tubes were cut off. Figure 4.5 shows the inside without tubes. Aluminum plates with a hole were put instead of the tubes to ensure that only horizontal ions hit the sensor. Figure 4.4 shows the magnetic field generated by the magnets and the interaction between the magnet and the aluminum tube inside. As it can be seen the magnetic field lines are not influenced by the aluminum tube, this was also assessed by using the Gaussmeter inside the tube.

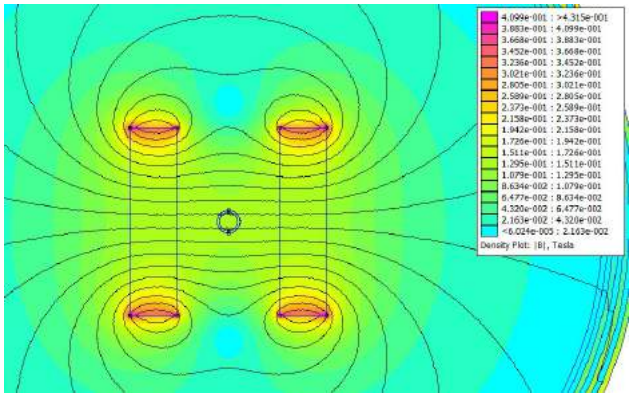

Figure 4.4: Magnetic field on FEMM

Figure 4.5: ExB sensor without tubes

The third modification consisted in connecting properly the tungsten sensor to the BNC cable which connects the tungsten sensor to the picoammeter. Figure 4.6 shows the new connection.

Figure 4.6: BNC Connection to the tungsten sensor

4.1.3 Electrical Connections

Figure 4.7 shows the connection for the ExB.

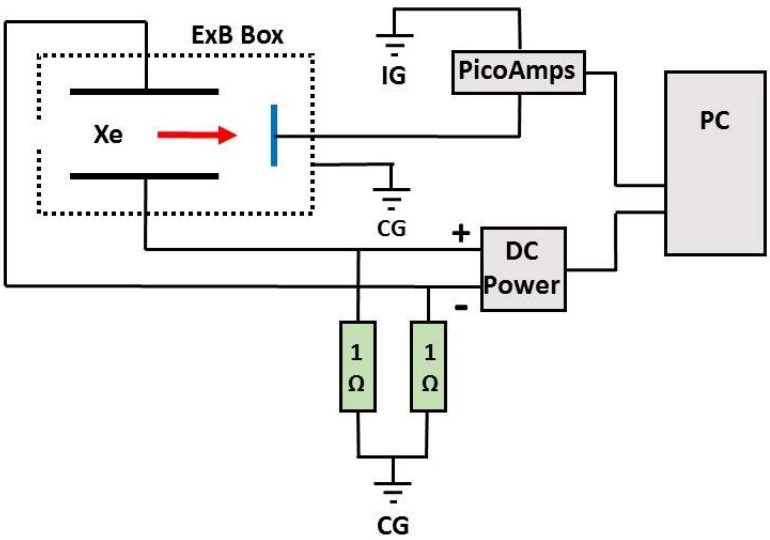

Figure 4.7: ExB full connection

The ions enter the box and are subjected by the two magnetic and electric forces. The ions that go straight hit the sensor and a small quantity of electrons start to flow in the signal line. The signal is read by the picoammeter. The picoammeter is connected to an insulated ground IG (not the chamber ground which is very noisy due to the plasma) to reduce the sources of noise. The picoammeter is connected though a GPBI cable to the computer, which is able to record the signal. The power supply provides a difference in voltage between the capacitor plates. The two outputs of the power supply are also connected to chamber ground CG through two $1\,M\Omega$ resistors. This is a critical connection, the ExB sensor was tested without the grounded power supply and didn't work properly. This trick allows the potential of the two plates to float around the ground chamber. The power supply is connected to the computer through a USB cable. The computer sends digital commands to the power supply and scans the voltages for the ExB.

Figure 4.8 shows the schematic of the circuit connecting the power supply to the sensor and the ground.

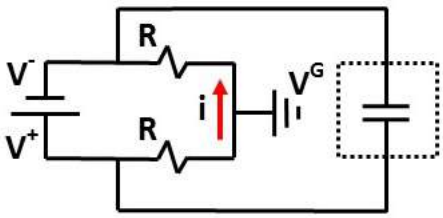

Figure 4.8: Power supply connection

The potential differences between the two resistors are:

$$\frac{V^{+}-V^{G}}{R}=i \tag{4.6}$$

$$\frac{V^{G}-V^{-}}{R}=i \tag{4.7}$$

The current i must be the same flowing in either resistor:

$$\frac{V^+ - V^G}{R} = \frac{V^G - V^-}{R} \tag{4.8}$$

Thanks to the fact that the resistors are the same, it is possible to write the following relation:

$$\frac{V^+ + V^-}{2} = V^G \tag{4.9}$$

The ground potential is always the average between the two outputs of the power supply, in this way the potential difference floats around ground potential.

4.1.4 Labview Logic

The Labview block diagram, made by the author of the thesis, can be found in the appendix. The block diagram is made of a big while loop with a flat sequence structure inside divided into three sections. In the first section the software sets the voltage of the power supply. In the second section it reads the voltage (not quite equal to the set value) and at the same time it reads the picoammeter signal 10 times and makes the average. In the third section the software saves the average value of the signal and the voltage in a text file. In the fourth section there is the increment in voltage (0.2 V) for the next cycle and the exit condition of the while loop.

4.1.5 Magnetic and Electric Field Assessment

The magnetic field was measured using a Gaussmeter as shown in figure 4.9.

Figure 4.9: Gaussmeter

The value measured in the middle is 1333 G which is equal to 0.1333 T.

The electric field was simulated using FEMM. Figure 4.10 shows the electric field for a potential difference of 78 V.

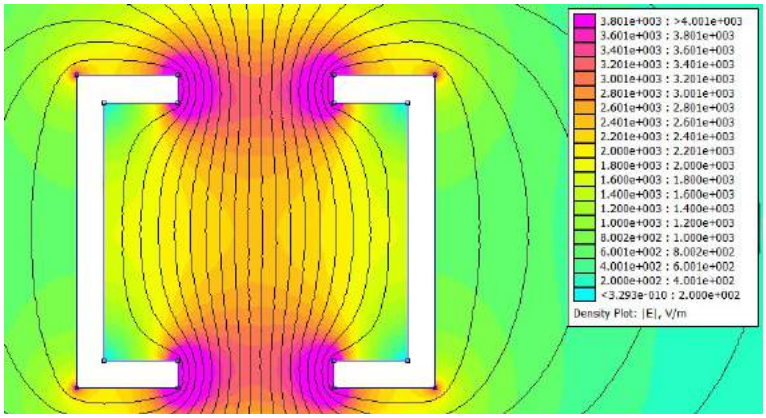

Figure 4.10: Electric Field on FEMM

The two plates of the capacitor were made with a C section because it makes the electric field more uniform in the middle.

Figure 4.11 shows the electric field in the middle of the capacitor as a function of the potential difference.

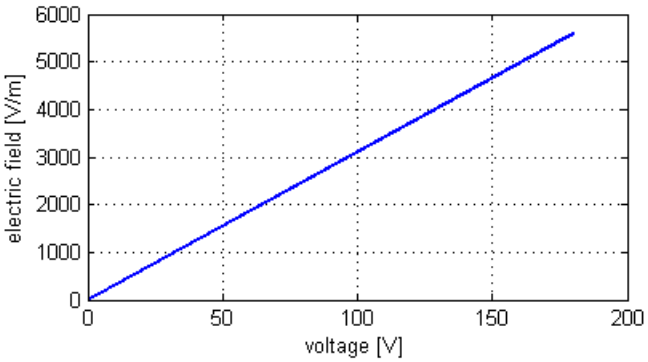

Figure 4.11: Electric field vs voltage

The electric field varies linearly with the applied voltage, approximately 311V/m increment each 1 Volt.

4.2 Testing

4.2.1 Effect of Multiply-Charged Ions

The effect of multiply-charged ions is perfectly described in Hofer's PhD thesis [11], which was the main reference for this chapter along with other Hofer's papers [2, 22].

If the beam contains multiply-charged ions the beam current can be written as:

$$I_b = I^+ + I^{++} + I^{+++} \dots \tag{4.10}$$

The total thrust can be computed with equation 3.11, substituting the new expression of the beam current (limiting it to just singly and doubly-charged ions):

$$T = I^+ \sqrt{\frac{2m_I V_b}{q}} + I^{++} \sqrt{\frac{2m_I V_b}{2q}} = I^+ \sqrt{\frac{2m_I V_b}{q}} \left(1 + \frac{1}{\sqrt{2}} \frac{I^{++}}{I^+}\right) \tag{4.11}$$

The thrust correction factor α, introduced in chapter 3, can be computed as the ratio between the thrust computed considering doubly-charged ions (equation 4.11) and the thrust computed with only singly-charged ions (equation 3.11):

$$\alpha = \frac{I^{+} + \frac{1}{\sqrt{2}} I^{++}}{I^{+} + I^{++}} = \frac{1 + \frac{1}{\sqrt{2}} \frac{I^{++}}{I^{+}}}{1 + \frac{I^{++}}{I^{+}}} \leq 1 \tag{4.12}$$

The correction factor α shows how doubly-ionized ions, even if they are faster than the singly-ionized ions, have a negative effect on the performance of an Hall thruster, since $\alpha \leq 1$[15]. If all the ions were doubly-ionized the thrust would be 30% less than if all the ions were singly-charged.

4.2.2 Vacuum Chamber Setup

Figure 4.1 shows the vacuum chamber setup for the ExB measurements. The thruster is on the thrust stand, so it was possible to measure the thrust along with the ExB signal. A steel structure lifts the sensor so it is aligned as well as possible to plume. The precise alignment was ensured by using a laser.

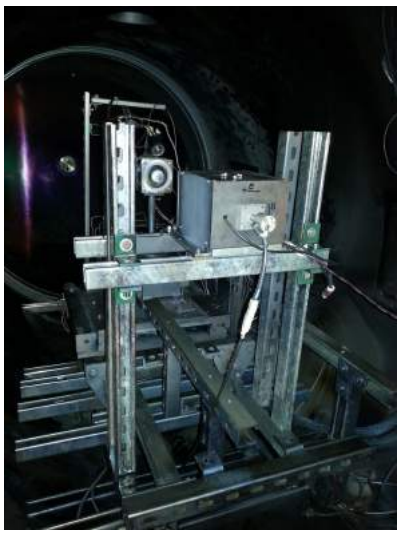

Table 4.1: ExB Setup

Figure 4.12 shows the alignment. The ions exit the thruster and a very little quantity enters the ExB box through the small aperture on the right of the figure.

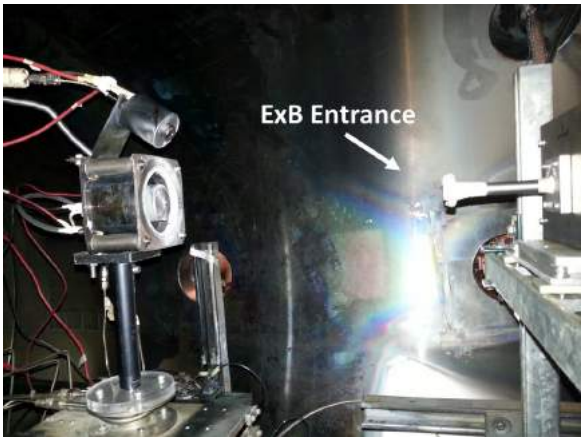

Figure 4.12: Z-70 ExB alignment

4.2.3 ExB Spectra

The ExB signal was recorded for the two most important working points in table 3.4: the LIF point and the maximum power point. The ExB signals are reported in figure 4.13.

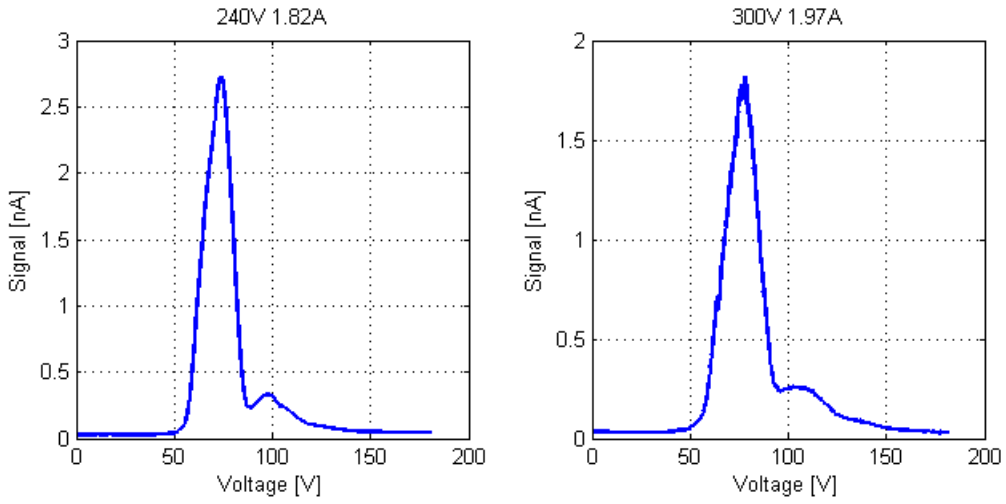

Figure 4.13: ExB spectra 240V (left) 300V (right)

The horizontal axis is the voltage difference between the capacitor plates set by the power supply, the vertical axis is the current collected by the Faraday cup and read

by the picoammeter. The highest peak is due to the singly-charged ions, the second peak is due to doubly-charged ions. At low and very high voltages the ion beam is deflected and almost no ion reaches the detector.

Figure 4.14 shows the signals in logarithmic scale. The logarithmic scale makes it easier to see the second peak. It is even possible to detect a hint of third peak in the 300 V spectrum.

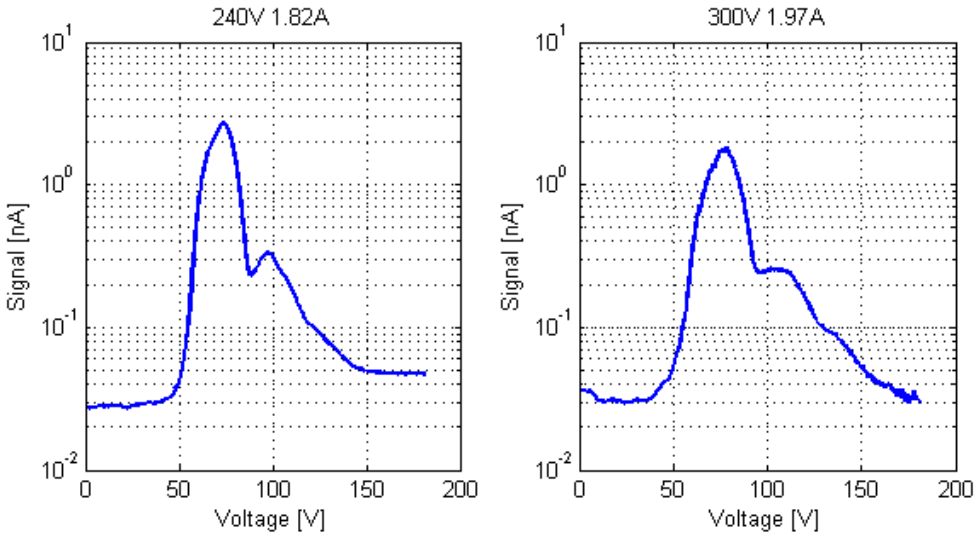

Figure 4.14: ExB logarithmic spectra 240V (left) 300V (right)

The normalized signals are reported in figure 4.15.

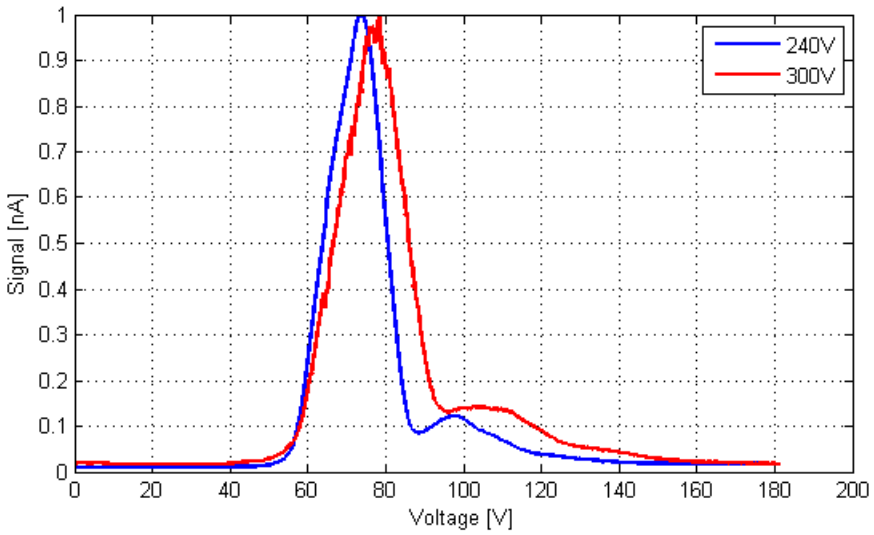

Figure 4.15: ExB normalized signals, comparison between 240V and 300V

The higher discharge voltage leads to faster ions, so it requires an higher voltage difference to detect the signal. The higher discharge voltage leads to a relative higher second peak, which means higher percentage of doubly-charged ions as it will be discussed later.

4.2.4 Collected Current

The current collected by the Faraday cup is the sum of the contributions of the single ion species. The current collected by the cup, for a single species i, is:

$$I_i = q_i \cdot A \cdot n_i \cdot u_i \tag{4.13}$$

Where A is the area of the detector as seen by the incoming ions (same for every species), n_i is the density of the species i, u_i is the velocity of the species i and q_i is the charge of the species i. Since the ExB sensor is a velocity selector, only ions with a certain velocity can hit the sensor, this allows computing some interesting plasma proprieties such as the species fractions and current fractions. However each species has a distribution of velocities (not all the singly-charged ions have

the same velocity), for this reason current contributions might overlap. In order to compute the currents, normal (Gaussian) were used to fit the signal as well as possible. The normal distribution is described by the following equation:

$$f(A,u,\sigma) = Ae^{-\frac{(x-v)^2}{2\sigma^2}} \tag{4.14}$$

Where A is the amplitude of the peak, v is the voltage relative to the peak (highest population for the species i), σ is the variance. Whenever A is high there is a high population of ions with that velocity. Whenever σ is high it means that the velocities are spread over a wide range.

Figure 4.16 shows the Gasussian interpolation lines.

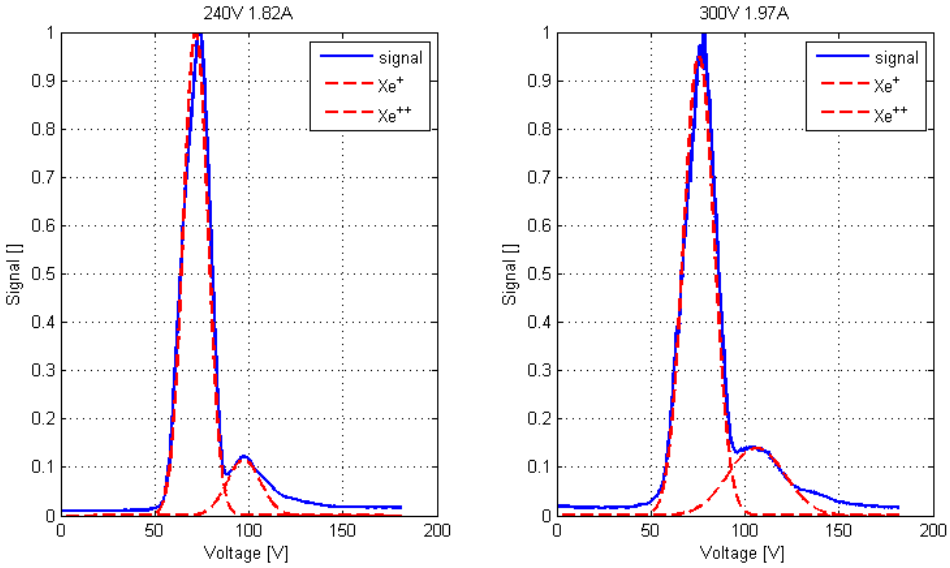

Figure 4.16: Gasussian interpolants

The parameters for the two Gaussians were optimized by a Matlab script written by the author to minimize the root of the sum of the squares of the errors between measured signal and sum of the two Gaussians. Table 4.2 reports the optimized parameters.

240V	v	A	σ	300V	v	A	σ
Gaussian Xe^{+}	71.7	0.998	6.4	Gaussian Xe^{+}	75.5	0.95	8
Gaussian Xe^{++}	97.3	0.115	8.9	Gaussian Xe^{++}	106.0	0.14	15

Table 4.2: Parameters of the Gaussians

As it can be seen, the variances of the doubly-charged ions are higher than for the singly-charged ions, this is due to the fact that the doubly-charged ions are produced out of the annular chamber and on a wider region (with a wider range of acceleration potential values), as it will be show later.

The current for each species is proportional to the area of the Gaussian, which can be computed as:

$$I_i \propto A_{g_i} = A_i \sigma_i \sqrt{2\pi} \tag{4.15}$$

It's worth noting that this is just a model. There is no theoretical framework that justifies a Gaussian distribution of velocities. In fact, the shape of the peaks doesn't quite match the shape of the Gaussian interpolants. The Gaussians were used to compute the plasma composition because they allow to take into account different values of variance for different species. The ion velocity and the energy of the species were computed just be looking at the measured peaks, without considering the Gaussian.

4.2.5 Ion Velocity

The ion velocity, which is equal to the ratio between the electric and magnetic field (according to equation 4.3), can be related to the voltage difference thanks to the simulation of the electric field. Figure 4.17 shows the signal as a function of ion velocity.

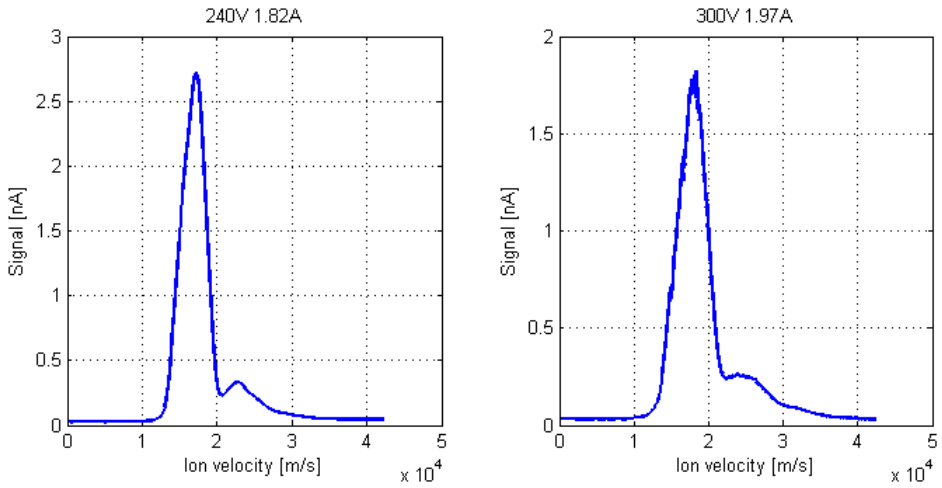

Figure 4.17: ExB Ion velocity

Table 4.3 reports the velocities computed from the ExB spectra for the two ion species Xe^{+} and Xe^{++} for both working points. The last column tells how higher the doubly-ionized velocity is with respect to the singly-ionized.

$V_D[V]$	$u_{Xe^{+}}[m/s]$	$u_{Xe^{++}}[m/s]$	
240	17,176	22,775	+32.6%
300	18,247	23,989	+31.5%

Table 4.3: ExB measured velocities

According to equation 3.9 , if the ions were accelerated in the same point in the annular chamber (at the same voltage), the doubly-ionized ions would be $\sqrt{2}$ times faster than the singly-ionized, since the charge doubles. This should roughly lead to an increment of 41% in velocity. The fact that the increment is around 32 % is a proof that the second ionization, for the doubly-ionized ions, happens further downstream where the voltage is lower, as it can be seen from the simulation of the voltage profile in the annular chamber in figure 3.15.

4.2.6 Energy Distribution

The ion energy can be computed from the estimated velocity with equation 3.8. If expressed in electronvolts [eV] it must be computed by dividing the energy (in Joule) by the charge of the electron e:

$$E = \frac{1}{2}\frac{m_I}{e}u^2 \tag{4.16}$$

Figure 4.18 shows the energy spectra for both working points normalized with respect to the discharge voltage.

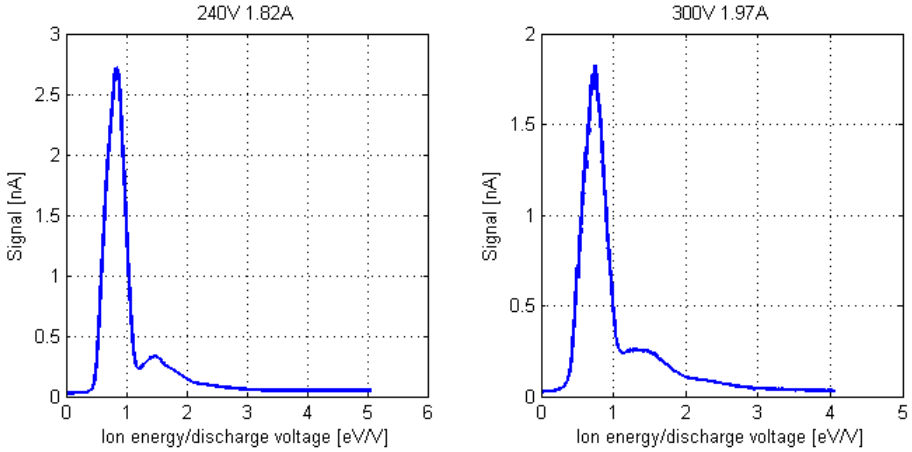

Figure 4.18: ExB energy spectra

The energy of the species are reported in table 4.4.

$V_D[V]$	$E_{Xe^+}[eV]$	$E_{Xe^+}/V_D[\%]$	$E_{Xe^+}[eV]$	$E_{Xe^{++}}/V_D[\%]$
240	200.73	83.64	352.90	147.04
300	226.53	75.51	391.52	130.51

Table 4.4: ExB measured ion energies

According to equation 3.8, the energy in electronvolts of singly-charged ions is equal to the acceleration voltage $V_{acc_{Xe^+}}$, since they have the same charge of the electron (absolute value). The acceleration voltage for the doubly-ionized ions can

be approximated to be equal to the difference between the energy of the doubly-ionized and singly-ionized (assuming that the doubly-ionized get ionized the first time at the same voltage of the singly-ionized).

$$V_{acc_{Xe^+}} = E_{Xe^+} \tag{4.17}$$

$$V_{acc_{Xe^{++}}} = E_{Xe^{++}} - E_{Xe^+} \tag{4.18}$$

By knowing the acceleration voltage for the species and the simulated potential profile of the Z-70 (figure 3.15 left) it is possible to estimate where the species are formed inside the thruster for the 240V point (no simulation was done for the 300 point). Table 4.5 reports the results.

$V_D[V]$	$V_{acc_{Xe^+}}[V]$	$V_{acc_{Xe^{++}}}$	$z_{Xe^+}[mm]$	$z_{Xe^{++}}[mm]$
240	200.73	152.18	~23	~28
300	226.53	164.99	-	-

Table 4.5: Acceleration potential and estimated ionization regions

Since the annular chamber is 23mm long, it means that the single-ionized ions are formed close to the annular exit section and doubly-ionized ions are formed approximately 5 mm outside. The fact that the ionization and acceleration happen also outside the chamber is demonstrated also by the LIF measurements [1], and it is also a feature of the Russian SPT-100. Figure 4.19 shows graphically the two ionization points.

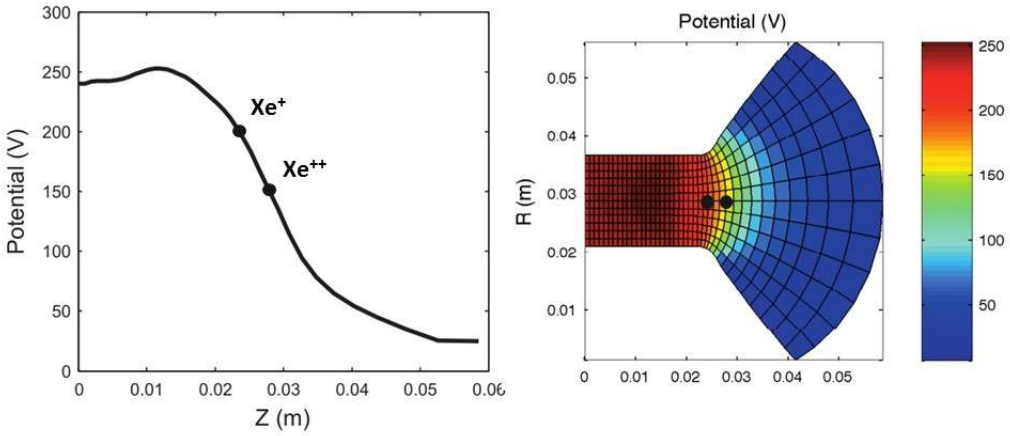

Figure 4.19: Z-70 ionization points

4.2.7 Current Fractions and Species Fractions

The species fraction for the each species i is defined as:

$$\xi_i \equiv \frac{n_i}{n_b} \tag{4.19}$$

Where $\sum \xi_i = 1$ and the total number density of the beam is the sum of the number densities of all the species:

$$n_b = \sum n_i \tag{4.20}$$

Analogously the total ion current can be described as the sum of all ion species currents:

$$I_b = \sum I_i \tag{4.21}$$

The current fraction of the species i is defined as:

$$\Omega_i \equiv \frac{I_i}{I_b} \tag{4.22}$$

Since a multiply-charged ion has a higher charge-state and velocity, it transports more current. The additional current is proportional to $Z_i^{3/2}$, where Z_i is the number of missing electrons of the multiply-charged ion for the species i (1 for single-charged, 2 for double-charged and so on). The current fraction can be computed with the following equation:

$$\Omega_i = \frac{\xi_i Z_i^{3/2}}{\sum \xi_i Z_i^{3/2}} \tag{4.23}$$

Where $\sum \Omega_i = 1$ and the species fraction ξ_i can be computed from the current fraction:

$$\xi_i = \frac{\Omega_i / Z_i^{3/2}}{\sum \Omega_i / Z_i^{3/2}} \tag{4.24}$$

Table 4.6 shows the current and species fractions for the two working points.

$V_D[V]$	$\Omega_{Xe^+}[\%]$	$\Omega_{Xe^{++}}[\%]$	$\xi_{Xe^+}[\%]$	$\xi_{Xe^{++}}[\%]$
240	86.19	13.81	94.64	5.36
300	78.35	21.65	91.10	8.90

Table 4.6: Measured current and species fractions

More than 5% of the ions are doubly-charged for the 240 V point, while the higher voltage point has an higher percentage of double-charged ions, as would be expected [11].

4.2.8 Charge Utilization Efficiency

Equation 3.31 for the anode efficiency η_a has to be modified to account for multiply-charged ions:

$$\eta_a = \frac{T^2}{2\dot{m}_p P_d} = \eta_q \eta_v \eta_b \eta_m \tag{4.25}$$

Where η_q is the charge utilization efficiency, which can be computed with the following equation:

$$\eta_q = \frac{\left(\sum \Omega_i / \sqrt{Z_i}\right)^2}{\sum \Omega_i / \sqrt{Z_i}} \tag{4.26}$$

Table 4.7 reports the charge utilization efficiency and the thrust correction factor for both working points.

$V_D[V]$	$\eta_q[\%]$	$\alpha[\%]$
240	98.90	95.95
300	98.37	93.66

Table 4.7: Charge utilization efficiency and thrust correction factor

The doubly-charged ions lower the thrust of about 4% in the case of 240V discharge voltage and 6.3% in the case of 300V discharge voltage, with respect to the ideal case of only singly-charged ions. The charge utilization efficiency is very high for both.

5 Final Remarks

5.1 Discussion of the Results

5.1.1 Thrust Stand and ExB Modifications

The modification of the thrust stand and the ExB sensor were overall successful. The closed-loop controlled system allows the moving part to oscillate around the equilibrium position, diminishing the non-linear effects, and the ExB spectra allow the computation of plasma proprieties .

5.1.2 Comparison between Estimated and Measured Velocity

The four main investigation techniques presented in this thesis exploited the thrust stand, the numerical simulation, the laser-induced fluorescence and the ExB sensor. While they measure different things, it is possible to estimate the velocity of the ions using all four techniques in order to compare the results obtained for the same working point (240V discharge voltage).

The velocity computed from the thrust stand data is the average velocity of the propellant, defined as the ratio between the measured thrust and the mass flow rate (anode plus cathode). The velocity computed from the simulations is also the average velocity of propellant, with the assumption that all ions are singly-charged. The velocity computed from LIF data is the average velocity of only singly-ionized ions in a particular point in space just after the exit section of the annular chamber. The velocity computed from the ExB spectrum is the velocity of singly-charged ions far away from the thruster.

	$u[km/s]$
Thrust Stand	13,071
Simulation	13,430
LIF	13,3
ExB	17,176

Table 5.1: Comparison between measured velocities

The velocities computed with thrust stand, simulation and LIF are very close. The thrust stand velocity is lower (even if the power was 30W higher) due to the fact that, unlike the LIF measurements, it accounts for losses due to the divergence angle of the plume. The velocity measured by the ExB is much higher. That's a sign that an acceleration happens because of the box which attracts ions due to its low potential. The box is intrusive and, even though it's called velocity selector, is more useful for measuring the composition of the plasma rather than the velocity of ions for Hall thruster measurements.

5.1.3 Thruster Issues

Two main issues affect this particular engine: the cathode and the insulation of the annular chamber. The cathode is not commercial and not space-qualified, and it is also very fragile and difficult to use. It needs two hour just for conditioning before each testing and it has to be cleaned regularly. The conditioning consists in flowing argon in the cathode while slowly increasing the heater current. In this way the poisoning oxygen is purged out, and the risk of cracking the electron emitting filament is low. The cathode represents potentially the major source of failure of each testing session. The insulation of the annular chamber is made of ceramics and it is cracked as it can be seen in figure 5.1. The cracking happened because of imperfections in the ceramics. Another set of ceramic walls have been sent by the manufacturer, but the author didn't replace the walls because Chris Young and Andrea Lucca Fabris, who obtained the LIF measurements, used the same cracked ceramic walls.

Figure 5.1: Cathode and falling insulation

5.2 Possible Future Work

5.2.1 Helicon Double-Layer Thruster

For future use, the new closed-loop controlled thrust stand can be used for precise measurements of the thrust produced by other thrusters owned by Stanford University like the cylindrical Hall thruster, the diverging cusped-field Hall thruster and the innovative Helicon double-layer thruster. In particular, the Helicon thruster under development at Stanford University is operated on water as propellant. Thrust measurements on the water-propelled Helicon will allow the computation of important performance parameters. The ExB sensor can also be used to investigate the plasma proprieties of the plasma produced by this innovative Helicon Double-Layer, which could represent a breakthrough in space propulsion.

5.2.2 Cooling Shroud

The thrust stand could be operated with the cooling shroud shown in figure 5.2.

Figure 5.2: Cooling shroud

The cooling shroud is a structure made of copper, where water can flow in an be the cooling fluid. The cooling shroud was not used for this thesis because of a water leak accident that happened during one of the testing sessions.

The shroud would dramatically decrease the thermal drift allowing for a much easier data acquisition.

5.2.3 Time-Resolved ExB signal

A possible future work consists in using the same techniques used for LIF measurements for the ExB signal. A time-resolved analysis would make it possible to compute the plasma composition as a function of time, during the breathing mode period. Nobody has ever done that.

6 Bibliography

References

[1] Christopher V. Young Andrea Lucca Fabris and Mark A. Cappelli. Time-resolved laser-induced fluorescence measurement of ion and neutral dynamics in a hall thruster during ionization oscillations. *Journal of Applied Physics volume 118, 233301*, 2015.

[2] Alec D. Gallimore Bryan M. Reid, Rohit Shastry and Richard R. Hofer. Angularly-resolved eb probe spectra in the plume of a 6-kw hall thruster. *AIAA 2008-5287*, 2008.

[3] Mark A. Cappelli Cheryl M. Lam, Eduardo Fernandez. A 2-d hybrid hall thruster simulation that resolves the exb electron drift direction. *IEEE Volume 43, Issue 1*, 2015.

[4] Andrea Lucca Fabris Christopher V. Young and Mark A. Cappelli. Ion dynamics in an exb hall plasma accelerator. *AIP Volume. 106, 044102*, 2015.

[5] Eunsun Cha Christopher V. Young. Comparison of hall thruster ion dynamics between laser induced fluorescence measurements and a 2-d hybrid simulation. *IEPC-2015-438 / ISTS-2015-b-438*, 2015.

[6] S. Mazouffre D. Renaud, D. Gerst and A. Aanesland. Exb probe measurements in molecular and electelectrone plasmas. *AIP Review of scientific instuments Volume 86,123507*, 2015.

[7] Ira Katz Dan M. Goebel. *Fundamentals of Electric Propulsion: Ion and Hall Thrusters pages 37-42 325-348*. Jet Propulsion Laboratory California Institute of Technology, 2008.

[8] Reed College David J. Griffiths. *Introduction to Electrodynamics pages 202-205*. Prentice Hall, 1999.

[9] O. Biblarz G. P. Sutton. *Rocket Propulsion Elements pages 660-666*. Wiley-Interscience, 2001.

[10] N. Koch G. Parissenti, D. Pavarin, E. Ahedo, K. Katsonis, F. Scortecci, and M. Pessana. Non conventional propellants for electric propulsion applications. *Space Propulsion 2010-1841086*, 2010.

[11] Richard Robert Hofer. *Development and Characterization of High-Efficiency, High-Specific Impulse Xenon Hall Thrusters pages 67-81*. PhD thesis, The University of Michigan, 2004.

[12] Y. Raitses J. Ashkenazy and G. Appelbaum. Investigations of a laboratory model hall thruster. *AIAA 95-2673*, 1995.

[13] A.D. Gallimore J.A. Linnel. Internal plasma potential measurement of a hall thruster using xenon and krypton propellant. In *AIP Physics of Plasmas volume 13, 093502*, 2006.

[14] John A. Hamley John M. Sankovic and Thomas W. Haag. Performance evaluation of the russian spt-100 thruster at nasa lerc. *IEPC-93-094*, 1993.

[15] Sang-Wook Kim and Alec D. Gallimore. Plume study of a 1.35 kw spt-100 using an exb probe. *AIAA-99-2423*, 1999.

[16] J. P. Boeuf L. Garrigues, I. D. Boyd. Computaion of hall thruster performance. *Journal of Propulsion and Power, Vol 17, No. 4*, 2001.

[17] J. A. Linnell and A. D. Gallimore. Efficiency analysis of hall thruster operation with krypton and xenon. *Journal of Propulsion and Power Vol. 22, No. 6*, 2006.

[18] Luigi T. De Luca. Space propulsion, 2002.

[19] Christopher V. Young Mark A. Cappelli, Ensun Cha, and Eduardo Fernandez. A zero-equation turbulence model for two-dimensional hybrid hall thruster simulations. *AIP Physics of Plasmas Volume 22, 114505*, 2015.

[20] C. Clauss P. Stuckey, M. Day, V. Murashko, N. Maslennikov K. Kozubsky, R. Gnizdor, B. Arhipov, G. Popov, V. Kim, V. Kozlov, and D. Grdlichko. Spt-140 high performance hall system (mphs) development.

[21] Peter Young Peterson. *The Development and Characterization of a Two-Stage Hybrid Hall/Ion Thruster pages 101-110*. PhD thesis, The University of Michigan, 2004.

[22] Ira Katz Richard R. Hofer, Ioannis G. Mikellides, Dan M. Goebel, Kristina K. Jameson, Regina M. Sullivan, and Lee K. Johnson. Efficacy of electron mobility models in hybrid-pic hall thruster simulations. *AIAA 2008-4924*, 2008.

[23] Christopher V. Young. The stanford diverging cusped field thruster: Design, construction, and initial testing pages 27-33 honor thesis, May 2010.

7 Appendix

7.1 Thrust Stand LabVIEW Software

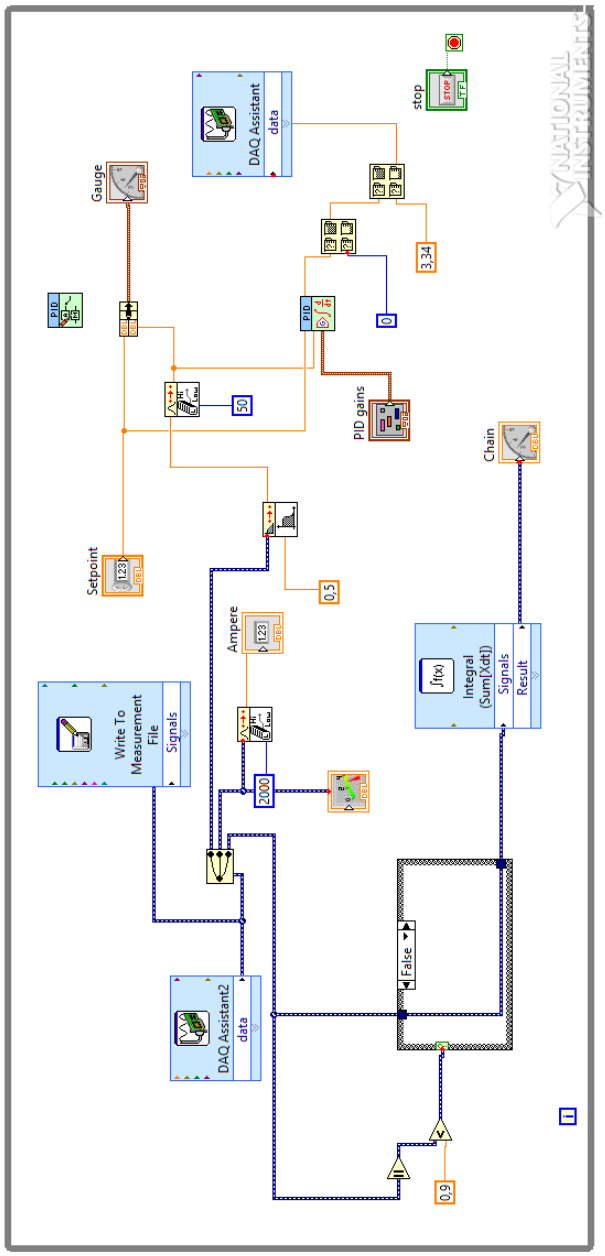

7.2 ExB LabVIEW Software

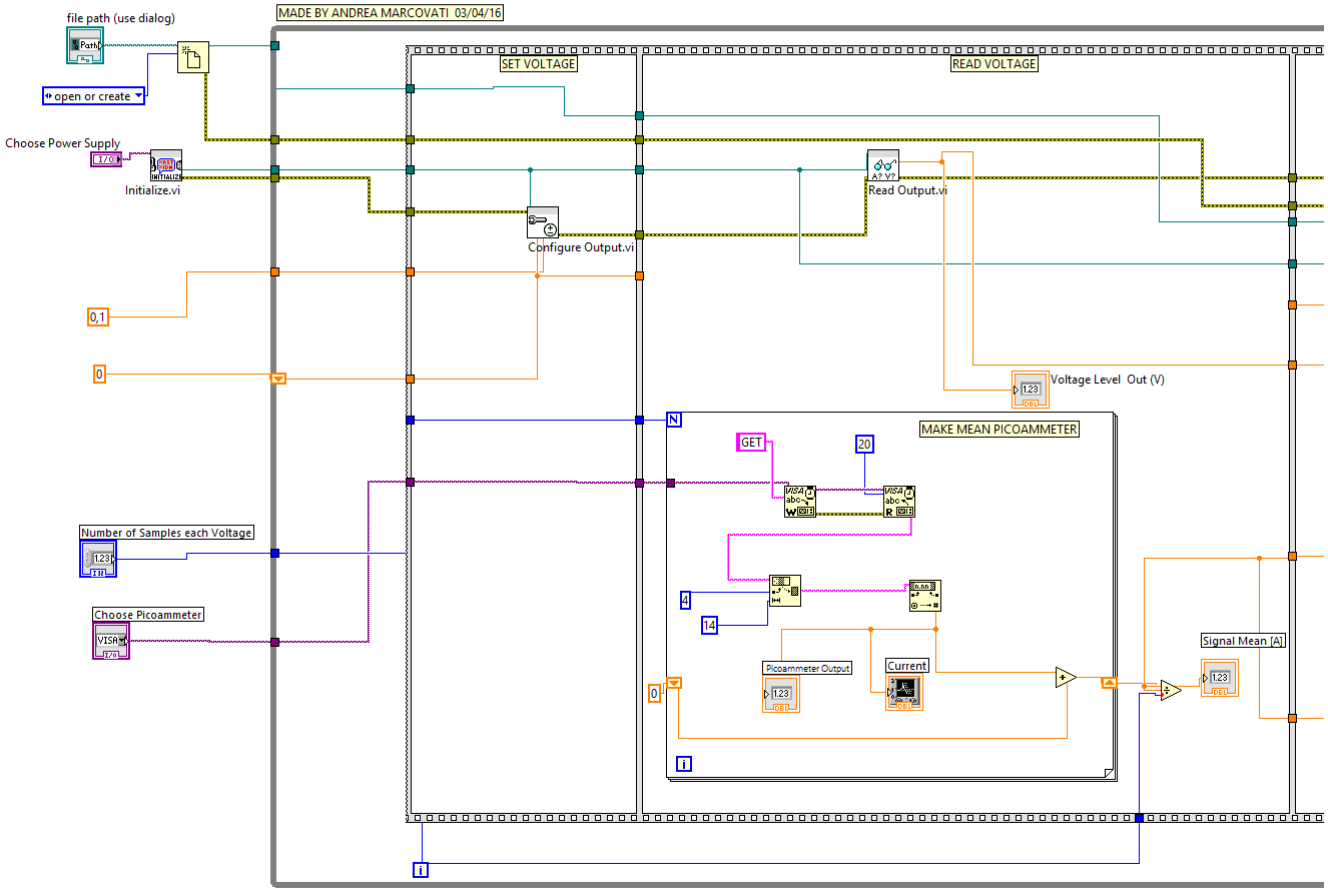

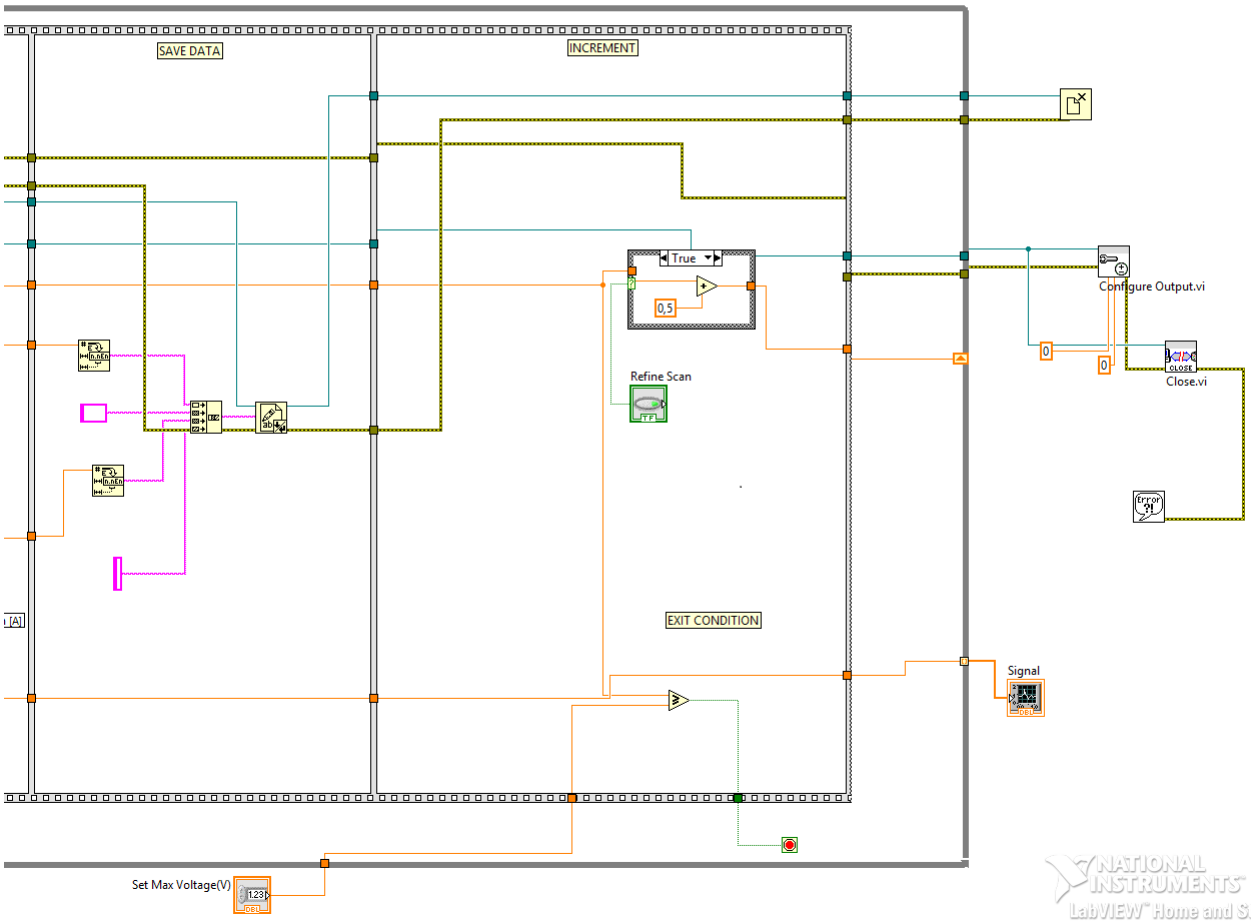
SAVE DATA
INCREMENT
True
0,5
Refine Scan
Configure Output.vi
Close.vi
EXIT CONDITION
Signal
Set Max Voltage(V)
NATIONAL INSTRUMENTS
LabVIEW Home and Stu